STUDYING THE DYNAMICS OF FC-ENGINEERED ANTIBODIES USING ADVANCED IMAGING METHODS

A Dissertation

by

SREEVIDHYA RAMAKRISHNAN

Submitted to the Graduate and Professional School of
Texas A&M University
in partial fulfillment of the requirements for the degree of

DOCTOR OF PHILOSOPHY

Chair of Committee,	Raimund J. Ober
Co-Chair of Committee,	Alvin T. Yeh
Committee Members,	Daniel Alge
	Andreea Trache
Head of Department,	Michael J. McShane

August 2021

Major Subject: Biomedical Engineering

ABSTRACT

The past decade has seen an enormous increase in FcRn-targeted engineering strategies to generate antibodies with therapeutic and diagnostic implications. The neonatal Fc receptor, FcRn, is a multifunctional receptor expressed abundantly throughout the body. The trafficking of engineered antibodies in the body is a multiscale process, taking place at subcellular, intracellular, and organ/tissue levels. In this study, various advanced imaging modalities are employed to capitulate the dynamics of Fc-engineered antibodies at different scales. The study investigates the fate of antibody-opsonized tumor cells after phagocytosis in macrophages, an intracellular/micrometer-scale process, using microscopy techniques. Results show a vacuole-like structure associated with the phagosomes exhibiting distinct characteristics. They are lysosomal in nature and impermeable to certain solutes, as seen using fluorescence microscopy analyses. The identification of this vacuole-like compartment has implications for understanding the subsequent processes involved in the degradation of antibody-opsonized tumor cells.

The use of advanced imaging approaches to study subcellular dynamics provides mechanistic insight with excellent spatiotemporal resolution. We imaged the 3D dynamics of two engineered FcRn-inhibitors at the subcellular/nanometer level, using an advanced imaging platform- rMUM. rMUM is capable of imaging the dynamics of the single molecule and the cellular organelles they interact with, in 3D. This enables compensation of the motion of a single molecule with the organelle's movement, thus giving a real snapshot of the dynamics. To that end, we utilized this multi-dimensional, nanometer

resolution microscopy technique to image two engineered FcRn-inhibitors in endosomes in cells.

At the macro level, we investigate the effective clearance of antigens by an engineered Fc-antigen fusion protein (HER2-Seldeg), consequently improving contrast during whole-body imaging in mice. HER2-Seldeg is designed to selectively capture anti-HER2 antibodies, bind to FcRn with enhanced affinity, and direct them to degradative lysosomes in FcRn-expressing cells. Positron emission tomography (PET) imaging of HER2-Seldeg revealed rapid clearance of radiolabeled antibodies from the systemic circulation following tumor localization and consequently improved contrast.

DEDICATION

To my lovely family for encouraging and supporting me to pursue my dreams

In memory of our GURU

ACKNOWLEDGEMENTS

I would like to express my heartfelt gratitude to my committee chair, Dr. Raimund J. Ober, and mentor Dr. E. Sally Ward, for their constant support and invaluable advice throughout my Ph.D. They've been instrumental in helping me grow as a researcher and teaching me how to look at the big picture. I am indebted to them for being very supportive during my difficult times and having faith in me. I have grown professionally as well as an individual under their mentorship. I will always cherish the long discussions I've had with Dr. Ober about science, philosophy, classical music, and life in general. I wish to thank them for entrusting me with this research, providing resources, and above all, having a vested interest in my professional and personal growth. I am grateful to my co-chair, Dr. Alvin Yeh, for his valuable suggestions and perspectives on my research and also for accepting to support me through the final years of my Ph.D. I would also like to thank Dr. Daniel Alge and Dr. Andreea Trache for serving as my committee member and providing helpful suggestions. I'd like to take this opportunity to thank Dr. Jerry Chao for being a teacher and a pseudo-mentor for the past few years. He has dedicated a significant amount of time helping me with my research design, taught me scientific writing, and also been a good friend.

I would like to extend my gratitude to former lab members Dr. Ramraj Velmurugan and Dr. Dongyong Kim, for being patient and teaching me techniques during my early stages of research. Special thanks to former lab members and friends Anish V. Abraham, Dr. Priyanka Khare, David Kim, and Dr. Xiaoli Wang for their moral support and for

making this exhausting graduate journey a bearable, fun-filled ride. Sungyong You deserves a special mention for being a great colleague to collaborate and work with, without whom my final years of Ph.D. would have been daunting. Many thanks to other lab members for their assistance and for creating a productive environment. I would like to thank my friends Shruthi Hamsanathan, Nivedita Ramadurai, Upendra Chitgupi, and Saarangan Krishnakumar for supporting me and uplifting me during difficult times. I am forever indebted to Dr. Samba Reddy and Savitha Reddy for looking out for me and making me feel at home throughout my graduate studies.

Finally, I would like to express my deep gratitude to my parents (Ramakrishnan Mani Iyer, Vijayalakshmi Ramakrishnan) and aunt Rajeswari Venkataraman for their unconditional love, an unfailing belief in me, and continually encouraging me to dream big. They never questioned my abilities and always had faith in me (even when I didn't). I am indebted for life, for the sacrifices they've made to help me chase my dreams. My father is the greatest source of strength in my life, my beacon of light during dark times, and my North Star. I hope this dissertation will compensate for the years we've lived apart.

CONTRIBUTORS AND FUNDING SOURCES

Contributors

This work was supported by a dissertation committee consisting of Professor Raimund J. Ober (chair), previously of the Department of Biomedical Engineering at Texas A&M University and currently of the Department of Imaging and Biomedical Engineering at the University of Southampton; Professor Alvin T. Yeh (co-chair), and Professor Daniel Alge of the Department of Biomedical Engineering at Texas A&M University; and Professor Andreea Trache of the Department of Medical Physiology at Texas A&M University.

The paper reprinted in Section 2 was authored by Professor E. Sally Ward, Professor Raimund J. Ober, Dr. Ramraj Velmurugan, and the student. Dr. Ramraj Velmurugan and the student co-authors the paper and equally contributed to this study. The experiments detailed in Section 2 were conducted in part by the student in collaboration with Dr. Ramraj Velmurugan and Mingin Kim of the Medical Science Graduate Program, Texas A&M University Health Science Center. The data analysis, results, and corresponding figures integral to this paper were prepared by the student in collaboration with Dr. Ramraj Velmurugan, Professors E. Sally Ward, and Raimund J. Ober. Peripheral Blood mononuclear cell samples were provided by Professor Darrell Pilling of Texas A&M University.

The experimental design and methodology described in Section 3 were designed by the student and Professor Raimund J. Ober. The student optimized the sample

preparation, acquired biological data, data-mined, and conducted data analysis. Proteins used in Section 3 were designed, purified, biotinylated, and provided by Dr. Wei Sun, Dr. Rafal Swiercz, and Dr. Pavel Savitskiy. The software used in this section was developed in part by Sungyong You, Anish V. Abraham, and Dr. Jerry Chao. The writing, reviewing, and interpretations of data were made by the student and Professor Raimund J. Ober.

The study presented in Section 4 was conducted in collaboration with Dr. Xiankai Sun's research group in UTSW Medical center. The proteins mentioned in the study were purified by Dr. Wei Sun. Animal breeding and tumor implantation was performed by Dr. Priyanka Khare, and PET imaging was done by Dr. Guiyang Hao, Su-Tang Lo, and Kien Nham. HCC1954 breast cancer cell line was a gift from Drs. John Minna and Kenneth Huffman. The data analysis, quantification of contrast measures, results, and interpretations described in Section 4 were performed by the student in collaboration with Dr. Priyanka Khare, Dr. Wei Sun, Professors Raimund J. Ober, Xiankai Sun, and E. Sally Ward.

All other work presented in this dissertation was performed independently by the student.

Funding Sources

This research was supported in part by grants from the National Institutes of Health (R01GM085575, awarded to R. J. Ober) and the Cancer Prevention and Research Institute of Texas (RP140141 awarded to E. S. Ward, RP110441 awarded to E. S. Ward and R. J. Ober, and RP160051 awarded to E. S. Ward). The authors declare no conflict of interest.

NOMENCLATURE

^{124}I – Radioisotope of Iodine-124

^{125}I – Radioisotope of Iodine-125

2D – Two Dimensions

3D – Three Dimensions

ADCC – Antibody Dependent Cellular Cytotoxicity

ADCP – Antibody Dependent Cellular Phagocytosis

ANOVA – ANalysis Of VAriance

APCs – Antigen Presenting Cells

β2m – β2-microglobulin

CCD – Charged Coupled Device

CDC – Complement Dependent Cytotoxicity

CFSE – CarboxyFluorescein Succinimidyl Ester

CH – Constant Heavy chain

CM – Contrast Measure

CSF – Colony Stimulating Factor

CT – Computed Tomography

DIC – Differential Interference Contrast

DMEM – Dulbeco's Modified Eagle Medium

DMSO – DiMethyl SulfOxide

EDOF – Extended Depth Of Focus

ELISA – Enzyme-linked ImmunoSorbent Assay

EMCCD – Electron Multiplying Charged Coupled Device

FCS – Fetal Calf Serum

FcRn – Neonatal Fc Receptor

FcγR – Fcγ Receptors

FITC – Fluorescein IsoThioCyanate

GFP – Green Fluorescent Protein

HEK-293 – Human Embryonic Kidney cells

HER2 – Human Epidermal growth factor Receptor 2

HILO – Highly Inclined and Laminated Optical sheet

HMEC-1 – Human Microvascular Endothelial Cells 1

IgG – Immunoglobulin G

IVIG – IntraVenous ImmunoGlobulin

MFI – Mean Fluorescence Intensity

MG – Myasthenia Gravis

MHC – Major Histocompatibility Complex

MIP – Maximum Intensity Projection

MOG – Myelin Oligodendrocyte Glycoprotein

MRI – Magnetic Resonance Imaging

MSD – Mean Square Displacement

MST-HN – M252Y/S254T/T256E/H433K/N434F

MUM – MUltifocal plane Microscopy

MUMLA – MUltifocal plane Microscopy Localization Algorithm

NA – Numerical Aperture

NaCl – Sodium Chloride

NK – Natural Killer

PET – Positron Emission Tomography

PBS – Phosphate Buffered Saline

PLAM – Practical Localization Accuracy Measure

PSF – Point Spread Function

QD – Quantum Dot

RMUM – Remote focusing Multifocal plane Microscopy

ROI – Region Of Interest

RMS – Root Mean Square

RPMI 1640 – Roswell Park Memorial Institute 1640 medium

sCMOS – scientific Complementary Metal-Oxide-Semiconductor

SEM – Standard Error Mean

SD – Standard Deviation

SNR – Signal to Noise Ratio

SPECT – Single-Photon Emission Computed Tomography

SPT – Single Particle Tracking

TC – Transport Carriers

TIRFM – Total Internal Reflection Fluorescence Microscopy

TEM – Transmitted Electron Microscopy

TRITC – Tetramethyl Rhodamine IsoThioCyanate

VH – Variable Heavy chain

VL – Variable Light chain

WCP – Whole Cell Phagocytosis

TABLE OF CONTENTS

Page

LIST OF FIGURES

Page

1. INTRODUCTION

The present work is directed towards studying the dynamics of engineered antibodies using advanced imaging techniques in vitro and in vivo. The first aim focuses on studying the fate of antibody-opsonized tumor cells after phagocytosis in macrophages, primarily using microscopy techniques. To study the biomolecular interactions of engineered antibodies with their cellular environment, continual development of advanced imaging systems is needed. To that end, the second aim focuses on the validation of an advanced 3D imaging platform, remote focusing multifocal plane microscopy (rMUM), for studying the dynamics of an Fc-engineered FcRn inhibitor. Finally, the third aim focuses on investigating the potential of an Fc-antigen fusion protein as a clearing agent to improve contrast during whole-body imaging.

This section gives a brief overview of FcRn function, engineering FcRn-IgG interactions for the modulation of antibody dynamics, phagocytosis in immune cells, and 3D imaging of single molecules.

1.1 Role of FcRn in antibody dynamics

The role of MHC class I-related receptor or the neonatal Fc receptor FcRn in the transfer of antibody molecules of the immunoglobulin G (IgG) across the neonatal gut epithelial barrier and within other cell types is well established (*1*, *2*). Two primary roles of FcRn include maintenance of IgG homeostasis (*3*, *4*) and transportation of the same across cellular barriers (*5–7*). Due to its role as a homeostatic regulator of the ubiquitously expressed immune molecule (IgG), FcRn is expressed in multiple cells types found throughout the body (*3*, *6*, *8–10*).

1.1.1. Molecular nature of FcRn-IgG interaction

FcRn is like an MHC class-I receptor comprising a heterodimer of a heavy chain (α) and β2microglobulin (β_2m)(*11*) and interacting with the constant region (Fc) of immunoglobulin IgGs (*3*, *12*, *13*). The β_2m association is required for the regular expression and function of FcRn (*14*). Earlier studies have identified the residues at the interface of CH2-CH3 domains of the fragment crystallizable contant (Fc) region of an IgG responsible for FcRn interaction (*12*, *15–17*) (Figure 1.1). The residues were identified as Ile253, His310, His435, His436 (mouse), or Tyr436 (human). Residues at 253 and 310 are highly conserved compared to the residues at 435 and 436, which exhibits higher species variability (*18*, *19*). The histidine residues play an essential role in conferring the pH dependence to FcRn-IgG interactions (*20*, *21*). Most IgGs bind to FcRn with relatively high affinity at acidic pH (pH 5.5-6.0), with very low to negligible affinity at near-neutral pH (pH 7.3-7.4) (*21*, *22*). FcRn-IgG interactions are dependent on the residues at the binding interface, and they differ across species due to cross-species differences (*22–24*). Cross-species differences have limited the use of traditional mouse models and led to the development of transgenic mice models that express human FcRn for clinical studies involving engineered antibodies (*26–28*).

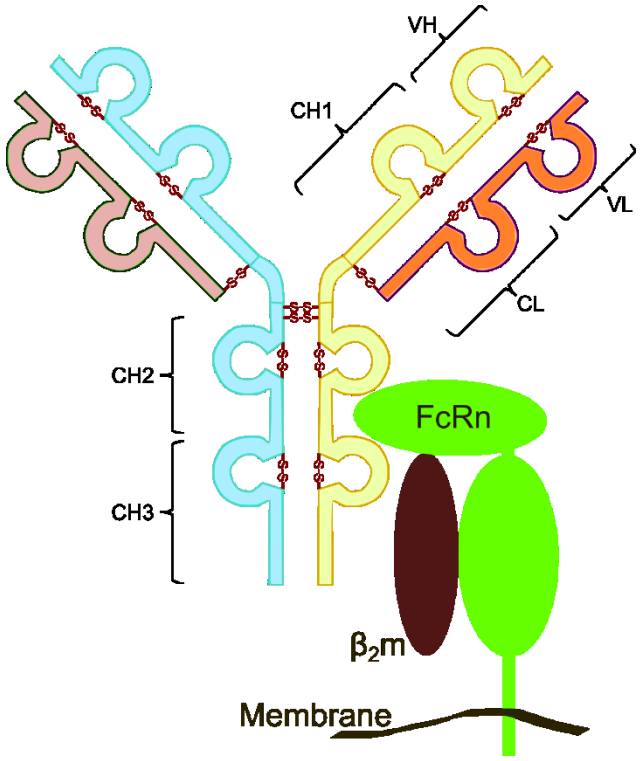

Figure 1.1 Schematic representation of FcRn-IgG interaction
The two heavy chains and two light chains are colored blue/yellow and pink/orange, respectively. The variable fragment (Fv, consisting of VH and VL domains) confers antigen binding activity, while the constant region (Fc, fragment crystallizable) of the heavy chain (consisting of CH1, CH2, CH3 domains) interacts with Fc receptors and complement components to mediate effector functions and in vivo persistence. The domains of the antibody are shown with disulfide bonds depicted as –S-S linkages. The heavy (α) chain (green) and β2-microglobulin (black) that comprise FcRn are shown, with the transmembrane region of the α chain inserted into a membrane.

1.1.2. FcRn expression in cells and tissues

Although initial studies believed that FcRn expression was confined to the gestation and neonatal periods in humans and rodents (*28*, *29*), later results pointed to its presence in multiple cell types and tissues (*1*, *30*). FcRn expression in the majority of hematopoietic cells, parenchymal

(endothelial cells, epithelial cells), podocytes, at the blood-brain barrier, corneal tissues, retina, and conjunctiva is well documented (*6*, *9*, *10*, *31–33*). The ubiquitous presence of FcRn throughout the body is consistent with its diverse role as a regulator of IgG homeostasis (*8*, *9*) and albumin levels (*34*), transporter of antibodies across epithelial barriers (*5–7*, *35*), and function in antigen presentation and cross-presentation in immune cells (*36–39*).

1.1.3. Subcellular trafficking of FcRn

To understand the mechanisms involved in maintaining the homeostasis of IgG and gain insights for designing antibodies that can modulate IgG dynamics in the body, the subcellular trafficking behavior of FcRn needs to be understood. The trafficking of the FcRn-IgG complex has been studied by live-cell imaging of FcRn-GFP transfected endothelial and epithelial cells (*40–45*). IgG enters the cells by fluid-phase pinocytosis (due to its negligible binding affinity to FcRn at pH 7.3). Subsequently, the IgGs enter the endolysosomal pathway and bind to FcRn in early/sorting endosome (acidic pH 6.0), are sorted into tubularvesicular recycling (or transcytotic) transport carriers (TCs), and are exocytosed into the extracellular milieu, thus salvaging IgGs from degradation (*40–42*). These endosomal sorting processes enable FcRn to regulate IgG levels. Advanced microscopy imaging studies using multifocal plane microscopy show that after segregation from sorting endosomes, the FcRn-positive recycling TCs traffick to the cell membrane and undergo exocytosis (*42*, *46*). Additionally, a subset of the TCs merge with other sorting endosomes (called interendosomal transfer) or return to the same sorting endosome (called looping) (*46*). Under conditions of high IgG concentrations that lead to saturation of FcRn (bound state), or if IgG fails to bind to FcRn in sorting endosomes, the unbound antibodies enter lysosomes and are degraded (*41*).

1.2 Engineering FcRn-IgG interactions

Two decades of research have revealed how FcRn functions as a global regulator of IgG levels and transport. This knowledge has opened avenues for engineering antibodies to exploit this interaction to extend in vivo half-lives of IgG, enhance antigen clearance, and generate antibodies that inhibit the FcRn-IgG interaction (*47*, *48*).

1.2.1. Generation of inhibitors of IgG-FcRn interactions

FcRn maintains IgG levels by salvaging them from degradation, and this can be targeted for ameliorating diseases in which pathogenic antibodies play a role in pathogenesis. Multiple inhibitors of FcRn have been designed and used to reduce pathogenic antibodies or autoantibodies in conditions such as autoimmune disorders (*49–54*). These FcRn inhibitors are engineered IgGs or Fc fragments that have enhanced binding affinity to FcRn in the pH range of 6.0-7.4 (*49*, *51*, *53*, *55*), thus competing with endogenous IgGs and driving unbound pathogenic antibodies to lysosomes for degradation (*49*). This has significant clinical relevance in autoimmune conditions where a greater than 50% decrease in autoantibodies can result in disease amelioration (*56*, *57*).

Several small molecules, peptide-based or antibody-based FcRn inhibitors, have been generated (*49*, *51*, *53*, *55*, *58–60*), and several of these are in different stages of clinical trials following preclinical analyses in animal models (*54*, *61*, *62*). One such FcRn inhibitor that has its constant region engineered is called an Abdeg (antibody that enhances IgG degradation) and binds to FcRn with increased affinity at both acidic and near-neutral pH, but with retention of the pH dependence of the interaction, i.e., higher affinity at acidic pH than at pH 7.3-7.4 (*49*). The Fc region is engineered to introduce MST-HN mutations (M252Y/S254T/T256E/H433K/N434F). As a result of this engineering, Abdegs are efficiently internalized by receptor-mediated endocytosis into FcRn-expressing cells and bind to FcRn with increased affinity in acidic endosomes.

Consequently, they accumulate to very high levels in cells, reduce the availability of free FcRn in acidic endosomes and drive endogenous wild type IgGs into lysosomes for degradation (Figure 1.2). In a serum transfer model of arthritis in mice, Abdegs reduced swelling and inflammation in the joints in both therapeutic and prophylactic disease settings (*55*). In a passive model of antibody-mediated experimental autoimmune encephalomyelitis, Abdegs were also shown to ameliorate disease by mediating both the rapid clearance and reducing the accumulation of encephalitogenic antibodies in the CNS (*63*).

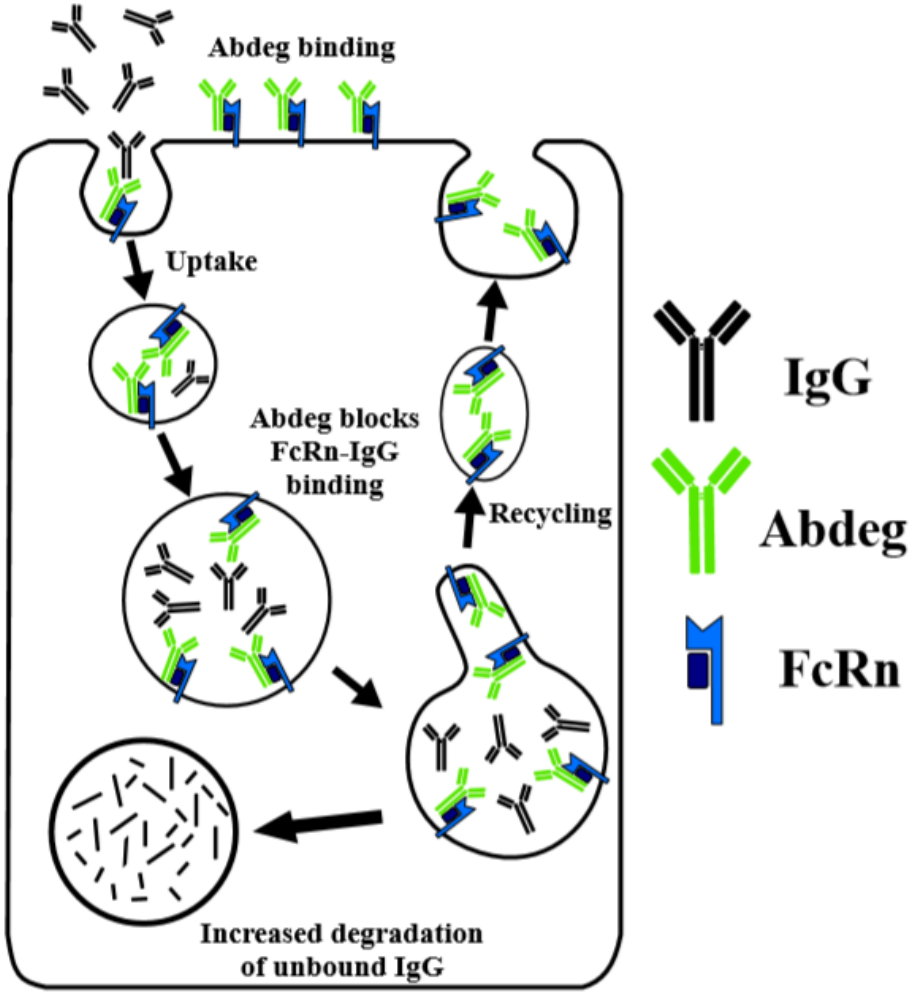

Figure 1.2 Engineering antibodies to inhibit FcRn-IgG interaction
FcRn inhibitors such as Abdegs are engineered to bind to FcRn with an enhanced affinity in the pH range of 6.0 to 7.4. These inhibitors enter the cell via receptor (FcRn)-mediated endocytosis, inhibit endogenous IgGs from binding to FcRn in acidic endosomes, and consequently led to the entry of these competing IgGs into lysosomes (*49*, *64*). Note that Abdegs described here binds via its Fc region to FcRn. However, there are other subtypes of inhibitors that bind through their Fv region (*53*, *59*).

1.2.2. Engineering antibodies for targeted clearance of antigen-specific antibodies

FcRn inhibitors binding to FcRn with increased affinity exhibit relatively short in vivo half-lives (*53*, *59*, *65*, *66*). due to their entry into the lysosomal pathway (*67*). One of these engineered antibodies (Abdeg) has been used in diagnostic or theranostic imaging to clear the radiolabeled antibody in the systemic circulation, subsequently decreasing background levels and improving contrast during tumor imaging (*68*). Inhibition of FcRn also has applications in the reduction of dose-limiting toxicity after localization of radiolabeled antibodies during radioimmunotherapy (*69*). Although FcRn inhibitors have many applications, they decrease IgG levels independent of the antigen specificity of the IgG. This has motivated the generation of an antibody-based reagent that can selectively deplete antigen-specific antibodies without affecting the clearance of endogenous antibodies of other specificities (*70*). Briefly, engineered antigen-Fc fusion protein called Seldegs (Selective degradation of antigen-specific antibodies) comprising a target antigen fused to an engineered Fc fragment of human IgG1, which is heterodimerized with an Fc fragment (without antigen fusion) to display the antigen in monomeric form (Figure 1.3). Mutations to ablate FcγR binding and enhance FcRn binding at a pH range of 6.0-7.4 were introduced into the Fc region. In contrast to Abdegs, Seldegs specifically capture the antigen-specific antibodies and bind

to FcRn on the cell membrane at pH 7.4. The antigen-specific antibodies bound to Seldeg subsequently enter lysosomes and are cleared (Figure 1.3). Seldegs have been shown to specifically target and clear antigen-specific antibodies without affecting the levels of antibodies of other specificities (non-target). Seldegs can be used at relatively low doses and therefore target only a small subset of FcRn molecules. Consequently, Seldegs do not result in the reductions of the levels of antibodies that are not specific for antigen (*70*).

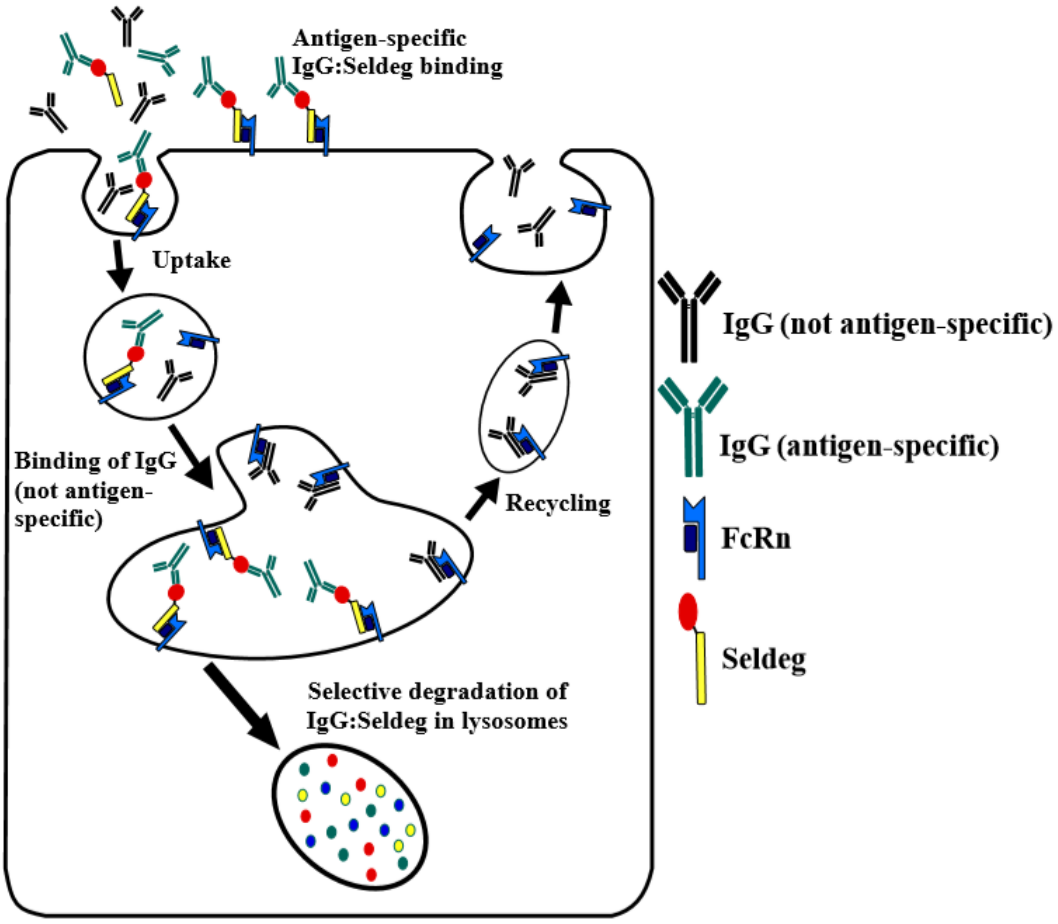

Figure 1.3 Engineering Fc-antigen fusion antibodies for selective degradation of antigen-specific IgG

A class of Fc-antigen fusion protein called Seldegs has one antigen molecule per Fc fragment and can selectively target antigen-specific antibodies and internalize them via FcRn-mediated

endocytosis. Seldegs result in lysosomal delivery of antigen-specific antibodies without affecting the levels of antibodies of irrelevant specificities (*47*, *70*).

1.3. Engineering therapeutic antibodies for cancer therapy

The therapeutic monoclonal antibody market has grown significantly, and these biopharmaceutical products have become one of the top promising choices to treat cancer and other disorder (*71–73*). Chimeric or humanized therapeutic antibodies have been developed against CD20 (Rituximab), HER2 (Trastuzumab), and multiple other targets. Rituximab (*74*) is an antibody specific for the CD20 receptor and one of the first therapeutic to be approved for cancer patients, while Trastuzumab (*75*) is specific for HER2 (a growth factor receptor) and approved for treatment in breast cancers.

1.3.1. Mechanisms involved in the killing of cancer cells

For therapeutic antibodies, immune-mediated mechanisms have been investigated for playing a role in killing cancer cells. One such killing process is antibody-dependent cellular cytotoxicity (ADCC), where natural killer (NK) cells induce killing (*76*). Fcγ receptors expressed on the surface of NK cells bind to antibody-opsonized cells and kill them using granzymes. Studies have established an increase in ADCC levels following trastuzumab therapy (*77–80*). Another mechanism by which cancer cells are killed is complement-dependent cytotoxicity (CDC) where, the antibody-opsonized cells recruit a group of soluble proteins called the complement system, which in turn mediates cell death (*81*, *82*). Antibody-dependent cellular phagocytosis (ADCP) mediates cell death by engulfing entire antibody-opsonized cancer cells and direct them for degradation (*83–86*). Several studies carried out in mouse models delineate the importance of

ADCP in antibody-mediated therapy for cancer (*87*, *88*). These findings have notably garnered renewed interest in the potential anti-tumorigenic role of macrophages that contrast with their pro-tumorigenic role in facilitating tumor progression (*89–91*).

Fc receptors are opsonic receptors, which are expressed by a variety of cell types and bind antibody molecules with different affinities (*92*). The important classes of Fc receptors are as follows: i) Fcα receptors which bind the IgA class of immunoglobulin antibodies and regulate mucosal immunity (*93*). ii) The Fcε receptors which bind the IgE class of immunoglobulins and responsible for responses against allergens and parasites (*94*). iii) The Fcγ receptors, the primary class of Fcγ receptors involved in phagocytosis, which bind to IgG (*92*, *95–98*). There are six human Fcγ receptors (FcγRI, FcγRIIA, FcγRIIB, FcγRIIC, FcγRIIIA, and FcγRIIIB), with varying ability to bind the different IgG subclasses in the soluble and immune-complexed forms (*98*). While human FcγRI has a high affinity towards IgG molecules, other Fcγ receptors have a substantially lower affinity (*92*, *98*, *99*). This selectivity allows the low affinity receptors to specifically engage targets only when proteins or particles (e.g., viruses, cells, bacteria) are bound by multiple antibody molecules. Antibody-opsonized particles larger than 0.5 μm can be phagocytosed by macrophages (*100*). FcγRs possess either an immunoreceptor tyrosine-based activation (ITAM) or inhibitory (ITIM) motif (*101*). The clustering of activating FcγRs results in ITAM phosphorylation and activates a signaling cascade that collectively drives phagocytosis (*102*, *103*). Macrophages co-express both activatory FcγRs and the inhibitory FcγRIIB, and a balance between the expression levels and occupancy of these two receptor classes has a significant impact on phagocytosis (*104*).

The typical targets that are opsonized by antibody molecules are pathogens that have elicited an antibody response by the humoral immune system. Targets of a cellular origin have

also become an important area of study with respect to Fcγ receptor-mediated phagocytosis due to the use of monoclonal antibody therapeutics to target cancer. The study of cellular phagosomes is crucial in understanding the process of ADCP of targets such as tumor cells. Therapeutic antibodies recognize and opsonize tumor-specific antigens, triggering Fcγ receptor-mediated phagocytosis leading to ADCP (*88*, *105*). Macrophages are the most abundant immune cell type in the majority of tumors (*106*). Thus, macrophage-mediated ADCP may contribute to the anti-tumor effects of antibodies (*89–91*, *107*), and understanding the maturation pathway of cellular phagosomes is crucial to the successful use of therapeutic antibodies.

1.3.2. Formation and maturation of phagosomes

Most eukaryotic cells are capable of phagocytosing pathogens, cellular debris, and apoptotic cells. Macrophages play a major role as phagocytes and express a variety of surface receptors to identify target antigens. In addition to FcγRs, the receptors involved can be opsonic receptors that include pattern recognition receptors responsible for detecting pathogens and apoptotic corpse receptors that detect the phosphatidylserine on the surface of apoptotic cells (*103*). As soon as the macrophages recognize a target, well-orchestrated events of biological pathways follow(*108*). The phagocytic receptors cluster on the cell membrane before the formation of the phagocytic cup. The molecular machinery responsible for phagosome maturation includes membrane lipids and the Rho family of GTPases (*109–114*). This membrane remodeling is followed by downstream signals that affect cytoskeletal remodeling (*115–117*).

Subsequently, the phagosomes sequentially fuse with lysosomes (termed as ‘phagolysosomes’(*118*)) and become acidified (*108*). The acidification process is not abrupt but rather gradual and is carried out by vacuolar (H+)-ATPase (*119*). The degree of acidification is a well-studied process and varies with cell types. The phagosomal contents are either released as

nutrients or, via several complex pathways that have been extensively analyzed, presented as antigen peptides on major histocompatibility complex (MHC) class I and II molecules (*120–122*).

1.3.3. Trogocytosis

When macrophages expressing FcγRs interact with the Fc regions of antibodies bound to a target cell, instead of phagocytosis, a process called 'trogocytosis,' where only parts of the target cell membrane are engulfed, can occur (*123*). Trogocytosis is derived from the Greek word 'trogo' which means to gnaw or nibble. In some cases, trogocytosis (or 'shaving') mediates the removal of target antigen such as CD20 from the cell surface during therapeutic administration of rituximab during the treatment of chronic lymphocytic leukemia (CLL) (*124*). Trogocytosis-mediated clearance of surface antigen is therapeutically beneficial when anti-CD22 antibodies are used in the treatment of B cell-dependent autoimmune diseases (*125*). By contrast, macrophage-mediated trogocytosis can lead to the death of tumor cells opsonized with anti-HER2 monoclonal antibodies (*89*). Thus, the therapeutic consequence of trogocytosis could be positive or negative depending on the therapeutic setting (target antigen and/or tumor cell in question) and is now recognized as an important effector function for any class of therapeutic monoclonal antibody (*126*).

1.4. Imaging of single molecules

The imaging of biological systems with light microscopes has been the gold standard in studying the dynamics in living cells. The first microscope was invented almost three centuries ago, and since then, optical microscopy has evolved and expanded to become a powerful technique with excellent resolution. Advances in the capabilities of detectors (highly sensitive photon-recording devices), the advent of high-speed data acquisition, the automation of image processing, significant improvements in the quality of sophisticated optical components and aberration-

correcting devices, and the discovery and development of fluorescent proteins, which allow the tagging of specific proteins inside cells, have revolutionized the field of bioimaging (*127–129*).

For many decades fluorescence imaging experiments revolved around bulk studies using fluorescently labeled proteins. The results obtained were sub-par because they were merely an average over the ensemble of molecules that masked the dynamics of the individual molecules. Key information is lost if the imaging environment is heterogeneous in nature. Live cellular systems are heterogeneous, and therefore investigation of their dynamics at the single molecule level is warranted. Single molecule imaging overcomes the bulk averaging effects and provides detailed information on the dynamics of single molecules (*127*, *129*).

1.4.1. Techniques involved in single molecule microscopy

The characteristics of fluorophores play a major role in defining the efficiency of single molecule experiments(*130*). Fluorophores should be bright, have an emission wavelength in the visible spectrum, and be easily tagged to the molecule of interest without hampering the molecule's function. They should also be small in size, highly photostable, and nontoxic to the cells. Most fluorescent dyes are susceptible to photobleaching and thus allow the molecules tagged to it to be imaged for only a short period (typically a few seconds). Quantum dots are a class of fluorophore dyes that were developed to overcome this limitation (*131*, *132*). They are highly photostable and brighter compared to conventional fluorescent dyes (*132*) and are chemically coupled to proteins of interest. However, problems such as the multivalency of the avidin-biotin or chemical labeling approach, the blinking behavior whereby a quantum dot fluoresces in an intermittent fashion over time, and non-specific binding, require careful experimental design.

Confocal and widefield methods are employed for single molecule imaging. In confocal imaging, a diffraction-limited spot of small volume (10^{-10}-10^{-12} cm^3) is sequentially scanned to

illuminate the sample, and a photomultiplier tube is used to record the collected fluorescence. Widefield fluorescence microscopy is typically used to image biological samples (e.g., a monolayer of cells on a treated substrate or a thin tissue section) through a high numerical aperture (n_a) objective lens, and a using a highly sensitive CCD or CMOS camera is used to detect the often low fluorophore signals from the molecules of interest. This microscope configuration produces an image of the sample as observed from a particular focal depth (*133*). The signal from the plane of focus corresponding to this focal depth contributes to the image, but in a way that "blurs" the image. This blurring is a consequence of the point spread function (PSF) of the microscope, which depends on the particular characteristics of the objective lens. Advanced techniques such as total internal reflection fluorescence microscopy (TIRFM) (*134*) and highly inclined and laminated optical sheet (HILO) have been widely used to selectively illuminate parts of a live cell using a beam of light. By adopting such selective illumination, the fluorophore-tagged molecules in the sample are not excited all at once, thus reducing the background. This improves the signal-to-noise ratio (SNR). TIRFM has been the technique of choice to study dynamic cellular events on the plasma membrane, especially exocytic events (*135*).

1.4.2. 3D single molecule microscopy

Advances in single molecule imaging capabilities have revolutionized how eukaryotic biological systems are visualized. Cellular biological processes are complex and three-dimensional, and the details of how they occur are not fully explored. To gain any meaningful insight into the complex cellular machinery, 3D single molecule imaging systems are required. The classical approach is to physically move the sample (using a piezo stage) or the objective lens in order to image and therefore visualize a cell in three dimensions. Despite using ultra-fast scanners or galvanometers for rapid scanning, images exhibit artifacts due to the time differences

between the acquisitions at the different focal planes. Confocal systems have been used for detecting single molecules in three dimensions by circling the confocal beam around the single molecule using very complex optical systems (*136*). Another approach for 3D single molecule imaging utilizes engineered PSFs. By appropriately engineering the shape of the PSF, different images of a point source are generated in a depth-dependent manner, thereby allowing the accurate estimation of the axial position of the point source even when it is near-focus. There are different types of engineered PSFs in use (*137*, *138*). For example, in the astigmatic method, the PSF is elongated in one direction as a function of defocus. In the double helix method, the PSF is engineered in the shape of two lobes by introducing a phase plate in the optical light path. In this case, the defocus information is encoded by the rotation of the pair of lobes around their center of gravity. These techniques have limited axial coverage of ~ 3 μm, but living cells are 10-20 μm thick.

It is essential to study the interactions between various biomolecules in cells to better understand fundamental biological pathways. This became possible with the advent of techniques to track single molecules with high temporal resolution (*139*). Single particle tracking (SPT) is widely carried out using widefield microscopy methods in two dimensions. However, it becomes significantly more challenging when the particle has to be tracked in three dimensions, as the conventional widefield technique captures images only in one focal plane. The single molecule being tracked will move in and out of the focal plane being imaged, and the inadequate depth information afforded by the conventional setup will make it difficult to estimate the axial location of the single molecule accurately (*140*). Techniques that employ scanning of the sample (*141*), and engineering the point spread function as a function of defocus (*137*, *138*, *142–144*) have been in practice for determining the location of single molecule in 3D space.

Multifocal plane microscopy (MUM) was developed to address these challenges (*145*–*147*). In MUM, light from the sample is partitioned and directed to different cameras (Figure 1.4). By customizing the distance between the tube lens and each camera using special optics, the cameras can simultaneously image distinct focal planes within the sample. This technique overcomes the depth discrimination problem, a well-known shortcoming of the conventional widefield techniques (*148*). An important aspect of MUM on the analysis side is the use of an algorithm called MUM localization algorithm (MUMLA) to accurately estimate the 3D positions of molecules of interest from the collected multifocal plane image data (*145*). 3D single molecule imaging, using MUM, of transcytosis and endocytosis, respectively, in epithelial and endothelial cells of 10μm thickness, has been demonstrated (*146*, *147*).

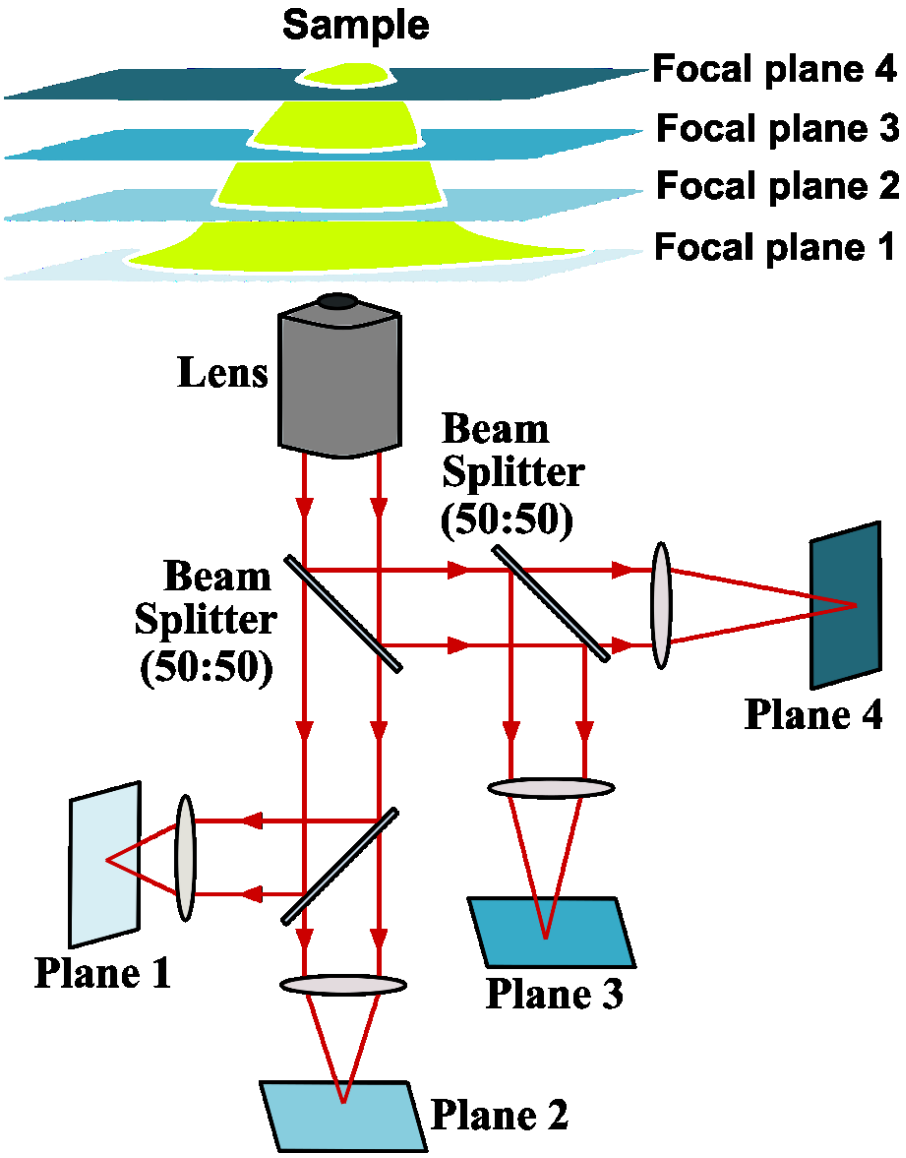

Figure 1.4 Schematic of MUM, configured to image four focal planes
The illustration shows a cell sample imaged using a multifocal plane microscopy (MUM) setup. After passing through the objective, the emitted signal is divided equally using beam splitters and focused onto four detectors. Different focal planes are imaged simultaneously by customizing the distances between the tube lenses and the detectors.

1.4.3. Three-Dimensional localization of single point sources

In the examination of biological samples using microscopy, experiments designed to yield images of isolated point sources of light are often desirable because we can more easily and accurately estimate the location of an isolated point source. The accuracy of estimation is dependent on the numerical aperture of the objective lens used, the emission wavelength, the number of detected photons, the pixel size of the detector, and noise sources in the microscope and detector (*149*). Two broadly different methods that utilize this approach of imaging point sources can be employed to extract spatial information from biological systems. One method involves the sample being sparsely labeled, such that only a few point sources are detected, thereby allowing us to estimate their locations with high certainty (*150*). The other method involves stochastically "switching on" only a subset of the fluorophores at a time, thereby also providing us with well-isolated point sources for accurate localization. This is performed repetitively using different subsets of the fluorophores, and the localization results are combined to form a high-resolution reconstruction of the biological sample (*151–153*). These methods rely on the ability to estimate the two- and three-dimensional location of a point source with high accuracy. This is often done by fitting the data to a parametric equation that models the image formation process of the microscope. The image of an in-focus point source is often approximated by an Airy profile, given by

$$I(x,y) = A\frac{J_1^2\left(\alpha\sqrt{(x-x_0)^2+(y-y_0)^2}\right)}{\pi((x-x_0)^2+(y-y_0)^2)},$$

where (x_0, y_0) is the location of the point source in the object space, and I is defined as the intensity at a point (x, y) on the detector. The parameter A represents the brightness of the point source,

while α denotes the width of the Airy profile, and J_1 denotes the first order Bessel function of the first kind (unit magnification is assumed for simplicity).

Another simple parametric equation that is commonly used for approximating the image of an in-focus point source is the 2D Gaussian profile, given by

$$I(x,y) = Ae^{-\left(\frac{(x-x_0)^2+(y-y_0)^2}{2\sigma^2}\right)},$$

where A and σ are parameters that denote the brightness of the point source and the width of the 2D Gaussian function, respectively. The 2D Gaussian profile provides a simple 2D parametric model of the PSF, while the Airy function better recapitulates its properties (*154*, *155*). Various approaches have been developed to detect and localize point sources effectively. A non-iterative state space-based localization method combines these steps and is capable of distinguishing very closely spaced molecules (*156*).

Parametric models are sufficient for estimating 2D locations, but may not be so for 3D localization. For example, the 2D Gaussian equation, when extended to the third dimension, results in a mismatch between the model and the data (*157*). Appropriate functions exist such that the 3D image can be parametrically modeled. The "Born and Wolf" model is a commonly used function where the imaging medium is modeled as a single layer of uniform refractive index (*133*), whereas the "Gibson and Lanni" model is a more realistic representation of the imaging system that models the imaging medium as multiple layers of different refractive indices (*158*, *159*).

The axial location of a point source near the focal plane is difficult to determine because very little information about it is encoded in the image, in this case, at least for some PSF models(*140*).

Various approaches have been developed to encode more information about a point source's axial location into the PSF (*137*, *143*, *145*). The MUM technique, described in Section 1.4.2 and Figure 1.4, solves the near-focus 3D localization problem as it simultaneously acquires the image of a point source from different focal planes. The advantage conferred by a MUM configuration is such that when a point source is near-focus with respect to one focal plane, it is out of focus with respect to the other focal planes. These images can be analyzed together to synergistically provide information for the estimation of the axial location of point sources (*160*). The aforementioned algorithm MUMLA is an optimization algorithm that can apply any of the parametric functions described above to estimate a point source's 3D location from images acquired using a MUM configuration (*145*, *146*). MUMLA has been shown to potentially provide the best theoretically possible localization accuracy if the applied PSF model reasonably approximates the PSF of the microscope (*145*).

1.4.4. Recent advances in 3D volumetric imaging

Recent advances in multi-resolution 3D imaging have enabled fast and efficient volumetric imaging of subcellular systems (*161*). In one particular study, the group demonstrates a design that utilizes three light-sheets to perform parallel 3D volumetric imaging of cytoskeletal dynamics at 600nm axial resolution and a high speed of up to 14 Hz (*162*). Multifocal approaches involving light sheets are well demonstrated in optically clear samples (e.g., larval zebrafish (*163*)) with isotropic resolution and in samples that are not clear, such as freely moving mice (*164*). Extended depth of focus (EDOF) imaging of systems with wavefront modulators for modulating the amplitude or phase of fluorescence has been applied to light sheet microscopy to produce lattice light sheets (*165*). Scanning-based strategies that result in quasi-volumetric imaging adopt PSF

engineering to increase the acquisition speed. Several examples of rapid volumetric imaging using scanning-based approaches in multi-photon microscopy are well documented (*166–168*). The laser focus is stretched from a Gaussian beam to a Bessel beam by inserting a spatial light modulator and a mask to generate an annular illumination in the pupil plane of a two-photon microscope (*169*). With the advent of fast acquisition using improved detection technologies, near-instantaneous multi-plane imaging in multi-photon microscopy is achieved by splitting the excitation light into time-delayed wavelets that can be focused onto the sample at different depths (*170*). This multi-photon multiplexing has been implemented to study neuronal activity in the mammalian brain (*171*), and a modified design of the same approach has been used to study Ca^{2+} signaling in the mouse brain (*172*).

1.4.5. Remote focusing multifocal plane microscopy (rMUM)

Our group recently introduced a new advanced imaging technology called remote-focusing multifocal plane microscopy (rMUM), which enables the imaging of single molecules in deep cellular samples at a high temporal and spatial resolution together with the visualization of the surrounding 3D cellular structures (*173*). The microscope setup comprises a MUM configuration (as detailed in Section 1.4.2, Figure 1.4) and a remote focusing configuration (Figure 1.5). MUM images single molecule trajectories in 3D space with high precision using MUMLA (*145*, *147*), while the remote focusing configuration images the 3D cellular structures to provide context for the recorded single molecule dynamics (*174–177*). The remote focusing configuration acquires a series of z-stack images rapidly independent of the MUM module.

A standard microscope is custom-fitted with the MUM module and the remote focusing microscopy module (r-module). The r-module is designed as proposed by Wilson et al. (*175*).

Figure 1.5 shows a schematic of the r-module. The primary objective lens (O1) of the standard microscope collects the emission of the sample, and the image is formed at the image plane using a tube lens (TL1). The r-module, which consists of two concatenated microscopy systems, is coupled after the image plane. Two objective lenses (O2 and O3) are placed opposing each other, such that a replica of the sample is formed at the intermediate focal plane between them. The second objective lens (O3) is placed on a piezo nanopositioner to allow the imaging of multiple intermediate focal planes. The z-stack images are captured using a camera (C1).

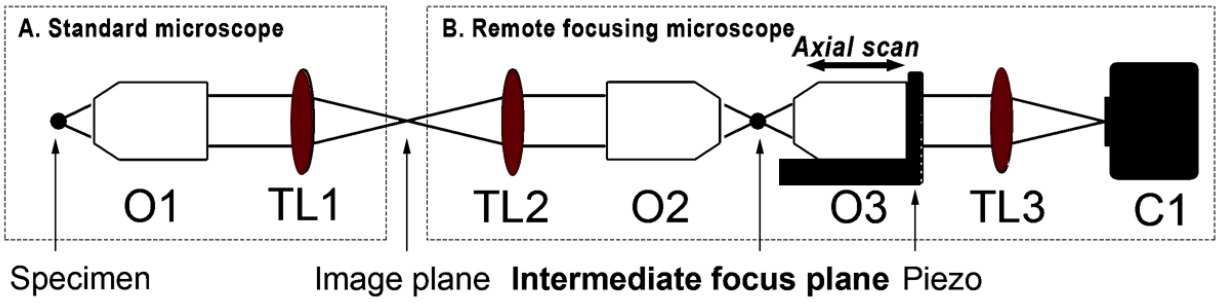

Figure 1.5 Schematic of the remote focusing microscopy module

The overall magnification M_R of the r-module is given by(*175*)

$$M_R = \left(\frac{n_2 F_2 M_2}{n_1 F_1 M_1}\right) \times \widehat{M}_3,$$

Here, M_1 and M_2 represent the magnifications of the objective lenses O1 and O2, F_1 and F_2 denote the focal lengths of the tube lenses TL1 and TL2, and n_1 and n_2 are refractive indices of the media corresponding to objective lenses O1 and O2, respectively. The total magnification of the subsystem is denoted by $\widehat{M}_3$. This rMUM system is also capable of multi-color volume imaging via the r-module.

1.5 Multimodality Imaging

Non-invasive in vivo imaging techniques, such as positron emission tomography (PET), computed tomography (CT), magnetic resonance imaging (MRI), and single-photon emission computed tomography (SPECT), are widely used adjunct to medical and surgical therapies or in diagnostic/theranostic settings (*178*). In general, these techniques are divided into two categories: anatomical and functional imaging. Based on the application, they can be utilized as single or hybrid modalities (i.e., PET/CT, PET/MRI, SPECT/CT). Anatomic imaging (CT and MR) provide great structural detail, while functional imaging (PET and SPECT) provides information about biological behavior (*179*, *180*).

1.5.1. Integrated PET/CT imaging

PET utilizes molecular probes that are labeled with positron emitting radioisotopes to image and quantify functional processes in vivo. These probes are called radiotracers and are used to visualize and measure physiological, metabolic, biochemical, and tumorigenic processes. Depending on the application and target within the body, different tracers are used for different purposes. A PET scanner can image positron emitting radionucleotides such as Fluorine-18, Carbon-11, Iodine-124, and Oxygen-15 at a spatial resolution of 2-5mm (*181*). The emitted positron encounters an electron, which leads to an annihilation reaction resulting in two photons of 511 keV, each with trajectories 180 degrees opposing each other. The PET/Gamma detectors accept coincident photons that hit the opposite sides of the rings within nanoseconds, thus improving the sensitivity of detection. By knowing the specific activity of the radiotracer (mCi/ug), the concentration of the delivered radiolabel to the tissue can be determined (*179*, *180*).

Advances in the processing power of computers along with volumetric x-ray imaging led to the development of CT imaging. CT generates 3D reconstructions of high resolution multiplane

x-ray images using advanced computationally expensive image reconstruction algorithms. Incorporating advanced camera technologies such as multi-detector CT (MDCT) yields even higher spatial resolution with shorter scan times (*182*, *183*). Each imaging modality has its own benefits and limitations. Hence, a combinatorial approach will be more powerful. PET imaging is limited by its relatively low spatial resolution and a lack of a clear anatomical reference which makes it difficult to accurately localize anatomic structures or accumulation of radiolabel. This is particularly important in oncological studies, which require the differentiation of radiolabel accumulation between healthy and pathological anatomical substrates. This can be achieved by combining this analytical imaging modality with an anatomical imaging technique such as CT that can give information about the structures. The development of software fusion algorithms permits the registration and merging of images acquired independently with high accuracy (*184*). Development of in-line CT and PET by integrating PET-CT systems in which the scanners are placed in tandem, allowing for sequential imaging, has led to absolute quantification of the radiolabel within a given intrinsic visceral organ (*185*).

1.6 Dissertation overview

The organization of the dissertation is as follows. Targets of cellular origin have become an important area of study with respect to antibody-dependent cellular phagocytosis (ADCP) due to the recent advent of monoclonal antibody therapeutics. Therapeutic antibodies opsonize the target and mediate the killing of tumor cells. However, the process involved after these antibodies opsonizing the tumor cells leading to degradation is not well established. In Section 2, the fate of antibody-opsonized tumor cells after undergoing whole-cell phagocytosis was studied using live-cell imaging microscopy. A vacuole-like structure was identified using various imaging modalities

and was found to be facilitating the degradation of large phagosomes with antibody-opsonized cancer cells.

In Section 3, a detailed analysis pipeline for imaging the trafficking behavior of single molecules interacting with its immediate cellular structures (here sorting endosomes) using remote focusing multifocal plane microscopy (rMUM) was studied. Remote focusing multifocal plane microscopy (rMUM) is an advanced imaging approach capable of three dimensional single molecule tracking and imaging of its cellular context at the same time. Two FcRn-inhibitors were imaged, and their interaction with sorting endosomes were studied in HMEC-1 cells. The actual single molecule trajectory of the single molecule interacting with the endosome was estimated for the FcRn-inhibitors. This is made possible only when the trajectories are compensated for the organelle's motion. This approach can be used to study different cellular contexts in biological systems.

Section 4 describes an approach that enables the selective capture of radiolabeled-target antibodies from the systemic circulation by engineered Fc-antigen protein and directing them to degradation. PET (positron emission tomography) was used to image the clearance and distribution of radiolabeled antibody in tumor-bearing mice. The contrast measures obtained from PET images was used as a variable to quantify the effectiveness of the target antibody's clearance.

2. PHAGOCYTOSIS OF ANTIBODY-OPSONIZED TUMOR CELLS LEADS TO THE FORMATION OF A DISCRETE VACUOLAR COMPARTMENT IN MACROPHAGE[*†]

2.1. Introduction

The process by which eukaryotic cells engulf and degrade particulate matter is known as phagocytosis (*97*). Specialized phagocytes such as macrophages are particularly active in this process. Fusion of endolysosomal compartments with the maturing phagosome as it acidifies results in the delivery of degradative enzymes followed by the destruction of phagosomal contents (*103*). Phagocytosed targets, such as mammalian cells, that approach the size of the phagocyte comprise a large proportion of the cellular content of a phagocyte, and as such, present unique challenges for degradation due to their relatively large size. By contrast with beads, which are typically used as models for the study of phagocytic processes, phagocytosed cells contain degradable content. Consequently, the release of metabolites such as amino acids during the degradation process could induce osmotic stress within the phagosome, causing it to increase in volume (*186*). Hence, effector cells may employ specific mechanisms during the degradative processing of cells within phagosomes in order to limit cellular stress.

The mechanistic target of rapamycin (mTOR) is a component of the mTOR complex 1 that localizes to lysosomes and acts as a sensor of nutrient availability and growth factor signaling (*187*, *188*). Specifically, this pathway is responsive to the accumulation of amino acids in the

---

[*] Reprinted with minor modifications, with permission from "Phagocytosis of antibody-opsonized tumor cells leads to the formation of a discrete vacuolar compartment in macrophages" by R. Velmurugan, S. Ramakrishnan, M. Kim, RJ Ober, ES Ward, 2018. *Traffic*, vol. 19, no. 4, pp. 273-284, Copyright 2018 by The Authors (*86*).

[†] Part of this data reported in this Section is reprinted with permission from "Using Advanced Microscopy Techniques for the Study of Macrophage-Cancer Cell Interactions in the Presence of Therapeutic Antibodies" by R. Velmurugan, 2017. (Doctoral Dissertation) (*275*)

lysosomal lumen (*189*). This suggests that the degradation of cells within phagosomes, or in entotic vacuoles that arise from live cell engulfment by neighboring cells ('entosis')(*190*), may be coordinated by the mTOR pathway, particularly in cases where the degradation process leads to amino acid release (*191*). Nevertheless, recent studies have revealed the complexity of the pathways, including mTOR-independent processes,that play a role in entotic vacuole or phagosome maturation and fission to generate lysosomes (*192–195*).

The study of cellular phagosomes is directly relevant to antibody-dependent cellular phagocytosis (ADCP) of targets such as tumor cells. Antibodies represent a rapidly expanding class of therapeutics for the treatment of cancer (*196*). The recognition of tumor-specific antigens by therapeutic antibodies results in coating, or opsonization, of the cancer cells which can lead to ADCP (*88*, *105*). The presence of macrophages as the most abundant immune cell type in the majority of tumors (*106*), suggests that macrophage-mediated ADCP may contribute to the anti-tumor effects of antibodies. Although macrophages can have pro-tumorigenic consequences, results from multiple studies are consistent with a contribution of macrophage-mediated effector activity to tumor cell death (*83*, *89*, *197–201*). Further, antigen can be processed from these phagosomes and presented in the context of major histocompatibility complex class I or II molecules to cognate T cells (*202*, *203*). Hence, studying the maturation pathway of cellular phagosomes is expected to be of direct relevance to the successful use of therapeutic antibodies and induction of anti-tumor immunity.

In the current study, we have analyzed the fate of phagosomes containing antibody-opsonized cancer cells within macrophages. Interestingly, we observe the formation of a distinct phagosome-associated vacuole during phagosome maturation. This phagosome-associated vacuole is separated from the phagosome by a barrier that selectively restricts diffusion of solutes

between the two compartments based on their size. Further, vacuoles are not detected following the phagocytosis of antibody-opsonized beads, indicating that cellular components within the phagosome may regulate vacuole formation. In addition, vacuole enlargement was observed in the presence of the mTOR inhibitor, torin 1. Collectively, our results suggest that this vacuole is a common feature associated with the degradation of cellular targets by phagocytes.

2.2. Materials and methods

2.2.1. Cell lines and primary cells

The cell lines J774A.1 (Cat# TIB-67, RRID: CVCL_0358), SK-BR-3 (Cat# HTB-30, RRID: CVCL_0033), Raji (Cat# CCL-86, RRID: CVCL_0511) and MDA-MB-453 (Cat# HTB-131, RRID: CVCL_0418) were purchased from the American Type Culture Collection. The cell lines were maintained in the following media supplemented with 10% fetal calf serum (FCS; Catalog no. 100-106, Gemini Bioproducts): macrophages and Raji cells, phenol red-free Dulbecco's Modified Eagle Medium (11965-092); MDA-MB-453, RPMI-1640 (11875-093); SK-BR-3, McCoy's (16600082). All experiments were conducted in medium containing FCS depleted of immunoglobulin G (*41*). Long-term live imaging of macrophages was performed in Leibovitz's L-15 medium (11415-064) containing 10% FCS. Media were purchased from Thermo Fisher Scientific. Identities of the cancer cell lines were authenticated by short tandem repeat analysis (University of Arizona Genetics Core). Human monocytes were purchased frozen (Catalog no. 1008, Astarte Biologics) or were purified from peripheral blood mononuclear cells (kindly provided by Darrell Pilling, Texas A&M University) using the EasySep Human Monocyte Enrichment Kit (Catalog no. 19059, Stemcell Technologies). The monocytes were cultured in DMEM containing 10% FCS supplemented with 50 ng/ml macrophage-colony stimulating factor (Catalog no. 300-25, Peprotech) in MatTek glass bottom dishes (Catalog no. P35G-1.5-10-C).

Bone marrow-derived macrophages were isolated from C57BL/6J mice (purchased from The Jackson Laboratory) as described previously (*204*).

2.2.2. Antibodies and other reagents

Clinical-grade trastuzumab, rituximab and IVIG (Gammunex) were obtained from the UT Southwestern Pharmacy. Trastuzumab and rituximab were labeled using Alexa 488 or 555 labeling kits (Thermo Fisher Scientific). The antibodies were labeled with 3-5 fluorophores per protein molecule. Trastuzumab was biotinylated as described previously (*25*). Lysotracker Red (L7528), LysoSensor Blue DND-192, Alexa 488, 555, 647 and pHrodo Red-labeled dextran (10 kDa molecular weight; D-22910, D34679, D-22914 and P10361, respectively), FM 4-64FX (F34653), Alexa 555-labeled human transferrin (T35352), Alexa 647-labeled Annexin V (A23204), Alexa 488, 555 and 647-labeled goat anti-rabbit IgG (H+L) secondary antibody (A-11034; RRID: AB_2576217, A-21429; RRID: AB_141761 and A-21245; RRID: AB_2535813, respectively), Alexa 647-labeled goat anti-mouse IgG (H+L) secondary antibody (A-21236; RRID: AB_141725) and $F(ab')_2$-goat anti-human IgG (H+L) secondary antibody conjugated Qdot 655 nanoparticles (Q-11221MP; RRID: AB_2556468) were purchased from Thermo Fisher Scientific. Rabbit monoclonal antibodies specific for phosphorylated S6 ribosomal protein (D68F8; Cat#5364, RRID: AB_10694233), specific for phosphorylation at Ser240 and Ser244 residues and mTOR (Clone 7C10; Cat# 2983, RRID:AB_2105622) were purchased from Cell Signaling Technology. Rat anti-mouse LAMP-1 (Cat#1D4B; RRID: AB_2134500) was purchased from the Developmental Studies Hybridoma Bank. FITC-labeled rat anti-mouse CD45 (Clone 30-F11,Cat# 553079; RRID: AB_394609) was purchased from BD Biosciences. Tetramethylrhodamine isothiocyanate-labeled dextran with average molecular weights of 155 kDa (T1287) or 65-85 kDa (represented as 75 kDa; T1162) were purchased from Sigma-Aldrich. Torin 1 (235-t-7887) was

purchased from LC Labs. 10 μm-diameter streptavidin-coated beads (CP01N) were purchased from Bangs Laboratories. All experiments were performed in cells plated in MatTek glass bottom dishes.

2.2.3. Sample pretreatment

For imaging phagosomes containing engulfed cancer cells, macrophages were first plated in MatTek glass bottom dishes. J774A.1 macrophages were plated overnight in the presence of 25 ng/ml murine interferon-γ (Catalog no. 315-05, Peprotech). Mouse bone marrow-derived macrophages were similarly activated overnight with interferon-γ. Purified human monocytes were directly plated in MatTek glass bottom dishes 6 days prior to the experiment. Human macrophages were activated with human interferon-γ overnight. To label the lysosomes of macrophages with dextran, the macrophages were incubated with medium containing 100 μg/ml labeled dextran for 1 hour, washed and incubated with medium for 2-4 hours prior to the addition of target cells. To label cancer cell lysosomes with dextran, cells were either pulse-chased (2 hours pulse, 4 hours chase) or incubated for 12 hours with 100 μg/ml dextran, followed by incubation with medium for 4 hours prior to addition to the macrophages.

2.2.4. Phagocytosis of cancer cells by macrophages

The cancer cells were harvested from flasks by mild trypsinization, washed and incubated with 10 μg/ml labeled opsonizing antibody for 10 minutes at room temperature. The cells were then washed twice with phosphate-buffered saline (PBS) followed by re-suspension in medium. Cancer cells were added to macrophages at 1:0.875 effector:target ratios (35,000 target cells were added to 40,000 plated macrophages in 10 mm MatTek glass bottom dishes) and incubated for various time points before imaging. When indicated in the Figure legends, the medium in the dishes was replaced with medium containing 10 mg/ml IVIG to block further phagocytosis

following one hour of co-culture. In a subset of experiments, Lysotracker Red (2 nM) and Lysosensor Blue (50 nM) were added to the medium and incubated at room temperature for 5 minutes to label the acidic compartments. For immunofluorescence using J774A.1 macrophages, cells were fixed in 1:1 methanol:acetone at -20 °C for 5 minutes.

2.2.5. Flow cytometry analyses

For flow cytometry analyses, co-cultures of macrophages and cancer cells were prepared as described above. One hour later, 10 mg/ml IVIG was added to block further phagocytosis and cells were treated with 100 nM torin 1 or vehicle (DMSO) for an additional 6 hours. As controls, MDA-MB-453 cells treated with rituximab (anti-CD20) and MDA-MB-453 cells without antibody were used. Following the incubation, cells were harvested, fixed with 2% paraformaldehyde for 10 minutes at 37 ºC, permeabilized with methanol for 30 minutes at -20 ºC, and stained with FITC-labeled mouse CD45-specific antibody and rabbit monoclonal antibody specific for pS6. Alexa 647-labeled anti-rabbit antibody was used to detect the pS6-specific antibody. Following staining and washing, stained cells were analyzed using flow cytometry (Accuri). Flow cytometry data were processed using FlowJo software (FlowJo, RRID: SCR_008520).

2.2.6. EM sample preparation

Cells were fixed on gridded MatTek dishes (Catalog no. P35G-1.5-14-CGRD-D) with 2.5% (v/v) glutaraldehyde in 0.1M sodium cacodylate buffer. After three rinses in 0.1 M sodium cacodylate buffer, they were post-fixed in 1% osmium tetroxide and 0.8 % K3[Fe(CN6)] in 0.1 M sodium cacodylate buffer for 1 h at room temperature. Cells were rinsed with water and en bloc stained with 2% aqueous uranyl acetate overnight. After three rinses with water, specimens were dehydrated with increasing concentrations of ethanol, infiltrated with Embed-812 resin and polymerized in a 60°C oven overnight. Blocks were sectioned with a diamond knife (Diatome) on

a Leica Ultracut UC7 ultramicrotome (Leica Microsystems) and collected on copper grids, followed by post-staining with 2% uranyl acetate in water and lead citrate. Images were acquired using a Tecnai G2 Spirit transmission electron microscope (FEI) equipped with a LaB6 source using a voltage of 120 kV.

2.2.7. Microscope configurations

For single time-point imaging, images were acquired using a Zeiss Axiovert 200M inverted fluorescence microscope with a Zeiss 63x/1.4NA Plan Apochromat objective as described previously (*67*). Long-term live imaging of the formation of the vacuole was imaged using a Zeiss Axio Observer.A1 body and a Zeiss 63x/1.4NA Plan Apochromat objective. The sample was illuminated with a 488-nm solid-state laser (Coherent) for Alexa 488 excitation and a 543-nm diode laser (Opto Engine LLC) for Alexa 555 excitation. The illumination was directed to the sample and fluorescence filtered back using a polychroic beam splitter/emission filter combination (488/543/633 RPC and 488/543 M; Chroma Technology Corporation). The fluorescence emission was detected using an Andor iXon EMCCD camera (Andor Technologies). The cameras were run on conventional gain mode and images were acquired in two colors along with a transmitted light image at an acquisition rate of 1 block per minute. Camera acquisition and shuttering of excitation lasers were controlled using custom acquisition software written in LabWindows/CVI (National Instruments Corporation). The acquired images were registered and processed using the Microscopy Image Analysis Tool (http://wardoberlab.com/software/miatool)(*205*) implemented in MATLAB (MathWorks, Inc; RRID: SCR_001622). The temperature and humidity in the microscope system were maintained by a caged temperature-control system (OKOlabs). Long-term imaging of the degradation of the vacuoles, the imaging of LysoSensor and of the different molecular weight dextrans were performed using a Nikon A1R confocal microscope equipped with

a 60X 1.4 NA Plan Apo objective and a temperature-control system. The acquired images were exported to TIFF format and processed with Microscopy Image Analysis Tool as described above.

2.2.8. Statistical analyses

Tests for statistical significance between groups were carried out using student's *t*-test or one-way ANOVA with Tukey's multiple comparison test in GraphPad Prism software, V6.0 (http://www.graphpad.com, RRID: SCR_002798). p values of less than 0.05 were considered to be significant.

2.3. Results

2.3.1. Identification of a phagosome-associated vacuole

Initially, we used live cell microscopy to analyze the phagocytic process involving J774A.1 macrophages as effectors and MDA-MB-453 breast cancer cells as targets. MDA-MB-453 cells were opsonized with Alexa 555-labeled HER2-specific antibody (trastuzumab) and co-incubated with macrophages that had been preloaded with Alexa 647-labeled dextran to identify lysosomes. At approximately three hours following phagocytosis, we observed the formation of a vacuole-like structure with a clear phase-contrast profile adjacent to the phagosome (Figure 2.1 A). Time-lapse images showed a gradual increase in the size of this vacuole over 2-6 hours (Figure 2.1 A). We observed that the vacuole and phagosome were positive for both Alexa 647 and Alexa 555 fluorophores (Figure 2.1 B), indicating that the vacuole contains both lysosomal components and opsonizing antibody (fragments) derived from the macrophages and cancer cells, respectively. In addition, the proportion of labeled dextran derived from macrophage lysosomes that is associated with phagosome/vacuole compartments relative to that in 'free' lysosomes in macrophages was quantitated and ranged from 20-60% (n = 9), suggesting a high frequency of lysosomal fusion with the phagosome and/or vacuole (Figure 2.1 C).

We next investigated the time-course of the formation of the vacuole. Antibody-opsonized target cells were mixed with macrophages, and intravenous immunoglobulin (IVIG) was added to the conjugates following 1 hour to prevent further phagocytosis (by competitive inhibition of Fcγ receptor binding(*89*)). The numbers of phagosomes containing an associated vacuole following a 2, 4, 6 or 8-hour incubation period following the addition of IVIG were quantitated by microscopy. This quantitation showed that the percentage of phagocytosed cells with associated vacuoles is maximal at ~75% (n = 150) at 6 hours following the addition of IVIG to block further phagocytosis, and this percentage decreases to ~50% (n = 148) at 9 hours (Figure 2.1 D).

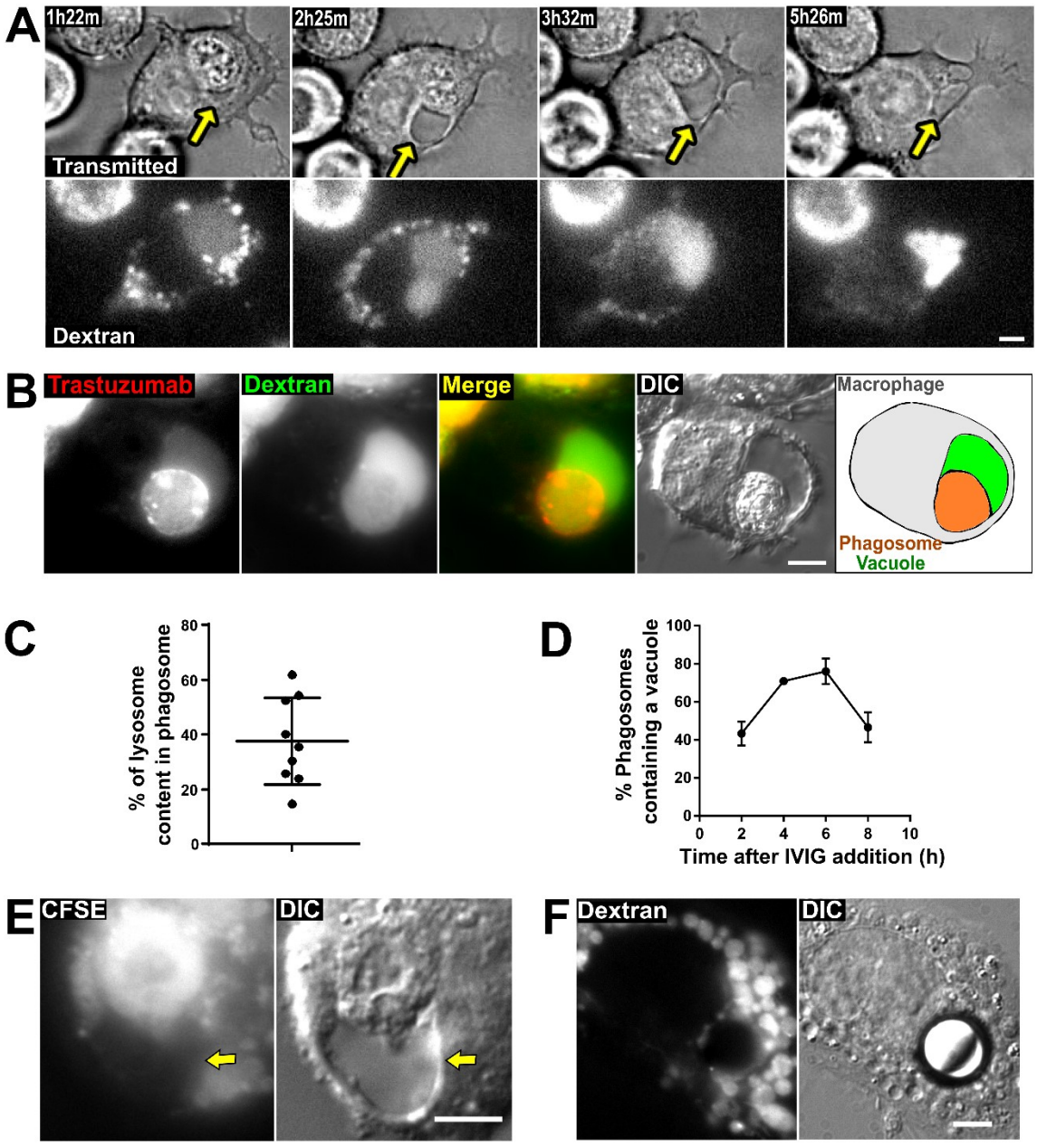

Figure 2.1 Phagosomes containing cancer cells have associated vacuoles

A, MDA-MB-453 cancer cells were opsonized with Alexa 555-labeled trastuzumab and co-incubated with J774A.1 macrophages for 1 hour. The macrophages were preloaded with Alexa 647-labeled 10 kDa dextran. A macrophage containing a phagocytosed target cell was identified and imaged live for 12 hours. The images show transmitted light and dextran fluorescence for this macrophage at the indicated time points following the start of imaging. B, Fluorescent and DIC

images of a phagosome from a sample prepared as in A following a 4.5-hour incubation. Alexa 555 (trastuzumab) is pseudocolored red, and Alexa 647 (dextran) is pseudocolored green. The right-hand panel shows a schematic diagram of the approximate location of the phagosome-associated vacuole (green), the phagosome containing the corpse of the target cell (orange) and the boundary of the macrophage (gray). C, J774A.1 macrophages were preloaded with Alexa 488-labeled 10 kDa dextran and co-incubated with MDA-MB-453 cancer cells opsonized with trastuzumab for 6 hours. z-stack images of cells (n = 9 phagosomes) were taken and the proportion of labeled dextran associated with the phagosome/vacuole compartments relative to that in 'free' lysosomes in macrophages was quantitated. Error bars represent standard errors. D, MDA-MB-453 cells were opsonized with Alexa 488-labeled trastuzumab and co-incubated with J774A.1 macrophages preloaded with Alexa 647-labeled 10 kDa dextran. After co-incubation for 1 hour, 10 mg/ml IVIG was added to prevent further phagocytic activity. Fluorescent and DIC images of the phagosomes were then taken at the indicated time points following IVIG addition, and the phagosomes with an associated vacuole were counted. Error bars represent standard errors. E, MDA-MB-453 cancer cells were preloaded with FITC-labeled CFSE, UV-irradiated for 3 hours to induce apoptosis and subsequently co-incubated with J774A.1 macrophages for 1 hour followed by the addition of 10 mg/ml IVIG and incubation for a further 6 hours followed by imaging. Fluorescent and DIC images are shown. F, Streptavidin-coated beads (10 μm diameter) were opsonized with biotinylated trastuzumab, washed and added to J774A.1 macrophages. The macrophages were preloaded with Alexa 647-labeled 10 kDa dextran. The cells were subsequently incubated for 1 hour followed by the addition of 10 mg/ml IVIG and incubation for a further 6 hours followed by imaging. Fluorescent and DIC images are shown. Yellow arrows in A and E indicate the position of the vacuole. For panels A, B, E and F, images of representative cells from at least 12 cells are shown. Data for all panels are representative of at least two independent experiments. Scale bars = 5 μm.

We also analyzed whether vacuoles form following the engulfment of apoptotic bodies by macrophages. Target cells were exposed to UV irradiation to induce apoptosis, and the resulting apoptotic bodies were incubated with macrophages for 7 hours followed by microscopy analyses

(n = 68 apoptotic vacuoles; Figure 2.1 E). Flow cytometric analyses using fluorescently labeled annexin V confirmed the induction of apoptosis (Figure 2.2).

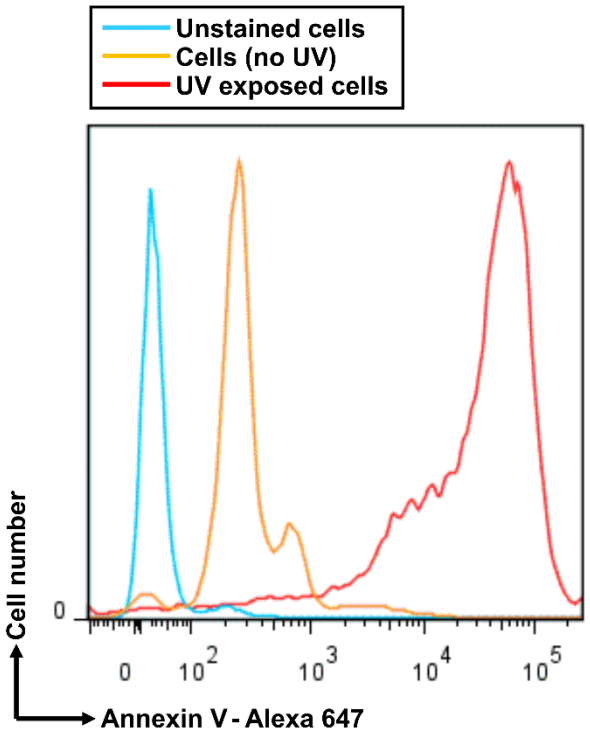

Figure 2.2 Flow cytometric analyses of induction of apoptosis in MDA-MB-453 cancer cells
MDA-MB-453 cancer cells were plated overnight and UV-irradiated for 3 hours, followed by harvesting of non-adherent cells/apoptotic bodies. As a control, cells were not exposed to UV irradiation and harvested by trypsinization. Cells/apoptotic bodies were stained with Alexa 647-labeled Annexin V. Histogram plot shows flow cytometry analyses for control and apoptotic cells. Data shown are representative of two independent experiments.

These studies revealed that vacuoles form adjacent to phagosomes containing apoptotic bodies. Interestingly, by contrast with phagocytosed cancer cells or apoptotic bodies, vacuoles

were not detected in macrophages that had phagocytosed streptavidin coated, 10 µm diameter latex beads coupled to biotinylated trastuzumab (n = 128 phagocytosed beads; Figure 2.1F).

2.3.2. The phagosome and vacuole are LAMP-1+ and their contents are redistributed into lysosomes

Consistent with the fusion of lysosomes with maturing phagosomes and associated vacuoles, staining of macrophages following phagocytosis of cancer cells with a LAMP-1-specific antibody demonstrated that the limiting membranes of both phagosomes and vacuoles have associated LAMP-1 (Figure 2.3 A). By contrast with the analyses of lysosomal markers, pulsing of J774A.1 macrophage: MDA-MB-453 co-cultures with Alexa 555-labeled transferrin indicated that phagosomes and associated vacuoles do not have detectable levels of this early/recycling endosomal marker (Figure 2.3 B).

To further characterize the fate of the vacuole, co-cultures of macrophages and opsonized cancer cells were incubated for 6 hours and phagosome-associated vacuoles in these samples were analyzed by long-term live cell imaging. In this experiment, the lysosomes of the target cells were labeled instead of trastuzumab, to distinguish phagocytosis from trogocytosis (‘nibbling,' in which membrane fragments, but not lysosomes of the target cell accumulate in macrophages)(*89*, *124*, *206*).

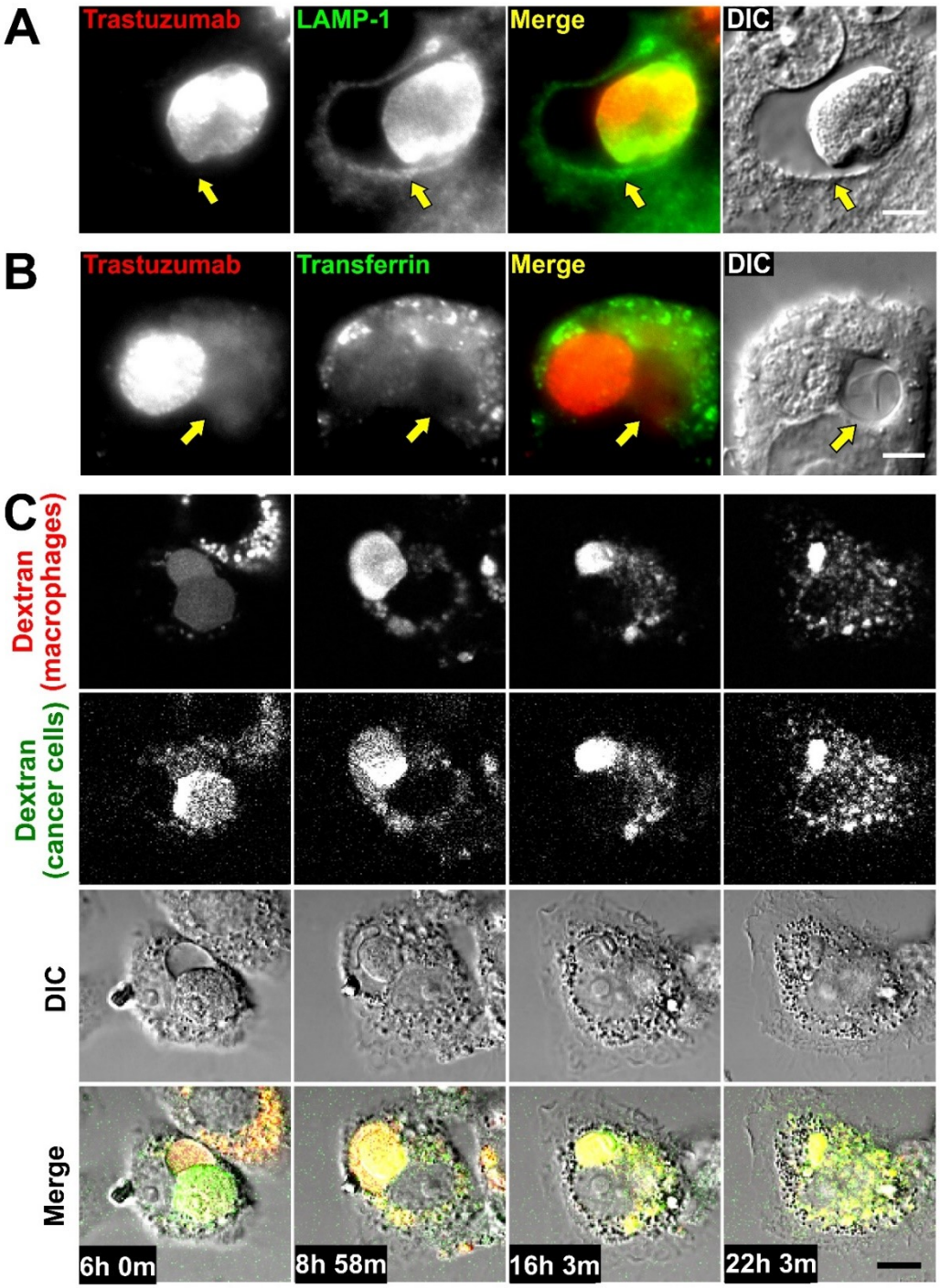

Figure 2.3 The phagosome and vacuole are LAMP-1+ and their contents are redistributed throughout the lysosomal network of the macrophage

A, MDA-MB-453 cancer cells were opsonized with Alexa 488-labeled trastuzumab and co-incubated with J774A.1 macrophages for 1 hour followed by addition of 10 mg/ml IVIG and incubation for a further 6 hours. Cells were fixed, permeabilized, and LAMP-1 was detected using

a LAMP-1 specific antibody followed by an Alexa 647-labeled secondary antibody. Fluorescent and DIC images are shown, with Alexa 488 (trastuzumab) pseudocolored red, and Alexa 647 (LAMP-1) pseudocolored green. B, MDA-MB-453 cancer cells were opsonized with Alexa 488-labeled trastuzumab and co-incubated with J774A.1 macrophages for 1 hour followed by addition of 10 mg/ml IVIG and incubation for a further 6 hours. Cells were pulsed with 10 μg/ml Alexa 555-labeled human transferrin at 37 °C for the last 10 minutes of the incubation and then cells were washed and imaged as live cells. Fluorescent and DIC images are shown, with Alexa 488 (trastuzumab) pseudocolored red and Alexa 555 (transferrin) pseudocolored green. C, MDA-MB-453 cancer cells opsonized with trastuzumab were co-incubated with J774A.1 macrophages. The cancer cells were preloaded with Alexa 555-labeled 10 kDa dextran (pseudocolored green), and the macrophages were preloaded with Alexa 488-labeled 10 kDa dextran (pseudocolored red). Imaging (fluorescence and DIC) was initiated 6 hours following the start of the co-incubation. The panels show 4 frames from the time series, with times corresponding to each frame indicated. Yellow arrows in A and B indicate the position of the vacuole. Images of representative cells from at least 14 cells and 2 independent experiments are shown. Scale bar = 5 μm.

Time-lapse images from long-term imaging reveal that as the phagosome-associated vacuoles begin to decrease in size around 8 hours, the dextran originating from the target cell, which was initially present in both the phagosome and the vacuole, redistributes throughout the lysosomal network of the macrophage during the following 14 hours (Figure 2.3 C). Similar results were obtained when the lysosomes in cancer cells, but not in macrophages, were labeled with Alexa 488-labeled dextran (Figure 2.4). These analyses indicate that the phagosome-associated vacuole is a temporary structure formed during the maturation of phagosomes and that the contents of the vacuole are subsequently redistributed into the lysosomal network.

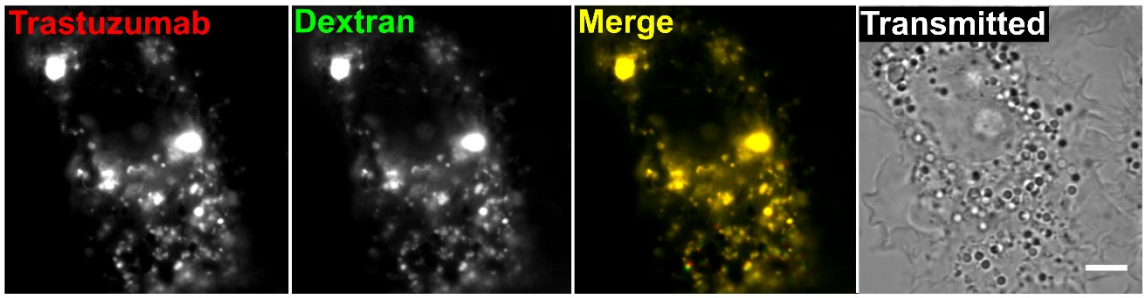

Figure 2.4 Redistribution of cancer cell content into the lysosomal network of macrophages
MDA-MB-453 cells were pulse-chased (2 hours pulse, 4 hours chase) with 100 µg/ml Alexa 647-labeled 10 kDa dextran (pseudocolored green) to label lysosomes, followed by opsonization with Alexa 555-labeled trastuzumab (pseudocolored red) and co-incubation with J774A.1 macrophages for 24 hours. Fluorescent and DIC images of a representative cell from at least 16 cells and 2 independent experiments are shown. Scale bar = 5 µm.

2.3.3. The phagosome and vacuole are discrete compartments

To investigate whether the vacuole is lysosomal in nature, we treated samples containing phagosome-associated vacuoles with the dye LysoTracker Red, which is membrane permeant and accumulates through trapping by protonation in acidic compartments, including lysosomes(*207*). Interestingly, although the phagosome was, as expected from earlier studies(*191*), positive for LysoTracker, the dye was undetectable in the phagosome-associated vacuole (Figure 2.5 A). To further explore the properties of the vacuole, we treated the samples with LysoSensor Blue DND-192, that is also membrane permeant and protonated in acidic compartments(*208*). As expected, the phagosome was positive for LysoSensor Blue fluorescence. Although the intensity of the LysoSensor staining in the vacuole was lower relative to that in the phagosome, LysoSensor signal could be detected in the vacuolar region, by contrast with very low to undetectable levels of LysoTracker signal (Figure 2.5 B).

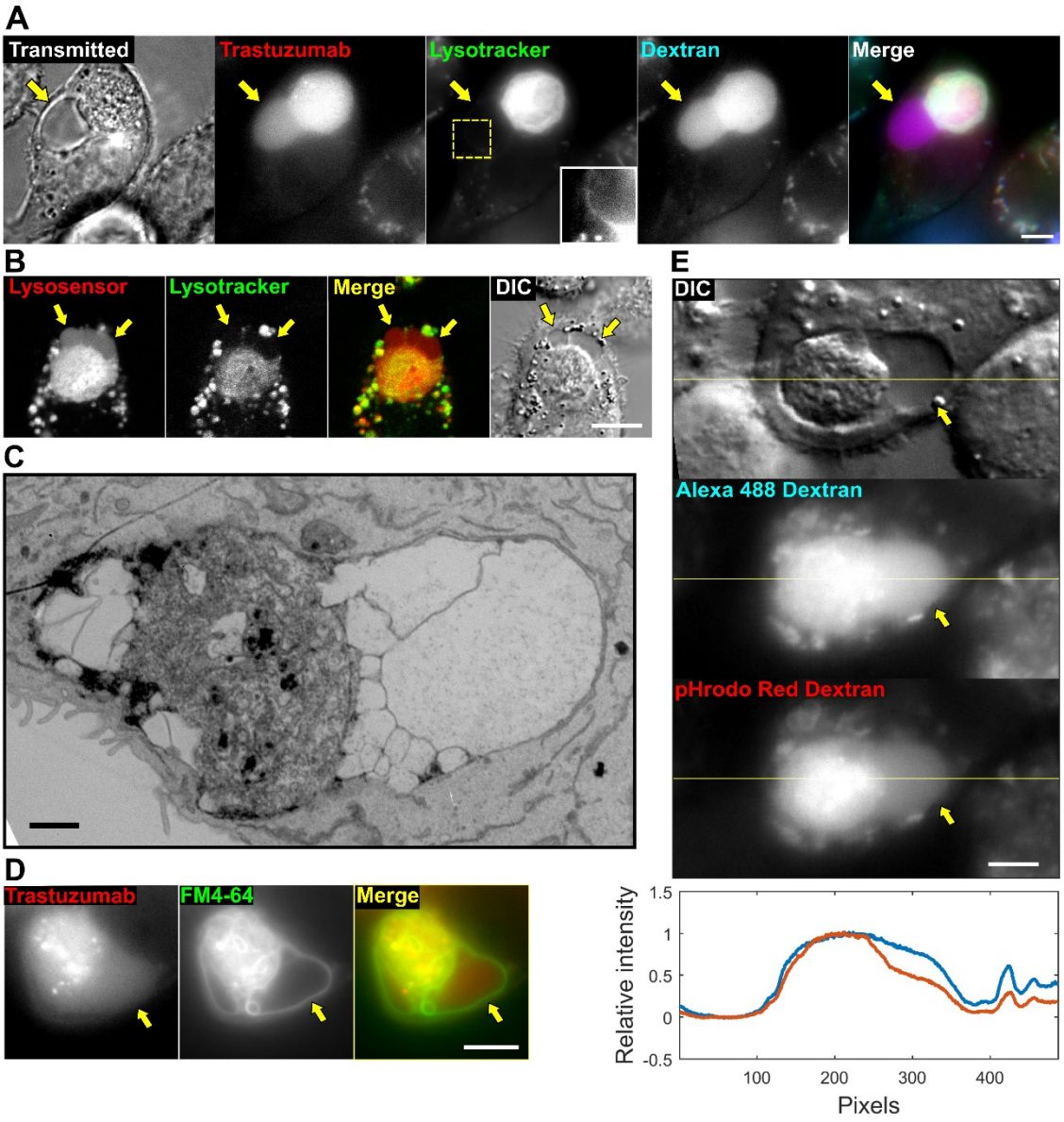

Figure 2.5 The vacuole contains membranous subcompartments

A, MDA-MB-453 cells were opsonized with Alexa 488-labeled trastuzumab (pseudocolored red), added to J774A.1 macrophages preloaded with Alexa 647-labeled 10 kDa dextran (pseudocolored blue), and incubated for 13 hours. Lysotracker Red (pseudocolored green) was then added to the medium, and the cells were imaged (transmitted light and fluorescence). The inset in the center panel corresponds to an enlargement of the cropped area (dotted lines) to show the region of interest with enhanced contrast. B, MDA-MB-453 cells were opsonized with trastuzumab and co-incubated with J774A.1 macrophages, and incubated for 6 hours. LysoSensor Blue (pseudocolored

red) and LysoTracker Red (pseudocolored green) were then added to the medium, and the cells were imaged (fluorescence and DIC). C, MDA-MB-453 cells opsonized with trastuzumab were added to J774A.1 macrophages, incubated for 6 hours, fixed and processed for EM. An EM image of a phagosome with associated vacuoles is shown (representative of 9 phagosomes). D, MDA-MB-453 cells were harvested, labeled with the FM 4-64FX dye (pseudocolored green), opsonized with Alexa 488-labeled trastuzumab (pseudocolored red) and co-incubated with J774A.1 macrophages. Co-cultures were then incubated for 6 hours and imaged (fluorescence). E, MDA-MB-453 cancer cells opsonized with trastuzumab were co-incubated with J774A.1 macrophages that were preloaded with an equimolar mixture of pH-insensitive Alexa 488- and pH-sensitive pHrodo Red-labeled 10 kDa dextran (50 μg/ml each) for 1 hour followed by addition of 10 mg/ml IVIG and incubation for a further 6 hours. Fluorescent and DIC images are shown, with a line drawn across the phagosome/vacuole. Line intensity plot represents the normalized intensity between the two fluorescent signals (Alexa 488 and pHrodo Red, shown in blue and red, respectively) detected along the yellow line. Data for each fluorophore are normalized against the maximum signal level. The ratio of fluorescent intensities in the phagosomes and vacuoles were quantitated and 60% (n = 110) of vacuoles were found to have lower pHrodo Red:Alexa 488 intensity ratios compared with adjacent phagosomes. Yellow arrows in A, B, D and E indicate the location of the vacuole, and images of representative cells from at least 39 cells and 2 independent experiments are shown. Scale bars = 5 μm (A, B, D and E) or 1 μm (C).

Although the vacuole had very low to undetectable levels of fluorescent signal from LysoTracker, we detected higher levels of fluorescence around the limiting membrane of the vacuole, suggesting that this membrane might be multilamellar (Figure 2.5 A, inset). Hence, to further understand the ultrastructural properties of the vacuole, we prepared specimens of phagocytosed target cells for analysis using transmitted electron microscopy (TEM). EM images showed that the vacuoles had very low density compared with the surrounding cytoplasm, whilst the target cell corpse had a morphology analogous to that observed by others for cellular

phagosomes (Figure 2.5 C) (*209*). The EM images of the vacuole also displayed membrane-limited subcompartments within this structure. To determine whether these membrane subdivisions are also found inside phagosome-associated vacuoles in live specimens, the target cells were labeled with the membrane dye FM 4-64FX before co-incubation with the macrophages. Analyses of phagosome-associated vacuoles with these FM dye-labeled targets revealed that this dye labeled the limiting membranes of subcompartments within the vacuolar region (Figure 2.5 D).

To further investigate whether the phagosome and vacuole have distinct properties, we preloaded macrophages with an equimolar mixture of Alexa 488- and pHrodo Red-labeled 10 kDa dextran prior to co-incubation with antibody-opsonized tumor cells. The fluorescent signal of pHrodo Red increases as the pH becomes more acidic, whereas that of Alexa 488 is constant across a broad pH range of 4-10 (*210*). The ratios of fluorescent intensities of pHrodo Red:Alexa 488 in the phagosomes and vacuoles were determined, and for 60% (n = 110) of vacuoles were found to be lower than those of adjacent phagosomes, whereas for the remaining 40%, the ratio was similar in both compartments (Figure 2.5 E, Figure 2.6). Collectively, these data suggest that the pH of the vacuole can be higher than that of the phagosome.

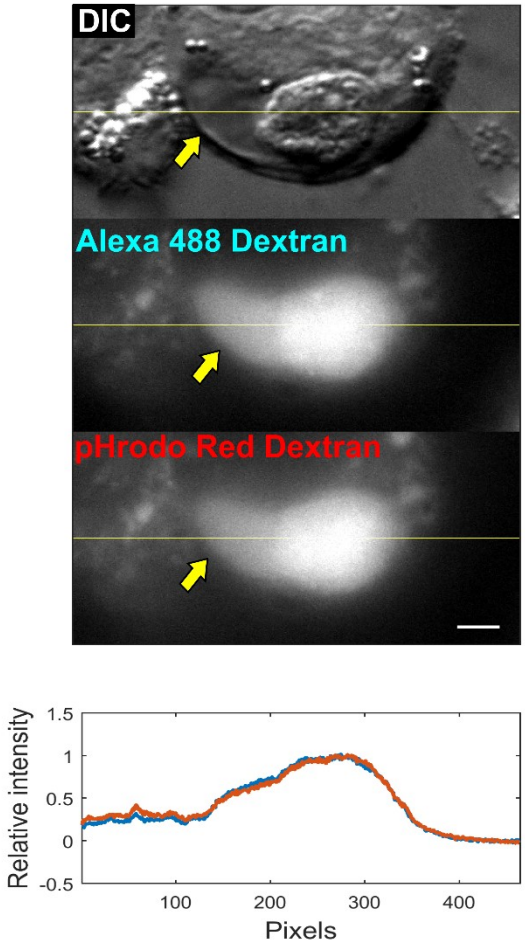

Figure 2.6 Status of pH in the phagosome and associated vacuole using pH-sensitive and insensitive dye conjugated dextran

J774A.1 macrophages preloaded with dextran were co-incubated with MDA-MB-453 cancer cells opsonized with trastuzumab as described in the legend for Fig. 2.5E. Fluorescent and DIC images are shown, with a line drawn across the phagosome/vacuole. Line intensity plot represents the normalized intensity for the two fluorescent signals (Alexa 488 and pHrodo Red, shown in blue and red, respectively) detected along the yellow line. Data for each fluorophore are normalized against the maximum signal level. The ratio of fluorescent intensities in the phagosomes and vacuoles were quantitated and 40% (n = 110) of vacuoles were found to have similar pHrodo Red:Alexa 488 intensity ratios in both the vacuole and adjacent phagosome. Yellow arrows indicate the location of the vacuole, and images of a representative cell from 110 cells and 3 independent experiments are shown. Scale bar = 5 μm.

2.3.4. The vacuole and phagosome are separated by a semi-permeable membrane

In combination with the EM data, the differential accumulation of LysoTracker and LysoSensor in the vacuole suggested that the phagosome and vacuole are discrete compartments. However, the accumulation of Alexa Fluor dye following phagocytosis of cancer cells opsonized with Alexa 555-labeled trastuzumab indicated that some macromolecules could transfer between the compartments. To investigate whether the barrier between these two compartments limits movement of solutes above a particular size threshold, we labeled the surface of target cells with QDot 655-labeled trastuzumab. These quantum dot nanoparticles have an approximate diameter of 20 nm (*211*). Vacuoles associated with phagosomes containing target cells did not contain any quantum dots, indicating that the barrier is impermeant to these nanoparticles (Figure 2.7 A).

Previous studies have used fluorescently labeled dextrans of different molecular weights to investigate the effect of size on subcellular transport processes (e.g. phagosomal-lysosomal and lysosomal fusion) (*212*, *213*). We therefore labeled the lysosomes of the macrophage with fluorescent dextrans of different molecular weights (65-85 kDa, referred to as 75 kDa, and 155 kDa) and subsequently co-incubated these cells with trastuzumab-opsonized cancer cells. As a control, lysosomes of the macrophage were also labeled with 10 kDa dextran. When 75 kDa and 10 kDa dextrans were preloaded together in macrophage lysosomes, both dextrans accumulated in the vacuoles (n = 40) to similar levels (Figure 2.7 B). However, when 155 kDa and 10 kDa dextrans were preloaded together in macrophage lysosomes, the accumulation of 155 kDa dextran was substantially lower compared with 10 kDa dextran in the majority (81%, n = 71 phagosomes) of the vacuole compartments. The differential vacuolar localization of these dextrans and quantum

dot nanoparticles indicates that the barrier between the phagosome and the vacuole can exclude the transfer of molecules/particles above a particular size threshold.

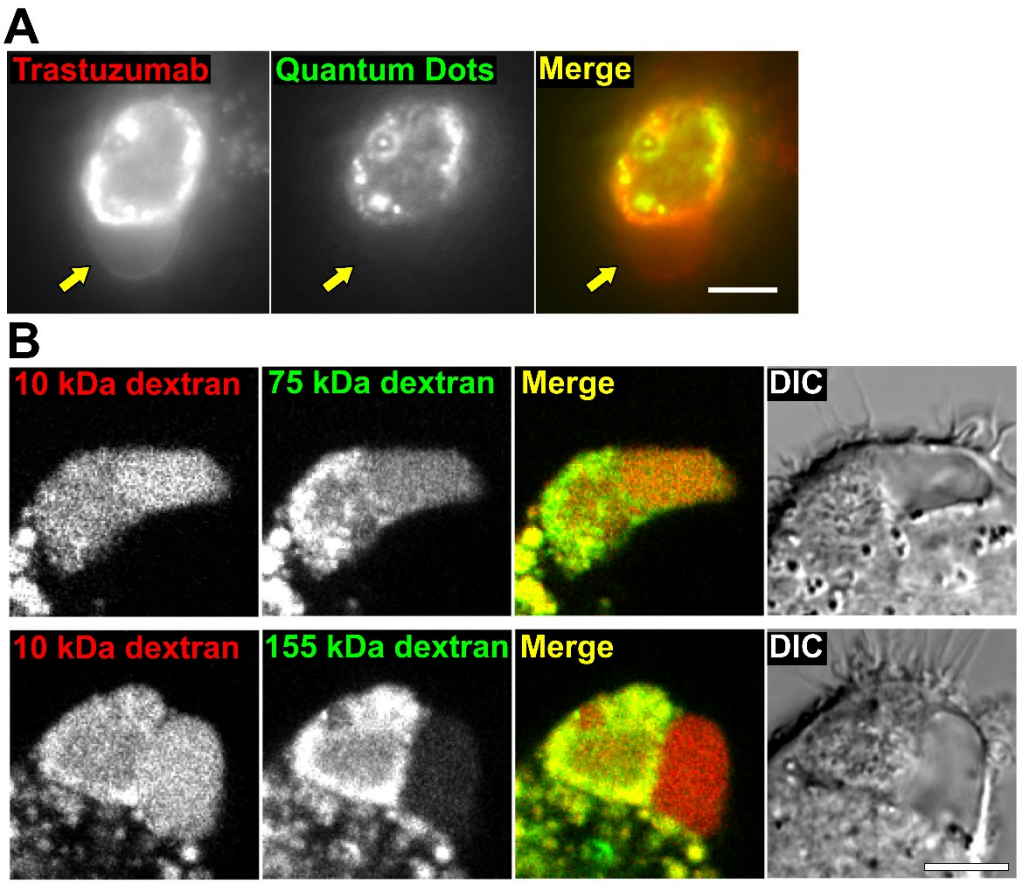

Figure 2.7 The vacuole is separated from the phagosome by a semi-permeable barrier
A, MDA-MB-453 cells were opsonized with Alexa 488-labeled trastuzumab (pseudocolored red) and counterstained with anti-human Fab-conjugated QDot 655 quantum dot nanoparticles (pseudocolored green). The cells were co-incubated with J774A.1 macrophages for 6 hours, followed by imaging (fluorescence). Yellow arrows indicate the location of the vacuole. B, MDA-MB-453 cells were opsonized with trastuzumab and co-incubated with J774A.1 macrophages for 6 hours followed by imaging (fluorescence and DIC). The macrophages were preloaded with Alexa 647-labeled 10 kDa dextran (pseudocolored red) and TRITC-labeled dextran of 75 or 155 kDa molecular weight (pseudocolored green) as indicated. Images of representative cells from at least 22 cells and 2 independent experiments are shown. Scale bars = 5 μm.

2.3.5. Formation of the phagosome-associated vacuole is independent of the effector or target cell-type

Using LysoTracker to differentiate the phagosome-associated vacuole from the phagosome, we investigated whether the phagosome-associated vacuole is observed for other macrophage:cancer cell couples. Target cells were co-incubated with bone marrow-derived macrophages and human monocyte-derived macrophages. Similar vacuole structures were associated with phagosomes for all macrophage types (Figure 2.8 A,B). The vacuole was also observed when trastuzumab-opsonized SK-BR-3 breast cancer cells or anti-CD20 (rituximab)-opsonized Raji B cells were used as targets, indicating that the formation of this structure is not dependent on the target cell type or the specificity of the opsonizing antibody (Figure 2.8 C).

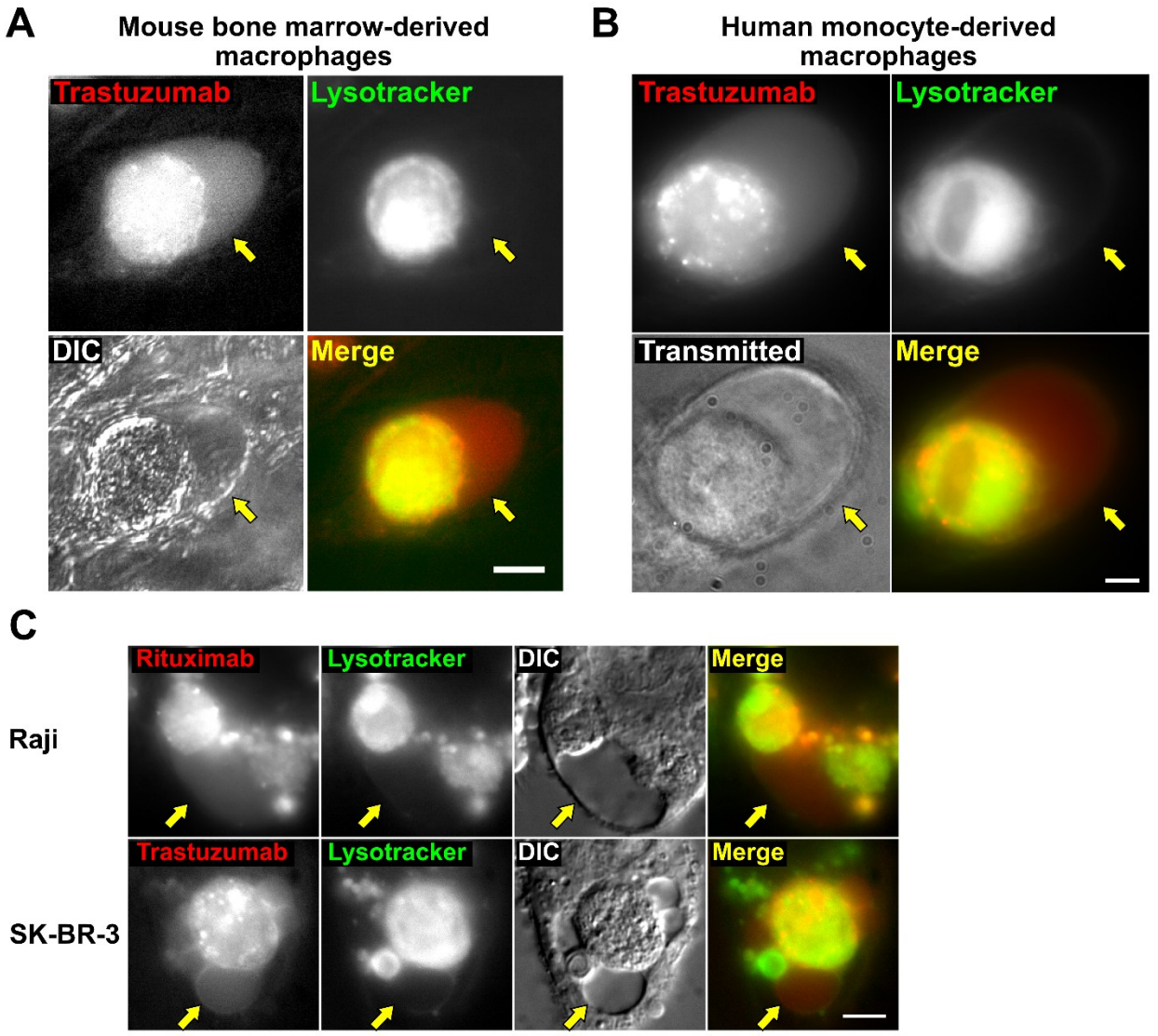

Figure 2.8 Phagosome-associated vacuoles are observed with multiple effector and target cell types

A, MDA-MB-453 cells opsonized with Alexa 488-labeled trastuzumab (pseudocolored red) were co-incubated with mouse bone marrow-derived macrophages for 6 hours, followed by addition of Lysotracker Red (pseudocolored green) and imaging (fluorescence and DIC). B, MDA-MB-453 cells opsonized with Alexa 647-labeled trastuzumab (pseudocolored red) were co-incubated with human monocyte-derived macrophages for 6 hours and treated/analyzed in for panel A. C, Raji B cells opsonized with Alexa 647-labeled rituximab or SK-BR-3 cells opsonized with Alexa 488-labeled trastuzumab (pseudocolored red) were co-incubated with J774A.1 macrophages for 4.5 hours or 6 hours, respectively, and treated/analyzed as in panel A. Yellow arrows in A-C indicate

the location of the vacuole. Images of representative cells from at least 34 cells and 2 independent experiments are shown. Scale bars = 5 μm.

2.3.6. The mTOR pathway regulates the size of phagosome-associated vacuoles

The mTOR pathway affects lysosomal biogenesis, with high levels of amino acids leading to the inhibition of transcription of genes associated with lysosome formation (*188*, *214*, *215*). In addition, mTOR inhibition has been shown to reduce fission of the entotic vacuole, a structure that is observed following engulfment of live (non-opsonized) cells by adjacent cells during carcinogenesis or development. We therefore investigated whether treatment with the mTOR inhibitor, torin 1, affected the size of the vacuoles. Phagosome-associated vacuoles were observed in the presence of torin 1 (Figure 2.9 A), and their size was greater in torin 1-treated cells relative to control cells (Figure 2.9 B). Fluorescence microscopy analyses also demonstrated that mTOR was present on the limiting LAMP-1+ membranes of the phagosome and associated vacuole for phagocytosed cancer cells (Figure 2.9 C), consistent with mTOR activation (*216*). By contrast, the levels of mTOR surrounding phagocytosed beads were substantially lower (Figure 2.9 C). In addition, the intracellular levels of phosphorylated S6 ribosomal protein (pS6), an indicator of mTOR activation, were analyzed in macrophages using an antibody specific for mouse/human pS6. Co-incubation of macrophages with antibody-opsonized tumor cells for 7 hours resulted in increased pS6 levels in macrophages compared with those in control samples or samples treated with torin 1 (Figure 2.9 D). Taken together, these data suggest that although mTOR signaling occurs during phagosome/vacuole maturation following phagocytosis of cancer cells, inhibition of

this pathway with torin 1 appears to affect phagosome/vacuole fission but does not prevent vacuole generation.

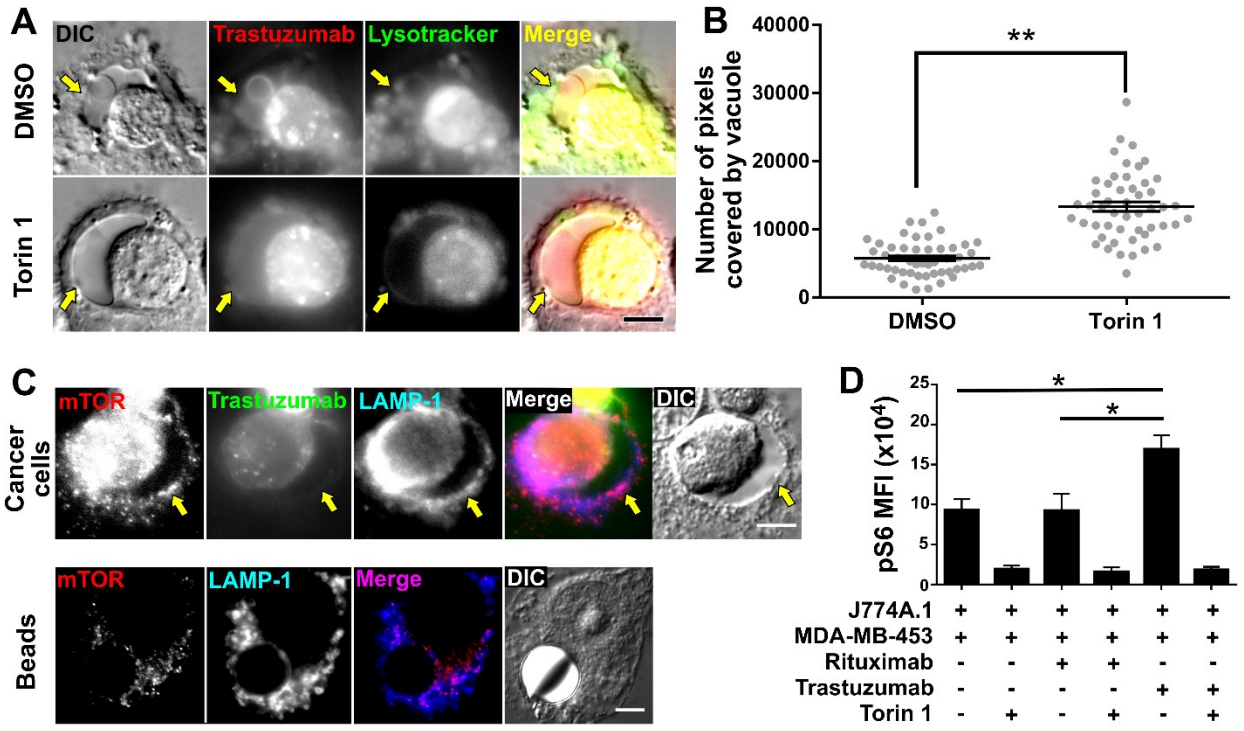

Figure 2.9 Inhibition of the mTOR pathway results in increased vacuole size
A, MDA-MB-453 cells opsonized with Alexa 488-labeled trastuzumab (pseudocolored red) were co-incubated with J774A.1 macrophages for 1 hour. The cells were then treated with 100 nM torin 1 or vehicle (DMSO) in the presence of 10 mg/ml IVIG and incubated for 6 hours. LysoTracker Red (pseudocolored green) was then added to the medium and cells were imaged. Fluorescent and DIC mages show representative vacuoles observed for each treatment condition. B, the size of the vacuoles was quantitated by manually segmenting the areas positive for trastuzumab and negative for LysoTracker Red surrounding each phagosome (n = 50 vacuoles) and counting the number of pixels covered by these segmentations. Error bars represent standard errors. The groups were compared using student's t-test, and ** indicates a statistically significant difference ($p < 0.01$). C, MDA-MB-453 cancer cells opsonized with Alexa 488-labeled trastuzumab (pseudocolored green) or streptavidin-coated beads (10 µm diameter) opsonized with biotinylated trastuzumab were co-incubated with J774A.1 macrophages for 1 hour followed by addition of 10 mg/ml IVIG and

incubation for a further 6 hours. Cells were fixed, permeabilized and incubated with LAMP-1- and mTOR-specific antibodies followed by Alexa 647- and Alexa 555-labeled secondary antibodies, respectively. Fluorescent and DIC images are shown. D, MDA-MB-453 cells treated with trastuzumab, rituximab (anti-CD20) or no antibody (as indicated) were co-incubated with J774A.1 macrophages for 1 hour. The cells were then treated with 100 nM torin 1 or vehicle (DMSO) in the presence of 10 mg/ml IVIG and incubated for 6 hours, fixed, permeabilized, and incubated with FITC-labeled mouse CD45-specific antibody and rabbit antibody specific for pS6 followed by Alexa 647-labeled anti-rabbit (H+L) antibody. Averages of mean fluorescence intensities (MFIs) are shown for triplicate or quadruplicate samples with error bars indicating SD. One-way ANOVA analyses was carried out followed by a Tukey's multiple comparisons test between all sample pairs with a confidence interval of 95%. Horizontal lines indicate the groups compared, and * indicates statistically significant differences ($p < 0.05$). Data shown are representative of two independent experiments. Yellow arrows in A and C indicate the location of the vacuole, and images of representative cells from at least 35 cells and 2 independent experiments are shown. Scale bars = 5 μm.

2.4. Discussion

In the current study, we describe a vacuolar structure that is formed during phagosomal maturation following macrophage-mediated phagocytosis of antibody-opsonized cancer cells. This vacuole is observed for three different macrophage:cancer cell combinations, suggesting that it is a universal structure associated with the phagocytic degradation of cellular targets. Although luminal space can be seen between the phagosomal 'body' and the limiting membrane of the phagosome in earlier electron micrographs, the space appears to be contiguous with the phagosome (*186*, *209*, *217*). By contrast, using EM and analyses of the differential accumulation of lysosomal tracers we demonstrate that the phagosome-associated vacuole described here is a discrete membrane-limited compartment (Figure 2.10).

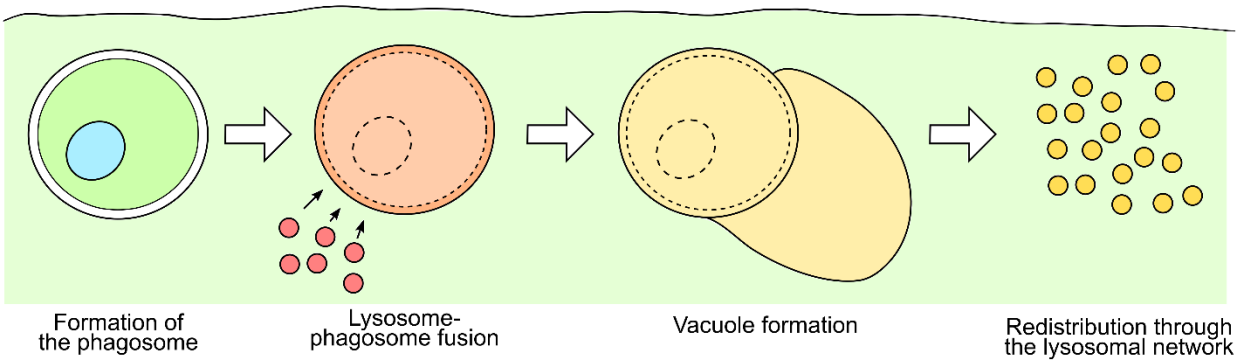

Figure 2.10 Schematic representation of the formation of the phagosome-associated vacuole
Following internalization of an antibody-opsonized cell, the lysosomes of the macrophage fuse with the phagosome. A distinct vacuole begins to form adjacent to the phagosome. Subsequently the phagosome and the vacuole shrink and their constituents are redistributed throughout the lysosomal network of the macrophage.

Interestingly, Lysosensor Blue (DND-192) but not LysoTracker Red can be detected in the vacuole when these dyes are added shortly before microscopy analyses. However, fluorescence from both of these dyes, which are membrane permeant and localize to acidic compartments, is lower in the vacuole compared with the adjacent phagosome (*218*). Two possibilities could explain this observation: first, the pH in the phagosome-associated vacuole may be higher than the pH in the phagosomal lumen. Our ratiometric analyses of the intensities of dextrans labeled with pH-sensitive and pH- insensitive fluors provide support for pH differences between the two compartments. Second, the entry of LysoTracker and LysoSensor into the vacuolar and phagosomal compartments may differ. For example, if the phagosome-associated vacuole is encapsulated by multiple membrane layers, acidic pH in the lumen between these membrane layers could result in accumulation of the acidotropic probes in this space and limit their diffusion into

the vacuole. This possibility is supported by the detection of LysoTracker fluorescence surrounding the vacuole. Nevertheless, the higher fluorescent signal for LysoSensor relative to LysoTracker is likely to be due to the pH sensitivity of fluorescence of this dye.

We show that dextrans of distinct sizes are selectively excluded from the phagosome-associated vacuole. Differential sorting of molecules in macrophages has been previously observed to occur between lysosomes (*211*) and between lysosomes and phagosomes (*212*, *219*). These studies led to the suggestion that such sorting might be caused by the diameter of the pores/tubules formed during potential kiss-and-run events that transfer solutes from one compartment to another (*220*). Our data indicates that similar interconnections may exist between the phagosome and the associated vacuole. This is further supported by the exclusion of quantum dot nanoparticles from the vacuole.

While the function of the phagosome-associated vacuole appears to be primarily related to the controlled release of metabolites, additional functions may exist for this compartment. Early studies have suggested that the size of the phagosome may correlate with the quantity of metabolites it releases, due to excess osmotic pressure. Similarly, the phagosome-associated vacuole could relieve such a buildup of osmotic pressure in a controlled manner. The differential accumulation of various solutes between the phagosome and the vacuole suggest that the vacuole may also act as a filter for the non-degradable or slowly degrading components of a large phagosome, separating and sequestering them from the degradable components. This possibility is supported by earlier reports suggesting that specialized lysosomal populations sequester such components (*122*, *221*).

Antigen presenting cells that are active in cross-presentation have been shown to maintain a higher pH in the antigen-loading compartments than cells that do not cross-present their antigen,

indicating that lower degradative rates are important for this process (*121*, *222*, *223*). Interestingly, our data are consistent with a higher pH in the vacuole compared with the phagosome, suggesting that this compartment could play a role in cross-presentation. Although macrophages are typically regarded to be inefficient in this process, cross-presentation of antigen from target cells following ADCP has been reported (*202*). Collectively, these observations suggest that the phagosome-associated vacuole may, therefore, be important for this pathway.

Analyses of mTOR and its downstream effector, pS6, demonstrate both mTOR association with the vacuole and increased pS6 levels in macrophages that contain antibody-opsonized tumor cells. This raises the question as to how the transcription factor, TFEB, which regulates the expression of a network of proteins involved in lysosomal biogenesis and function (*214*, *215*), retains sufficient activity to support lyso-some:phagosome formation, given that mTOR inhibits TFEB activation (*224*, *225*). Several recent studies demon-strate that mTOR-independent pathways such as those involving Ca^{2+}-mediated signaling and the Ca^{2+} channel, transient receptor potential mucolipin 1 (TRPML1, also known as MCOLN1), can play important roles in TFEB activation and lysosome:phagosome fusion (*192–194*). Thus, the observation that phago-some/vacuole formation occurs despite mTOR activation suggests that alternative pathways leading to the enhancement of TFEB and lysosomal activity can override the counteracting effects of mTOR activation (*193*, *194*, *226*).

In the current study, treatment of macrophage:cancer cell cultures with the mTOR inhibitor torin 1 does not inhibit vacuole formation, consistent with earlier studies demonstrating that torin 1 does not affect the formation of the entotic vacuole (*191*). Instead, incubation of macrophages containing antibody-opsonized cancer cells with torin 1 results in the generation of larger vacuoles. By analogy with the behavior of entotic vacuoles (*191*), this indicates that vacuole fission to reform

lysosomes is inhibited by mTOR blockade. Based on our current analyses, however, we cannot exclude the possibility that mTOR inhibition also contributes to increased lysosome:phagosome fusion due to elevated TFEB activation. In this context, the identification of an mTOR-independent pathway for entotic vacuole fission involving PtdIns(3)P 5-kinase (PIK)fyve, a lipid kinase and its downstream effector, the Ca^{2+} channel TRPML1, indicate that this cation channel can play dual roles in both the regulation of lysosomal activity and vacuole resolution (*192*, *193*, *195*). Nevertheless, the increase in vacuole size that we observe in the presence of torin 1 suggests that the PIKfyve pathway cannot fully compensate for the negative effect of mTOR inhibition on vacuole fission.

The phagosome-associated vacuole appears to be specific for cellular targets since it was not observed for antibody-opsonized beads. A primary factor that differentiates cancer cells from other phagocytic targets such as beads is their composition, including the presence of phospholipids and high concentrations (200 g/L(*227*)) of proteins. The role of phospholipid intermediates in endosomal/lysosomal trafficking pathways (*228*, *229*), combined with our data demonstrating that mTOR activation in response to released amino acids is not a prerequisite for vacuole generation, suggest that the presence of (phospho)lipids on the phagocytosed entity may be necessary for vacuole formation. It is also possible that the rigidity of the phagocytosed particle or cell affects vacuole development.

In summary, our study has identified a vacuole-like compartment that is associated with maturing phagosomes containing antibody-opsonized cells. Importantly, we demonstrate that this vacuole is separated by a semi-permeable membrane from the phagosome. Future studies will be directed towards defining the role of this vacuole in antigen presentation and other cellular processes related to phagocytosis.

3. 3D SINGLE MOLECULE TRACKING OF ANTI-FCRN ANTIBODIES WITH ITS CELLULAR CONTEXT USING AN ADVANCED IMAGING PLATFORM

3.1 Introduction

The neonatal Fc receptor (FcRn) plays an essential role in maintaining serum IgG levels throughout the body (*3*, *12*). IgG is internalized into cells by fluid-phase endocytosis, binds to FcRn in early endosomes in a pH-dependent manner, followed by the recycling/exocytic release of FcRn-bound IgG (Figure 3.1) (*5*, *40*, *41*). Consequently, FcRn salvages internalized IgGs from degradation and maintains IgG homeostasis. FcRn exhibits relatively high affinity binding to IgG at acidic, endosomal pH (pH~6.0), but binds very poorly at near neutral pH ~7 (*15*, *21*, *22*). This pH-dependence is important for the in vivo persistence of antibodies (*25*, *230*).

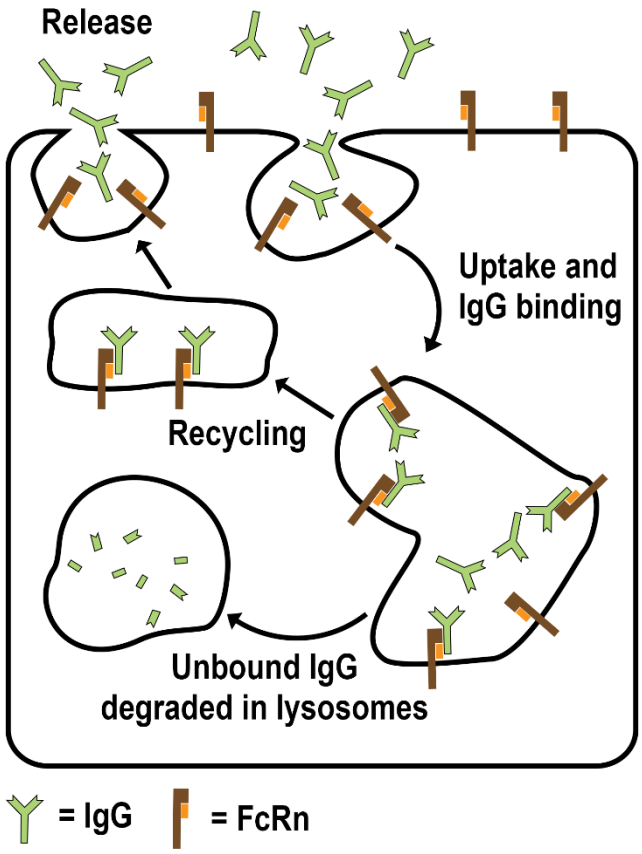

Figure 3.1: Model for FcRn mediated recycling of IgG

Multiple human autoimmune diseases, such as myasthenia gravis (MG) or immune thrombocytopenia purpura (ITP), are mediated by high levels of pathogenic IgGs. This indicates that approaches to reduce IgG levels could have therapeutic benefit (*231*). These IgG-mediated autoimmune diseases can be treated by B cell–depleting therapies or IVIg, but such treatments are expensive and often have undesirable side effects (*232*). In addition, B cell depleting antibodies such as rituximab that bind to CD20 do not deplete long-lived CD20-negative plasmablasts (*233*, *234*). Therefore, over recent years the

inhibition of FcRn has become an attractive therapeutic approach for autoimmune diseases (*49*, *55*, *58*, *66*). This approach has been accomplished by engineering antibodies to have a higher affinity for binding to FcRn than endogenous, wild type IgGs at both near neutral and acidic pH (*49*, *52*, *53*, *59*, *235*, *236*). Consequently, the engineered antibodies enter the cells by receptor-mediated uptake (through binding to FcRn at near neutral pH) and competitively inhibit endogenous IgGs from binding to FcRn (*49*). Consequently, unbound IgGs enter degradative lysosomes to lead to decreases in systemic levels of IgG (Figure 3.2)

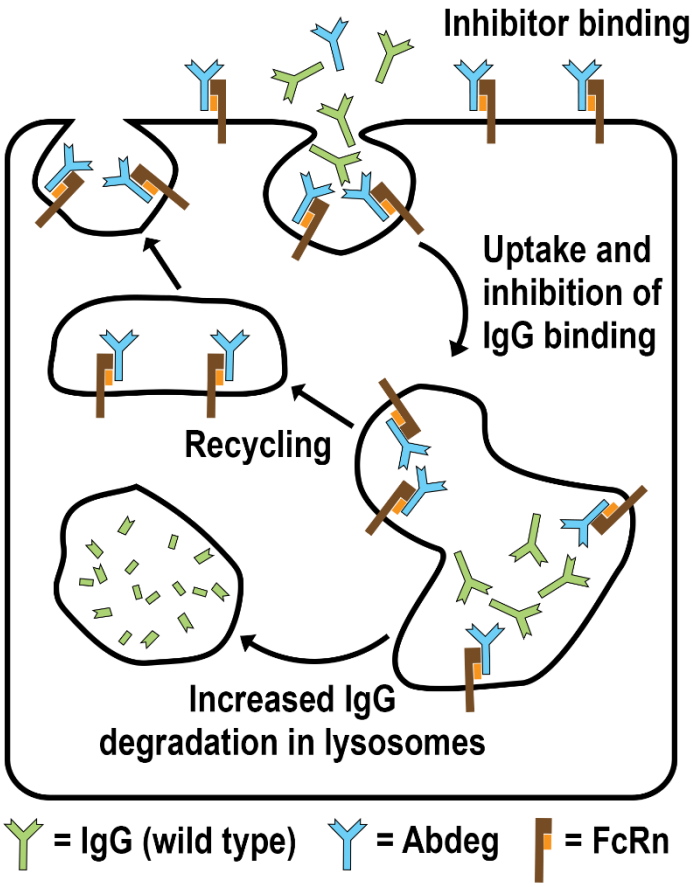

Figure 3.2: Engineering antibodies to inhibit FcRn

Several antibody-based FcRn inhibitors are currently in preclinical and clinical development (*50*, *53*, *54*, *61*, *62*, *237*). Although all of these antibodies reduce systemic IgG levels by inhibiting FcRn and blocking the salvage pathway (*49*, *238*), they differ in their molecular structure and binding properties (*49*, *52*, *53*, *236*, *239*). Efgartigimod (developed from the Abdeg technology) is an engineered Fc fragment that binds to FcRn through the natural interaction site of IgG for FcRn with pH-dependence (lower affinity at pH 7.4 vs. pH 6.0)(*49*), whereas other antibody-based FcRn inhibitors bind through the variable domains of the antibodies with very high affinity at near neutral and acidic pH (*239*). Studies of the cell biological behavior of an Fc-engineered antibody (Abdeg) with that of an antibody that binds through the variable domains (*59*) indicates differences in recycling rates and retention in FcRn-expressing cells (*50*). However, to date, details of trafficking behavior at the levels of behavior of single molecules in subcellular compartments such as endosomes have not been analyzed in detail due to the difficulties in simultaneously imaging both 3D single-molecule trajectories and their cellular context.

Therefore, in this study, using remote focusing multifocal plane microscopy (rMUM) previously described by our group (*173*), we have shown that this system can be used to analyze of the trafficking behavior of single molecules interacting with cellular structures or compartments that are also non-stationary (here sorting endosomes). Here we demonstrate that this system can be used to image the 3D subcellular trafficking of two FcRn inhibitors, MST-HN mutant ('Abdeg')(*49*) and Rozanolixizumab (UCB7665)(*53*), (described as Abdeg and UCB7665) using rMUM. UCB7665 binds to FcRn with high affinity across the pH range 6.0-7.4 through its V-regions (*53*). In these studies, FcRn

tagged with GFP is expressed in endothelial cells and is present in early/sorting endosomes and tubulovesicular transport carriers (TCs). Our results show that the rMUM technology allows the simultaneous imaging of single-molecules dynamics with small and non-stationary organelles such as sorting endosomes.

3.2 Sample preparation

3.2.1 Plasmid constructs

Human FcRn tagged at the C terminus of enhanced GFP (in pEGFP-N1; Clontech, Mountain View, CA; FcRn-GFP) and human β2- microglobulin (β2m) were expressed as described previously (*41*, *42*, *46*). Standard molecular biology methods were used to make the constructs and were sequenced before use in these studies.

3.2.2 Antibodies and reagents

Quantum dots (QDs) 705 coated with streptavidin, and 0.1 μm TetraSpeck™ microspheres were purchased from Invitrogen (Carlsbad, CA). Paraformaldehyde and glutaraldehyde used for the fixation of cells were purchased from Electron Microscopy Sciences (Hatfield, PA).

3.2.3 Cells and transfections

The human endothelial cell line HMEC-1, a generous gift by F. Candal at the Centers for Disease Control (Atlanta, GA) was maintained in MCDB 131 medium. Before transfection, the cells were maintained in phenol red-free Ham's F-12K medium supplemented with 10% FCS (HyClone) that had been depleted of immunoglobulin G (IgG) as described previously (*41*). Cells were transiently transfected with a combination

of expression plasmids encoding human FcRn-GFP (1.5 μg) and β2 microglobulin (0.75 μg) using Amaxa Nucleofector Technology.

3.2.4 Expression and site-specific biotinylation of FcRn-specific antibody and quantum dot labeling

We expressed two anti-FcRn antibodies, namely MST-HN mutant ('Abdeg') and UCB7665 (1519.g57 IgG4P). To express the MST-HN mutant (human IgG1-derived (*49*)) as an antibody with a site-specific biotinylation peptide at the C terminus, we adopted a previously described protocol (*40*). The recombinant protein was purified using lysozyme-Sepharose. We expressed anti-FcRn antibody UCB7665, as previously described (*238*). To express UCB7665 as an antibody with a site-specific biotinylation peptide at the C terminus, codon optimized gene fragments of humanized V-region heavy (VH) and light (kappa, VK) chain of UCB1519.g57 IgG4P were synthesized by Twist Bioscience and cloned into pcDNA3.4 expression vectors containing DNA encoding the human κ-chain constant, the human IgG1 heavy chain constant regions, and biotinylation signal peptide (Bsp) appended to the C-terminal of the CH3 domain, respectively. The plasmid constructs were transiently transfected with the Expi293 expression system kit (Life Technologies) into Expi293F cells and purified from culture supernatants using protein G-Sepharose (GE Healthcare) (*240*). To site-specifically biotinylate both the anti-FcRn antibodies, the proteins (~2 mg/ml) were individually dialyzed into 20 mM Tris-HCl, 50 mM NaCl, pH 8.0. Purified Abdegs were then incubated with BirA, ATP, magnesium and biotin (18 units per mg of antibody; Avidity, Denver, CO) for 16 h at room temperature (*241*). UCB7665 was incubated with BirA, ATP,

magnesium and biotin (Avidity, Denver, CO) according to manufacturers' recommendations at 4º C for 24 hours. The proteins were then dialyzed into PBS, pH 7.2. Biotinylation of the anti-FcRn antibodies was analyzed using ELISA by immobilizing them on Nunc Maxisorp plates, incubating with Streptavidin-HRP conjugate and developing with TMB substrate. The biotinylated antibodies were also analyzed to ensure that no detectable aggregates were present using HPLC (Superdex 200 or Yarra 3 µm SEC 3000).

For single-molecule live-cell imaging of the anti-FcRn antibodies, QD-antibody complexes were made. QD-anti-FcRn antibody (QD-αFcRn 1 and 2 are Abdeg and UCB7665, respectively) complexes were prepared by mixing the site specifically biotinylated anti-FcRn antibodies with streptavidin-coated QD705 at a 1:0.5 molar ratio of QD to an antibody (*42*). The mixture was incubated at room temperature for 10 minutes and then diluted with an imaging medium. The cells were incubated in an imaging medium (~pH 7.3) with QD conjugated anti-FcRn (11 nM with respect to antibody) at 37◦C with 5% CO2 and 95% humidity for 5 minutes, washed thoroughly with room temperature PBS (~pH 7.3), incubated with warm pH adjusted Ham's F-12K medium and imaged for about 10 minutes. Controls for non-specific antibody uptake by construct, non-specific accumulation of QD, and optical setup controls were also performed accordingly.

3.2.5 Live-cell imaging using rMUM

Live-cell imaging experiments were carried out using the rMUM setup. To keep the cell alive during live-cell single molecule imaging experiment, we installed a microscope incubation system (Okolab; Pozzuoli NA, Italy) to maintain the temperature at 37˚C with

5% CO2 and 95% humidity. Before performing the live-cell imaging experiments, a calibration data set was acquired using Nanogrid calibration slide (Miraloma Tech, LLC). The acquired calibration data is used to determine essential information to analyze the live-cell imaging data, such as spatial transformation matrices, conversion factor α for the focal shift correction, and experimental PSF data for MUMLA. The live-cell samples for the anti-FcRn antibody (Abdeg or UCB7665) were then prepared as previously described. The cells were washed twice with a warm (37◦C) imaging medium and subsequently placed on the objective lens and left undisturbed for a few minutes to attain thermal stability before imaging.

3.3 Results

3.3.1 Acquisition settings in rMUM setup

The remote focusing multifocal plane microscopy (rMUM) setup comprises of an excitation module, a standard microscope, and two emission modules: a multifocal plane microscopy module (MUM-module) and a remote focusing microscopy module (r-module). The MUM-module images trajectories of single molecules in 3D, and the r-module performs 3D volumetric imaging of the cellular context. Volumetric contextual imaging is achieved by sequentially scanning the specimen along the optical axis without having to move the specimen physically. A commercially-available standard NanoGrid slide (Miraloma Tech, LLC) is used to acquire calibration data which is used to perform 2D and 3D spatial registration and estimation. We configured the MUM-module with four distinct focal planes, and the adjacent planes are separated by a spacing of 1.21 µm, 1.24 µm, and 1.27 µm. The MUM-module was set to acquire 25 images for every 51 R-images,

which constitutes one full R-volume (i.e., a z-stack). In other words, the acquisition rate of the MUM-module is ten frames per second for four focal planes simultaneously acquired. We configured the r-module to obtain z-stacks at a 300 nm step size with 51 frames per stack, covering a depth of ~15 μm inside the cell. The acquisition rate of the r-module was set to 20 frames per second, i.e., one entire volume (a z-stack) was acquired in about 2.5 seconds. To maximize the speed of axial scanning, we use a bi-directional scanning mode (Figure 3.3) in which the r-piezo nanopositioner first moves in one direction for the acquisition of z-stack images and then moves back to the original position in the opposite direction for the acquisition of the next z-stack images (Figure 3.3). The live-cell samples were imaged using the same acquisition settings and configurations used to acquire the calibration data set.

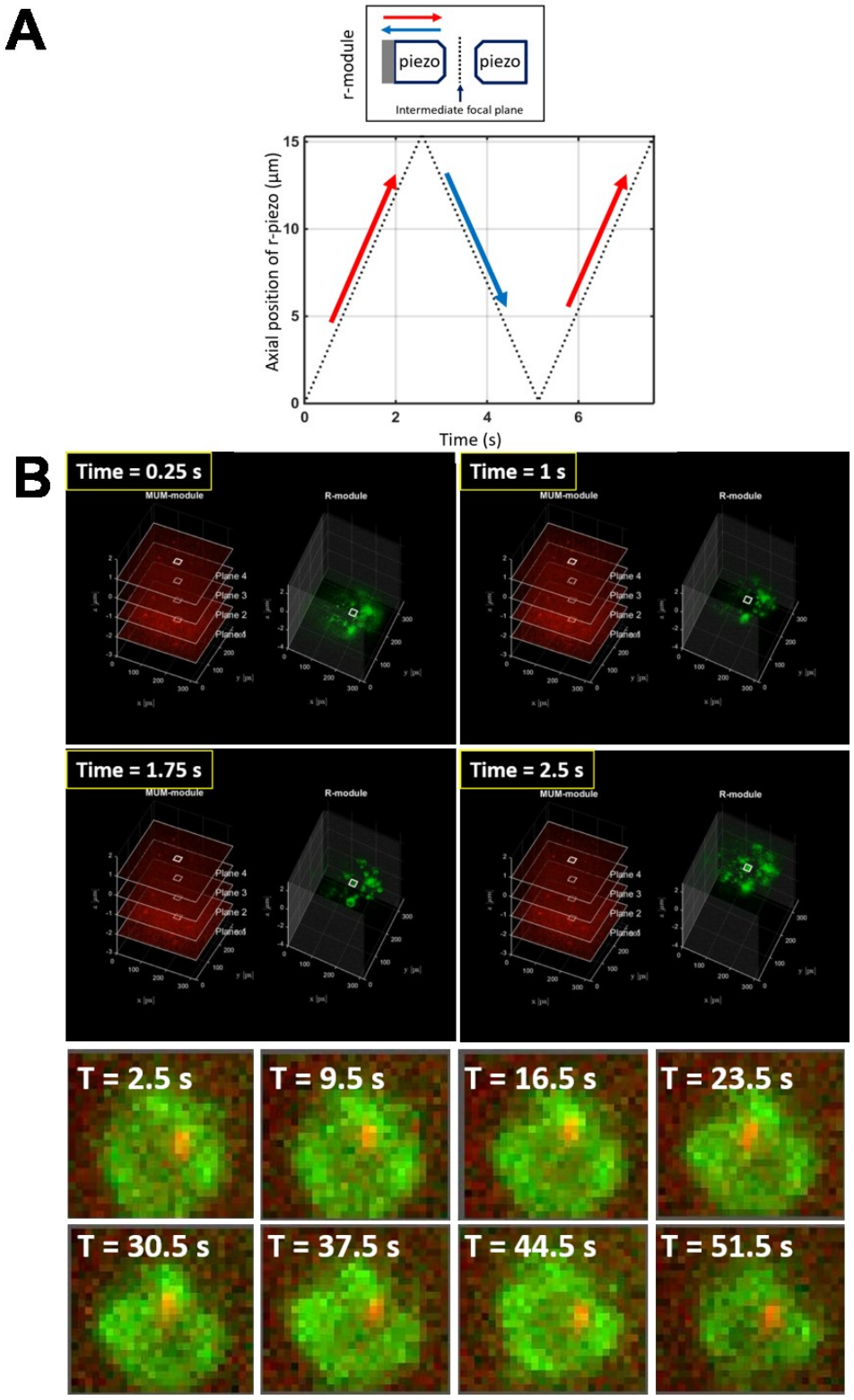
A
r-module
piezo
piezo
Intermediate focal plane
Axial position of r-piezo (µm)
Time (s)
B
Time = 0.25 s
Time = 1 s
Time = 1.75 s
Time = 2.5 s
MUM-module
R-module
Plane 4
Plane 3
Plane 2
Plane1
T = 2.5 s
T = 9.5 s
T = 16.5 s
T = 23.5 s
T = 30.5 s
T = 37.5 s
T = 44.5 s
T = 51.5 s

Figure 3.3 Acquisition settings in rMUM setup
A, Bi-directional mode of r-module B, Time-lapse images of the sample (QD-UCB7665 and hFcRn-GFP pseudocolored as red and green, respectively) using rMUM. The bottom panel shows the time-lapse overlay images (maximum z-projection) of the selected ROI.

3.3.2 Data analysis and processing

We perform live-cell imaging of hFcRn transfected HMEC-1 cells, as described in the methods section. The rMUM data is collected using two imaging modules, r- and MUM-module, operating at different acquisition rates and coordinate systems. As described in the methods, the acquisition rate of the r-module is twice as fast as the rate of the MUM-module. Therefore, the acquired rMUM data must first be registered both spatially and temporally to mine and analyze the rMUM data. To spatially transform different sets of data into one reference coordinate system (i.e., camera 1 in the MUM-module), we applied the corresponding spatial transformation matrices generated using the calibration data to the imaging data (Figure 3.4). To temporally register data between the r- and MUM-module, the data acquired in the r-module was temporally interpolated to match the time points of the single-molecule data obtained in the MUM-module.

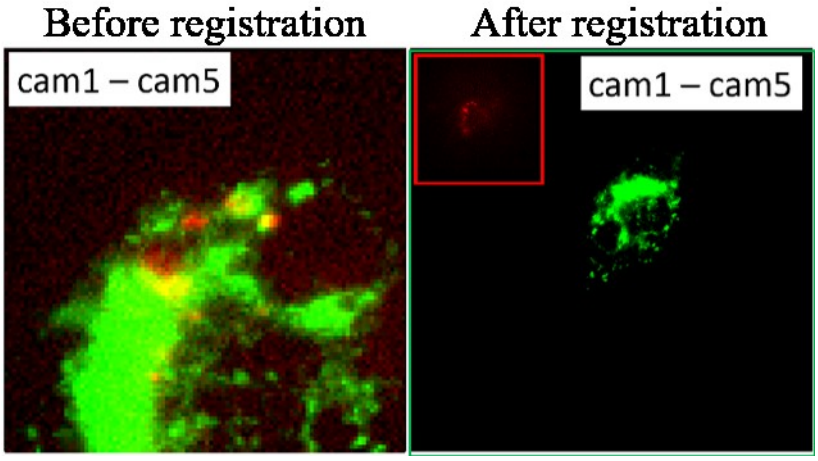

Figure 3.4 Spatial transformation of rMUM images
HMEC-1 cells expressing hFcRn-GFP were pulsed with QD 705 conjugated antibody (Abdeg or UCB7665) for 5 minutes, washed twice with room temperature PBS, and imaged live using the rMUM setup. GFP and QD 705 are pseudocolored green and red, respectively. Overlay of rMUM image before and after image registration is shown. Here cam 1 represents plane 1 of the MUM-module, and cam 5 denotes the z-stack acquired using r-module.

Once the rMUM data is processed, the data is visualized using visualization software to gain additional insights to interpret the data further. Therefore, we visualized the processed rMUM data with Lumio (Astero Technologies LLC), a software application designed to view and process complex and large sets of imaging data such as our rMUM data. To find interesting biological events (a step called datamining), displaying the data as a montage for each corresponding focal plane image between MUM- and r-images (Figure 3.5) is convenient. The identification and segmentation of single molecules and the associated endosomes were performed manually using the segmentation tool in Lumio.

For the molecule of interest, the region of interest (ROI) was defined using the display interface of Lumio, and the coordinates of the imaged molecule in the ROI were determined using the MUMLA algorithm, as described previously (*173*).

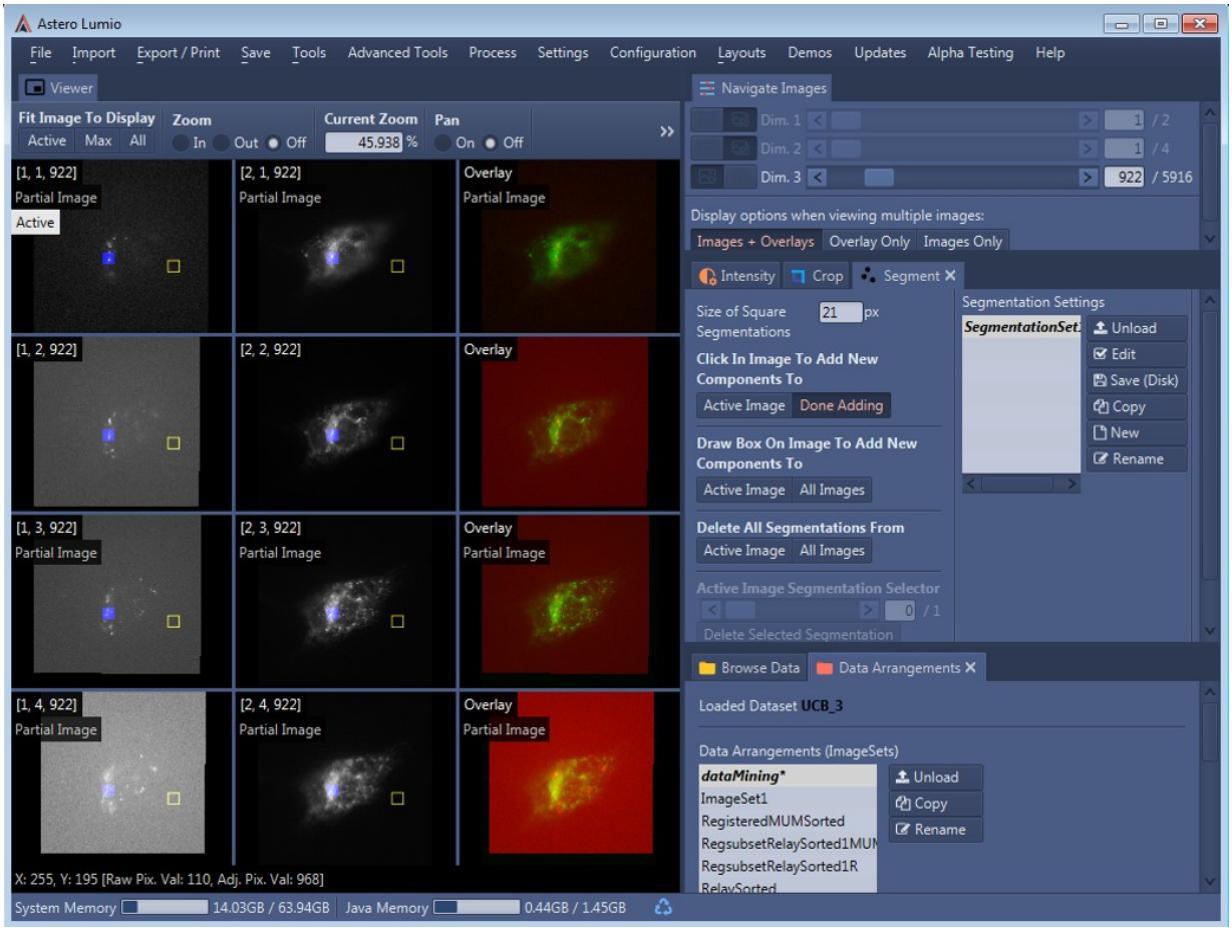

Figure 3.5 A snapshot of rMUM data as seen using the image processing software

3.3.3 3D visualization of single-molecule trajectory with the cellular context

Three-dimensional visualization of a single molecule of interest along with the cellular context at any time point along the trajectory can provide intuitive insights into understanding subcellular trafficking. Visualizing detailed structural dynamics of the

cellular context and the corresponding trajectory of a single molecule warrants a volume rendering of the same in 3D. The series of z-stacks acquired using the r-module are preprocessed by deconvolution (Section 3.3.3.1, Figure 3.6) and temporal interpolation (Section 3.3.3.2), sequentially. The main visualization approach is through isosurfaces as obtained using the MATLAB isosurface command. We also use 3D voxel-based approach to render the volumetric data. The code used for the volume rendering is from Oliver Woodford's Matlab code (*242*). This code uses the orthogonal plane 2D texture mapping technique for volume rending 3D data in OpenGL. The trajectory of a single molecule of interest is then reconstructed with pseudo-colors corresponding to the time point and superimposed on the isosurface-rendered images at every time point.

3.3.3.1 3D deconvolution

The optical properties of a microscope, especially a widefield fluorescence microscope, can lead to significant out-of-focus blurring of the acquired images. To obtain higher quality 3D rendered images from the r-module, we, therefore, use the deconvolution approach, which can effectively reduce the influence of out-of-focus excitation noise. We use a computational approach, the iterative Richardson-Lucy deconvolution algorithm (*243*), to remove the blurring of the z-stack images acquired using the r-module.

Firstly, a set of z-stack images are simulated using the Born and Wolf PSF model (*244*) with the experimental parameters of the microscope system. The parameters used are the numerical aperture of the objective lens, the wavelength of the detected photons, and the refractive index of the immersion oil. The data acquired using the r-module are

then deblurred by the deconvolution process using the simulated PSF z-stack, over an appropriately chosen number of iterations.

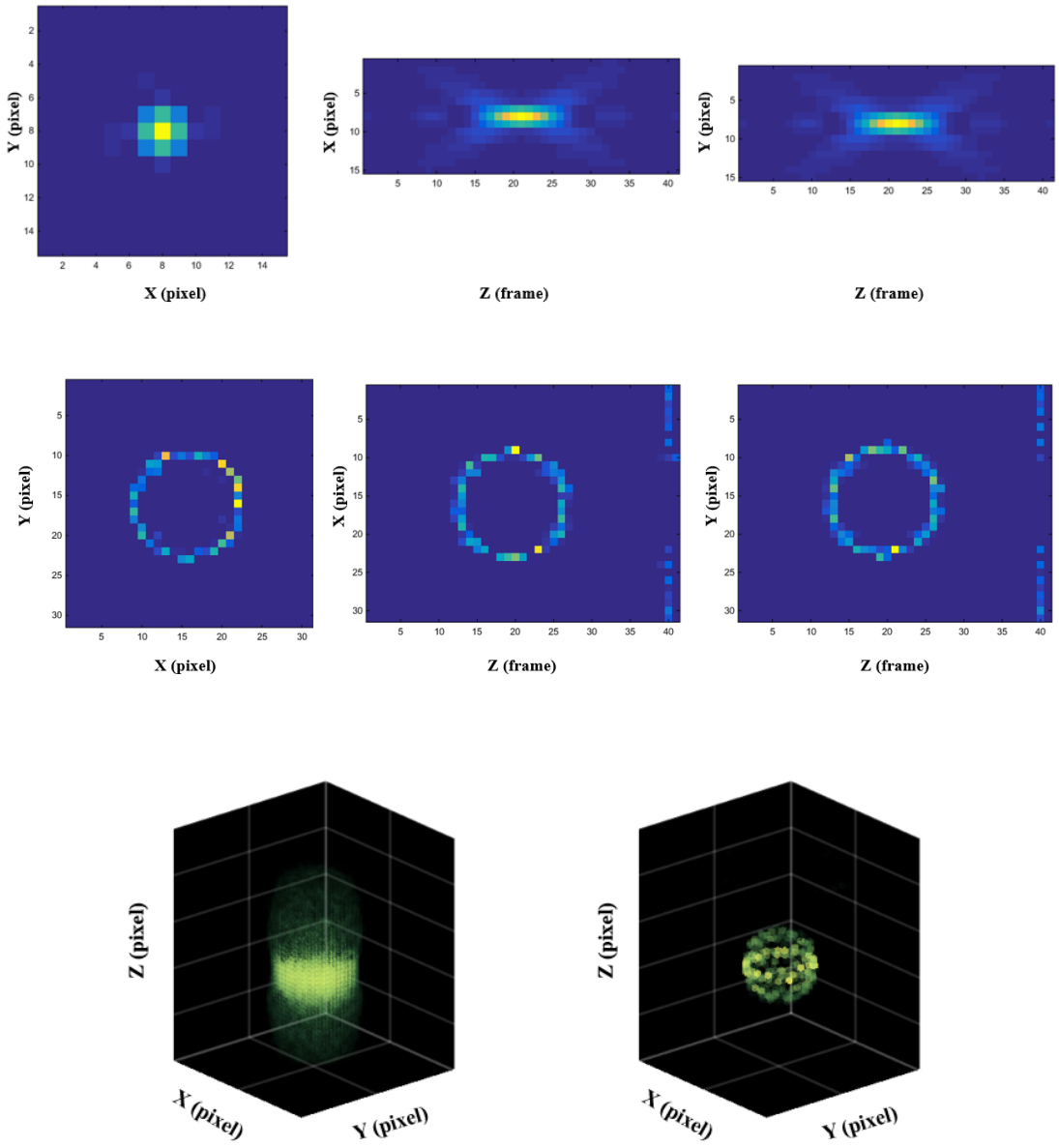

Figure 3.6 The simulated sphere data after deconvolution
The top panel shows the projection images of simulated PSF used for the deconvolution. The middle panel shows the projection images of sphere data after deconvolution. The

bottom panel shows the 3D visualization of the simulated sphere before (left) and after deconvolution (right).

3.3.3.2 Temporal interpolation

Unlike the MUM-module, the r-module needs to scan the volume of interest along the optical axis sequentially. Therefore, the acquisition rate per volume of the r-module is slower than the rate of the MUM module. A temporal interpolation approach using B-splines (*245*) is adopted to render the cellular context completely (Figure 3.7). This provides the interpolated images of r-module corresponding to the time point in a single molecule trajectory. To elaborate, for each z focus level, the r-module images at the same time point as the MUM-module image is generated by interpolating the pixel values of images acquired at different times with a specific choice of the B-spline degree d.

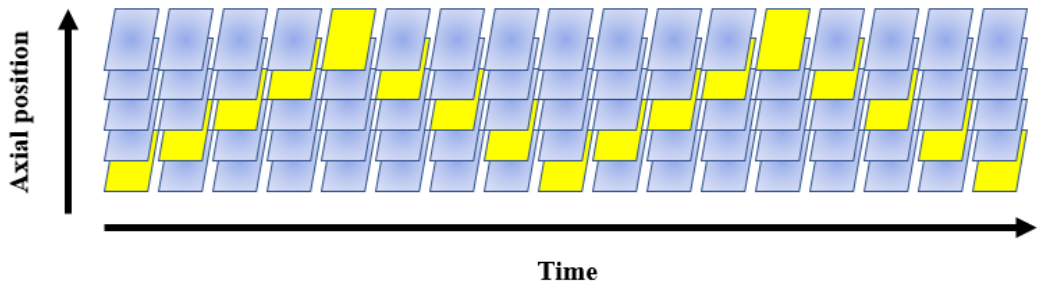

Figure 3.7 Illustration of the time interpolation using the z-stack images from the r-module (bi-directional mode)
The yellow rectangles represent the images acquired by the r-module, and the blue rectangles represent the images that need to be interpolated.

To visualize the r-data with improved resolution, we subsequently deconvolved the temporally registered r-module data using the Richardson-Lucy algorithm (detailed above in Section 3.3.3.1) and see an improved z-stack images (Figure 3.8).

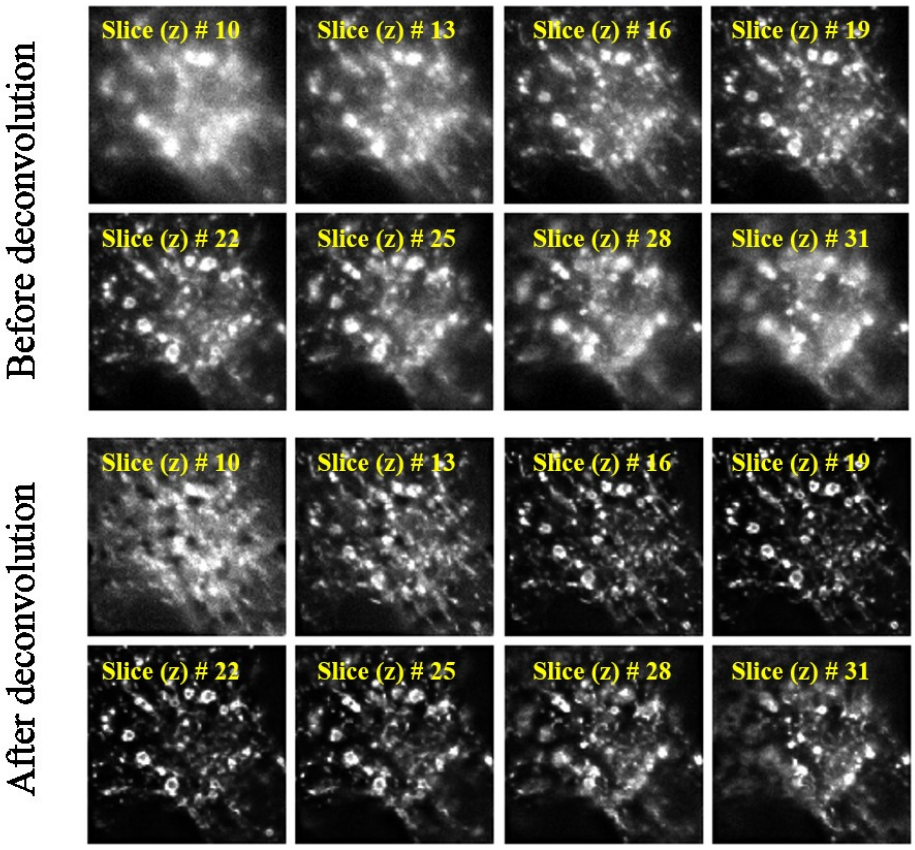

Figure 3.8 Deconvolvution of z-stack images acquired using rMUM setup
HMEC-1 cells expressing hFcRn-GFP were pulsed with QD 705 conjugated antibody for 5 minutes, washed twice with room temperature PBS, and imaged live using the rMUM setup. Z-stack images acquired using r-module are deconvolved as described in Section 3.3.3.1. Z-stack images before and after deconvolution are shown here.

3.3.4 3D behavior of QD conjugated Abdeg in a sorting endosome

The two anti-FcRn antibodies conjugated to QD705 were imaged using the rMUM setup, and the data was processed as described above. HMEC-1 cells expressing hFcRn-GFP were pulsed with QD 705 conjugated Abdeg for 5 minutes, washed and imaged live using the rMUM setup. Panel A of Figure 3.9 shows a maximum intensity projection of a cell. Maximum-intensity projected images are used for preliminary data mining to find suitable cells and areas of interest. Here we see a QD-Abdeg molecule localized on the ring-like sorting endosome. One small ROI is then enlarged and visualized as a montage in panel B. Each row in the montage corresponds to images acquired at each MUM focal plane and its corresponding (approximate) z-stack plane acquired using the r-module. Visualizing the data in this fashion provides more insight into the event of interest. At t=2.8 s, the QD-Abdeg molecule, which is found interacting with the sorting endosome in Plane 1, moves up to Plane 2 at t=47.2 s, which is 1.2 μm apart from the reference plane. This shows that the sorting endosomes are also non-stationary and move inside the cell.

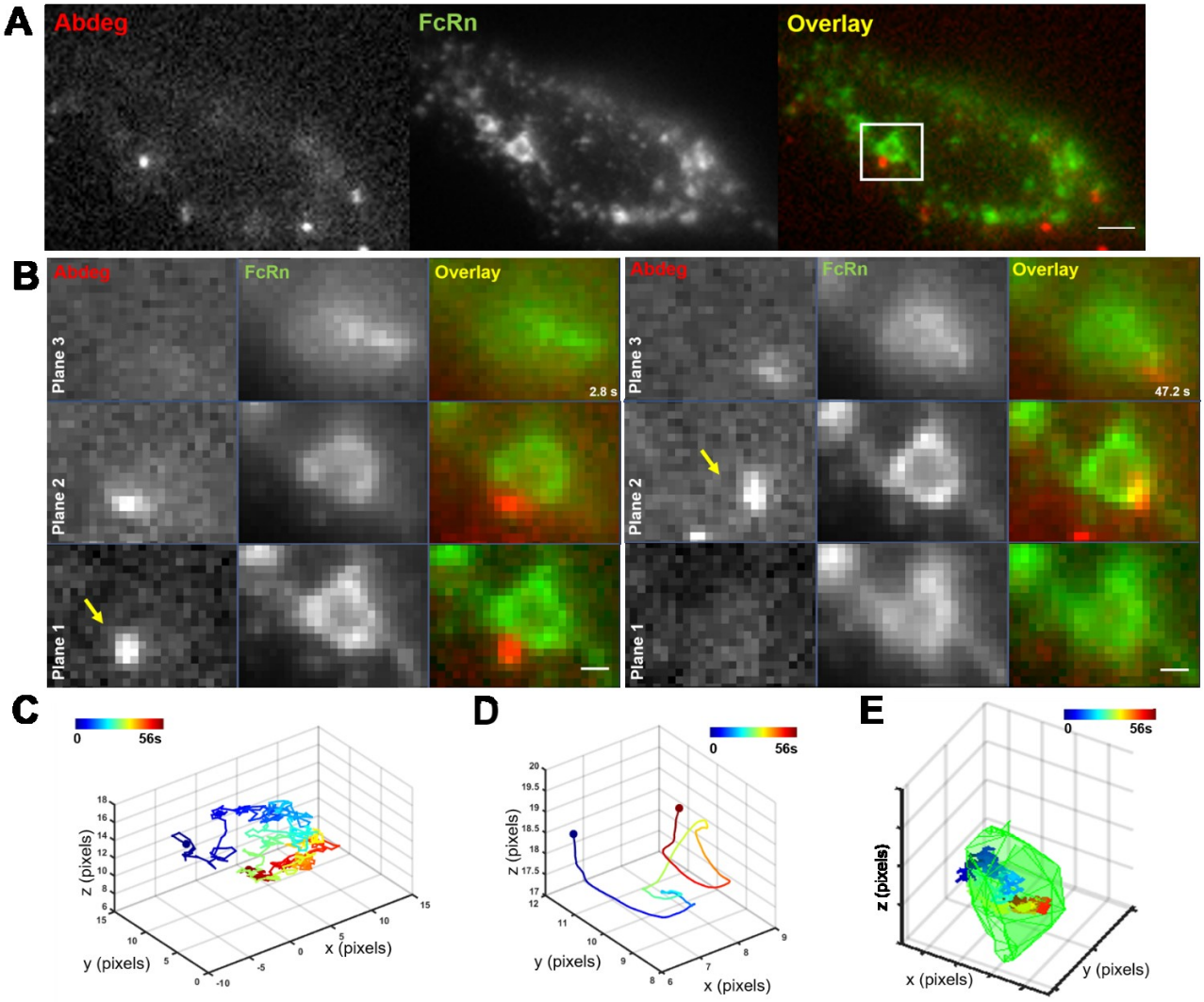

Figure 3.9 3D behavior of QD conjugated Abdeg in a sorting endosome

HMEC-1 cells expressing hFcRn-GFP were pulsed with QD 705 conjugated Abdeg for 5 minutes, washed twice with room temperature PBS, and imaged live using the rMUM setup. A, A snapshot of maximum-intensity projected image of a representative hFcRn-transfected HMEC-1 cell. The white box represents the region in the cell that is shown in the montages. GFP and QD 705 are pseudocolored green and red, respectively. Scale bars: 3 µm. B, Montages for FcRn and Abdeg channels along with the overlay displaying areas of interest of a transfected HMEC-1 cell with the time (in seconds) at which each image was acquired. Each row in the montage corresponds to images acquired at each MUM

focal plane and its corresponding (approximate) z-stack plane acquired using the r-module. Plane 2 and plane 3 are 1.2 µm and 2.4 µm away from Plane 1, respectively. Individual frames at t= 2.8 s (left panel) and t= 47.2 s (right panel) are shown as examples. Yellow arrow indicates the QD-Abdeg molecule that is tracked, and it moves from plane 1 (left panel) to plane 2 (right panel). Scale bars: 1 µm C, 3D trajectory of the QD-Abdeg molecule as acquired by MUM-module. D, 3D trajectory of the sorting endosome as acquired by r-module. E, 3D visualization of the QD-Abdeg molecule (color-coded track) and the interacting sorting endosome (green) for t=56 s. The trajectory showed here is compensated for the sorting endosome's motion, thus giving the actual motion of the QD-Abdeg complex. The trajectory shown in panels C, D, and E is color-coded to indicate time. The color change from blue to green to red indicates increasing time.

The estimated 3D single molecule trajectory of QD-Abdeg and the interacting endosomal trajectory is shown individually in panels C and D, respectively. We then compensate the single molecule trajectory for the sorting endosomes' motion and estimate a true 3D trajectory (Figure 3.9, Figure 3.10). 3D rendering of the z-stacks of sorting endosomes acquired using the r-module is visualized together with the compensated QD-Abdeg trajectory in panel E. The final visualization shows that the QD-Abdeg molecule interacts with the sorting endosome membrane and appears to co-localize with the ring-like structure.

3.3.4.1 Endosome localization and approximation

Molecular dynamic studies of individual molecules and their interactions with subcellular organelles, such as early endosomes, late endosomes, and lysosomes, are of significant biological interest in understanding the subcellular trafficking pathway (*2*,

246–249). To obtain detailed information of the individual proteins within the sorting endosomes, the 3D positions of the single-molecule needs to be estimated with high accuracy and subtracted from the 3D centroid of the sorting endosomes that the molecule interacts with, in each frame of the recorded time sequence of images.

The 3D centroid of a sorting endosome is estimated as follows. We first generate maximum intensity projection (MIP) images of the endosome images (i.e., a z-stack) from three angles: from the top (z-projection) and two sides (x- and y-projection). The center of mass of each projection image is then calculated, i.e., x and y coordinates from the z-projection image, y and z coordinates from the x-projection image, x and z coordinates from the y-projection image. The final x, y, and z positions of the endosome are determined by averaging the measures of each axis.

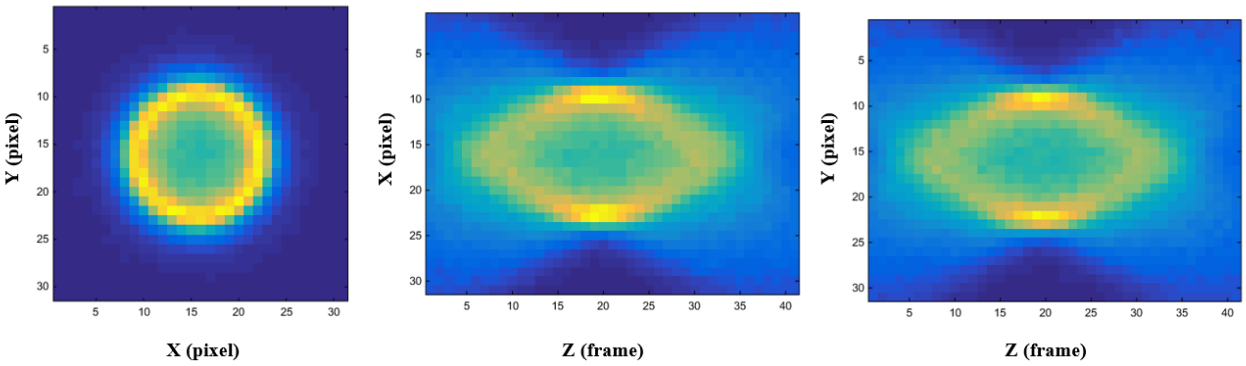

Figure 3.10 xy-, xz-, and yz-projection of the simulated sphere data

Most of the sorting endosomes are approximately spherical, and the diameter of the endosomes is about 100–500 nm (*250*). To verify the endosome localization approach, we

first simulated z-stack images of the sphere with a diameter of 140 nm (*251*), as shown in figure above. The pixel size of the simulated images is 100 nm × 100 nm, and the z-stack range is 2000 nm to -2000 nm with a step size of 100 nm, the center of the simulated sphere (x, y, z) is (16, 15.6, 19.5) μm. The estimated x, y, and z using our approach is (16.0828, 15.6836, 19.5706) μm, which has an error less than 10 nm. We require both spatial and structural information (such as radii) of the endosomes in order to compensate the single molecule trajectory. Here, the radius of a sorting endosome (i.e., a sphere) is determined by applying Hough transform (using the MATLAB function "imfindcircles") to xy-maximum intensity projections of the 3D z-stack of the endosome. Applying this approach to the simulated data above, the estimated diameter of the sphere is 135 nm. By using this approach to the experimental data, we find in average the diameter of the endosomes were 0.3-1.2 μm.

3.3.5 3D behavior of QD conjugated UCB7665 in a sorting endosome

We analyzed the 3D behavior of QD conjugated UCB7665 interacting with sorting endosomes. HMEC-1 cells expressing hFcRn-GFP were pulsed with QD 705 conjugated UCB7665 for 5 minutes, washed and imaged live using the rMUM setup. Panel A of Figure 3.11 shows a maximum intensity projection of a cell. Maximum-intensity projected images are used for preliminary data mining to find suitable cells and areas of interest. Here we see a QD-UCB7665 molecule localized on the ring-like sorting endosome. One small ROI is then enlarged and visualized as a montage in panel B. Similar to Figure 3.9, each row in the montage corresponds to images acquired at each MUM focal plane and its corresponding (approximate) z-stack plane acquired using the r-module.

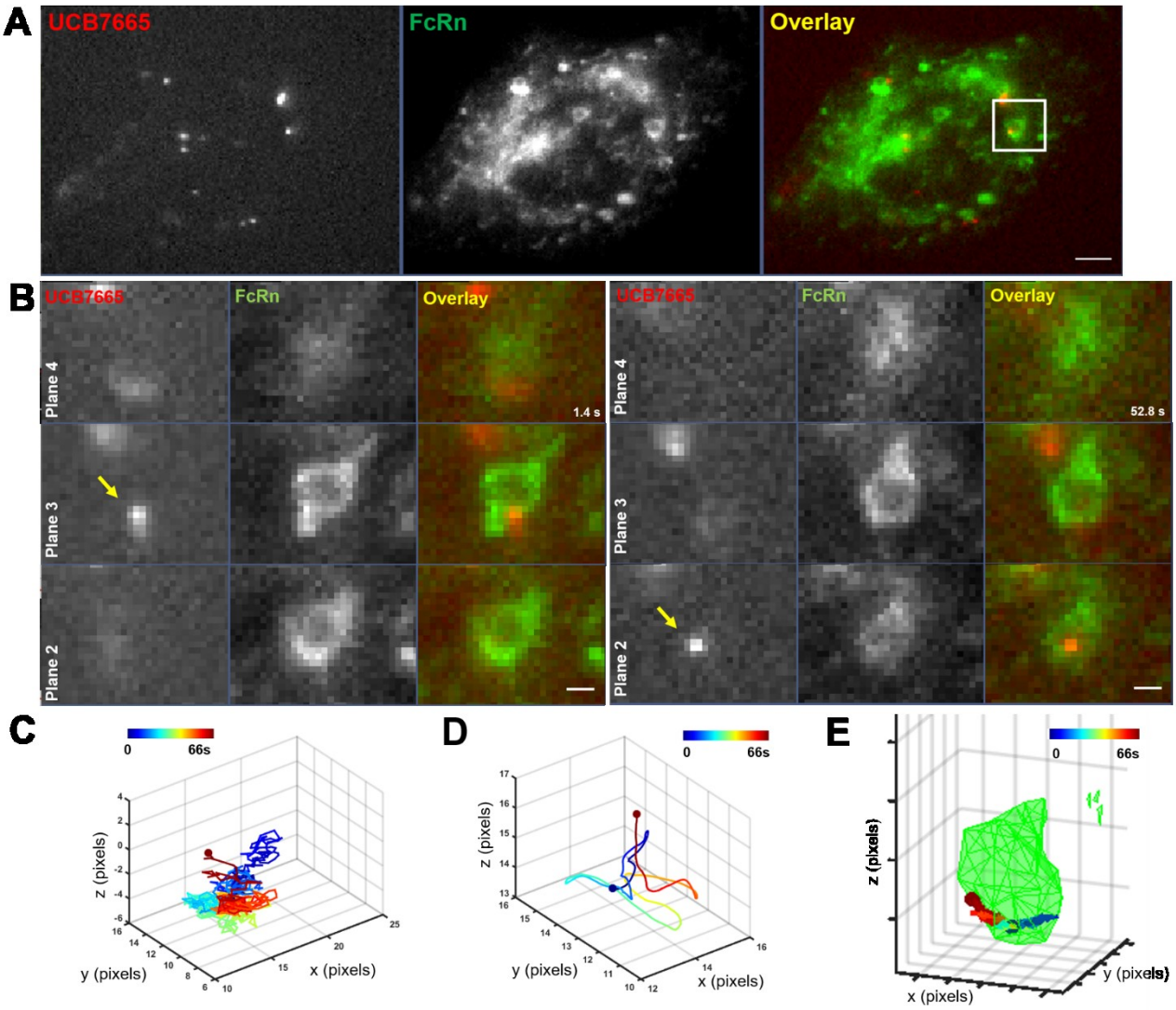

Figure 3.11 3D behavior of QD conjugated UCB7665 in a sorting endosome
HMEC-1 cells expressing hFcRn-GFP were pulsed with QD 705 conjugated UCB7665 for 5 minutes, washed twice with room temperature PBS, and imaged live using the rMUM setup. A, A snapshot of maximum-intensity projected image of a representative hFcRn-transfected HMEC-1 cell. The white box represents the region in the cell that is shown in the montages. GFP and QD 705 are pseudocolored green and red, respectively. Scale bars: 3 µm. B, Montages for FcRn and UCB7665 channels along with the overlay displaying areas of interest of a transfected HMEC-1 cell with the time (in seconds) at which each image was acquired. Each row in the montage corresponds to images acquired at each MUM focal plane and its corresponding (approximate) z-stack plane acquired using the r-

module. Plane 2, plane 3, and plane 4 are 1.2 μm, 2.4 μm, and 3.6 μm away from Plane 1, respectively. Individual frames at t= 1.4 s (left panel) and t= 52.8 s (right panel) are shown as examples. Yellow arrow indicates the QD- UCB7665 molecule that is tracked, and it moves from plane 3 (left panel) to plane 2 (right panel). Scale bars: 1 μm C, 3D trajectory of the QD- UCB7665 molecule as acquired by MUM-module. D, 3D trajectory of the sorting endosome as acquired by r-module. E, 3D visualization of the QD- UCB7665 molecule (color-coded track) and the interacting sorting endosome (green) for t=66 s. The trajectory showed here is compensated for the sorting endosome's motion, thus giving the actual motion of the QD- UCB7665 complex. The trajectory shown in panels C, D, and E is color-coded to indicate time. The color change from blue to green to red indicates increasing time.

At t=1.4 s, the QD-UCB7665 molecule, which is found interacting with the sorting endosome in Plane 3, moves down to Plane 2 at t=52.8 s (from 3.4 μm to 1.2 μm). The structure of the sorting endosome also changes and is non-stationary. The estimated 3D single molecule trajectory of QD-UCB7665 and the interacting endosomal trajectory is shown individually in panels C and D, respectively. We then compensate the single molecule trajectory for the sorting endosomes' motion and estimate a true 3D trajectory similar to Figure 3.9. 3D rendering of the z-stacks of sorting endosomes acquired using r-module is visualized along with the compensated QD-UCB7665 trajectory in panel E. The final visualization shows that the QD-UCB7665 molecule interacts with the sorting endosome membrane and appears to co-localize with the ring-like structure.

It should be pointed out that in Figure 3.9 and Figure 3.11, we observed blinking of the QD throughout its trajectory. To reliably track QDs and the blinking behavior to not

interfere with the tracking, QDs that were sufficiently isolated were used for estimation. Hence they were unambiguously and reliably identified when they reappeared in the image.

3.4 Discussion

The rMUM technology is a novel advanced imaging technique offering an aberration-free imaging platform for 3D imaging of single molecule together with its cellular context. The r-module is modular and can be implemented in combination with a standard commercial microscope. This technique is superior compared to other classical sectioning approaches because the biological sample is not moved. Even though light sheet microscopy is used for imaging much deeper into the biological samples, the rMUM system facilitates imaging the 3D trajectories in combination with the cellular context. Recent advances in 3D single molecule imaging include tracking of single molecules in 3D combined with two-photon scanning or light sheet microscopy (*252–255*). Simultaneous tracking and contextual imaging has been studied by several groups (*256*, *257*). In particular, a recent study shows simultaneous motion and pH-sensing of nanoparticles in its targeted lysosomes (*257*). However, they fail to capture real-time images of the cellular context continuously. A study by Welsher and colleagues also described 3D tracking of internalizing viral particle and contextual imaging of the intracellular organelles asynchronously (*256*). By this method, the interacting compartments can be identified, however, they cannot be imaged continuously together with the single molecule.

The ability to track single molecules and their cellular contexts synchronously, is highly preferred in trafficking studies where the processes involved frequently occur rapidly. By adopting the rMUM imaging platform to image fast dynamic processes, 3D tracks of the single molecules in combination with their cellular context can be obtained after compensating for the organelle motion. We have designed an advanced imaging system to study the single molecule behavior of engineered antibodies together with their global cellular context. Our study focused on obtaining a snapshot of the immediate cellular context (i.e., the sorting endosomes) of these antibodies and studying their 3D behavior within sorting endosomes. However, this imaging system could be utilized to study the cellular behavior of a plethora of other proteins or macromolecules and their interactions with subcellular organelles such as endosomes, lysosomes, Golgi or the endoplasmic reticulum.

4. SELECTIVE DEPLETION OF RADIOLABELLED HER2-SPECIFIC ANTIBODY FOR PET CONTRAST IMPROVEMENT

4.1. Introduction

The use of engineering approaches to generate antibodies of high affinity and specificity for target has led to an expansion of interest in using these agents as diagnostic and theranostic imaging agents. However, antibodies of the IgG class are endowed with long in vivo persistence due to their ability to bind to the receptor, FcRn (*30*). This longevity results in high background, poor contrast and, if radiolabeled for detection using positron emission tomography (PET), potential radiation damage to normal tissue (*258–260*). The current study is directed towards overcoming these limitations by using a novel approach to selectively clear target-specific antibody that is not tumor-bound during PET.

We have recently developed engineered antigen-Fc fusion proteins that selectively clear antigen (target)-specific antibodies without affecting the levels of endogenous antibodies of other specificities (*70*). These engineered fusion proteins, named Seldegs (for selective degradation), comprise an antigen component that is fused to an Fc-based targeting component. The targeting component is engineered to bind to the internalizing receptor, FcRn, with substantially increased affinity at near neutral and acidic pH (*47*, *70*). This binding behavior leads to rapid internalization of antibody-Seldeg complexes into FcRn-expressing cells followed by lysosomal degradation. Consequently, Seldeg delivery results in the selective depletion of antigen-specific antibodies (*70*).

Our recent studies have demonstrated that specifically designed Seldegs can be used to deplete antibodies specific for the autoantigen, myelin oligodendrocyte glycoprotein (MOG), and the tumor target HER2 (*70*, *261*). In addition, we have shown that the depletion of MOG-specific antibodies results in the amelioration of antibody-mediated disease in mice (*261*). However, the efficacy of Seldegs in reducing background and enhancing contrast during PET analyses in tumor-bearing mice has not been investigated. In the current study, we describe a strategy using a Seldeg that targets HER2-specific antibodies such as pertuzumab (*262*) to substantially improve contrast during PET.

4.2. Materials and methods

4.2.1. Antibodies and radiolabeling

Pertuzumab(*262*) was obtained from the UT Southwestern Medical Center Pharmacy (University of Texas Southwestern) and was labeled with ^{124}I (PerkinElmer) using the Iodogen reagent in pre-coated tubes (Pierce)(*49*). The Na^{124}I (369 µCi) solution was firstly mixed with Na^{nat}I (667 pmol, 0.1 µg, 10 µl) solution and then added to each Iodogen tube containing (~246 µg pertuzumab in phosphate buffered saline (PBS). The iodination reaction was carried out for 15 min at room temperature. At the end of the reaction, the product solution was mixed with 10 µl of 10 mg/ml L-ascorbic acid solution in a 5 ml tube, and radiolabeled pertuzumab was isolated using a 10 kDa Amicon Ultra-4 centrifugal filter unit (Millipore Sigma). Radiolabeled pertuzumab was analyzed using instant thin layer chromatography medium (iTLC) and PBS as the developing solution, and the radiochemical purity of the 124I-labeled pertuzumab was over 95%.

4.2.2. Expression and purification of Seldegs

Expression constructs encoding heterodimeric HER2-Seldeg or MOG-Seldeg(*70*) were transiently transfected into HEK-293F (Life Technologies) cells using Gibco Expi293 expression system kits (Life Technologies). Recombinant proteins were purified from culture supernatants using protein A-Sepharose followed by anion exchange chromatography (SOURCE-15Q column, GE Healthcare) at pH 8.0 as described previously (*70*). Before use in experiments, the recombinant proteins were further purified using size exclusion chromatography (Hiload 16/600 Superdex 200 gel filtration column; GE Healthcare). Purified proteins were analyzed using a Phenomenex Yarra 3 μm SEC-3000 column (Phenomenex, 00H-4513-K0).

4.2.3. Mice and Tumor Implantation

All animal experiments described in this study were approved by the Texas A&M University and UT Southwestern Medical Center Institutional Animal Care and Use Committees. Experiments were carried out in 8-10 wk-old SCID BALB/c female mice (Jackson Laboratory) that were bred in a pathogen-free facility at Texas A&M University. To implant tumor xenografts, HCC1954 cells (0.5×10^6 cells/mouse) suspended in 0.1 mL of RPMI-1640/Matrigel (Corning Inc.) (1:1 ratio of medium:Matrigel) were injected into the fat pad of mammary gland number 3 of each mouse using a 22-gauge needle as described previously(*68*). Tumor-implanted mice were shipped to UT Southwestern Medical Center for use in PET experiments.

4.2.4. PET imaging study

Seven days following tumor implantation, when tumors were approximately ~175-300 mm^3 in volume, mice were divided into three equivalent groups (3 mice per treatment group) and injected intravenously with ^{124}I labeled pertuzumab. Thyroid uptake of radiolabeled iodine was reduced by adding Lugol solution to drinking water 48 h before the injection of radiolabeled proteins. To block stomach uptake of radiolabeled iodine, mice underwent gastric lavage using 1.5 mg of potassium perchlorate in 0.2 ml PBS. Thirty minutes before injection of radiolabeled (^{124}I-labeled) antibody (2.96-3.33 MBq, 60 μg antibody/mouse in a volume of 100 μl via tail vein injection). Twenty four hours after injection of radiolabeled pertuzumab, mice were injected intravenously with 51 μg HER2-Seldeg, 31 μg MOG-Seldeg, or vehicle (PBS). These Seldeg doses are equimolar with the injected dose of pertuzumab. PET and CT images were acquired at the indicated times, with acquisition of CT images immediately before PET imaging.

4.2.5. Image Acquisition

Small animal PET/CT imaging was performed with a Siemens Inveon PET-CT Multimodality System (Siemens Medical Solutions, Inc., Knoxville, TN). The CT images were acquired at 180 projections over a full rotation at 80 kV and 500 μA for 15 minutes with an exposure time of 140ms. PET images were acquired immediately after CT data acquisition for 15 minutes with an acquisition energy window of 350-650 keV for ^{124}I. During imaging acquisition, mice were sedated on the imaging bed using 2% isoflurane. A 3D Ordered-Subset Expectation Maximization followed by Maximum a Posteriori (OSEM3D/MAP) algorithm at 1.5mm intrinsic spatial target resolution, was used to

reconstruct the PET images. The Siemens Inveon Acquisition Workplace (Siemens Medical Solutions, Inc., Knoxville, TN) was made use for this purpose.

4.2.6. Image Analysis

PET and CT images were registered in the AMIDE software package (*263*). Linear intensity adjustments with a zero-minimum threshold were applied to display the PET images. The maximum thresholds were adjusted equally across all three groups and time points. The CT images were down sampled by a factor of 2 and set to interpolate bilinearly using a Shepp-Logan filter. For measuring the contrast, two ellipsoidal regions of interest (ROIs) were defined manually. One ROI encompassed the tumor in all planes. A second ROI was defined in the thorax area to measure the background intensity. The mean background intensity and the mean tumor intensity were calculated by taking the average of the intensity of the voxels within both the ROIs. This was carried out for each mouse. The dimensionless Contrast Measure (CM) is defined as:

$$CM = (I_T - I_b) / I_b$$

where I_T and I_b denote the mean tumor intensity and the mean background intensity, respectively. 3D animal images were generated using the 3D volume rendering tool available in the AMIDE software.

4.2.7. Statistics

Tests for statistical significance between treatment groups were performed using one-way analysis of variance (ANOVA) with Tukey's multiple comparison test and

plotted in GraphPad Prism, V6.0 (GraphPad Software). p values less than 0.05 were considered to be significant.

4.3. Results

4.3.1. Design and size exclusion analyses of Seldegs.

The Fc-antigen fusion protein, HER2-Seldeg, used for these studies is designed to rapidly and selectively capture anti-HER2 antibodies and direct them to degradative endolysosomal pathways by binding to FcRn expressing cells at neutral pH with enhanced affinity(*70*). This results in a more targeted clearance than seen in other engineered antibodies with increased binding to FcRn at near-neutral pH(*25*). The design of Seldegs and their analysis following purification are shown in Figure 4.1. For use as a control for the Seldeg targeting HER2-specific antibodies (HER2-Seldeg), a Seldeg in which extracellular domains I-IV of HER2 were replaced with the extracellular domain of myelin oligodendrocyte glycoprotein (MOG-Seldeg) was produced. In earlier studies, both HER2- and MOG-Seldegs have been shown to deplete antigen-specific antibody levels, whilst not affecting the levels of endogenous IgGs, in mice (*70*).

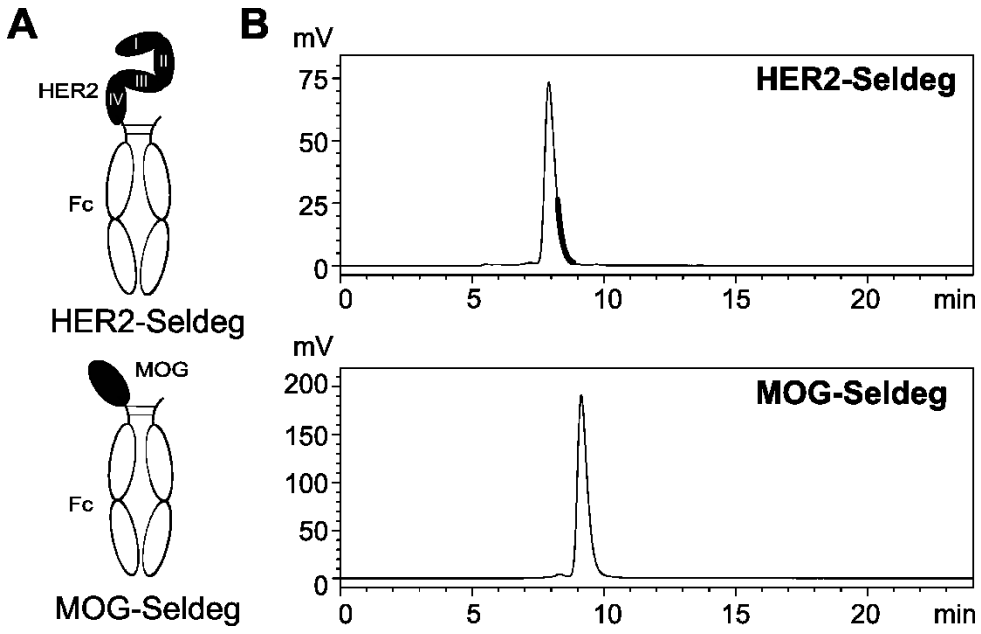

Figure 4.1 Design and size exclusion analyses of Seldegs
A, Schematic representation of the design of the Fc fusion proteins. HER2-Seldeg and MOG-Seldeg consist of domains I-IV of HER2 and the extracellular domain of MOG, respectively, fused to a heterodimeric Fc fragment that is engineered to bind with increased affinity to FcRn. B, Analyses of the purified Seldegs using a Phenomenex Yarra 3 μm SEC-3000 column (Phenomenex, 00H-4513-K0).

4.3.2. Selective clearance of anti-HER2 antibody by HER2-Seldeg improves contrast during PET

To analyze the ability of the HER2-Seldeg to improve contrast during diagnostic imaging, mice were implanted with the HER2-overexpressing tumor cell line, HCC1954. When tumors reached a size of ~175-300 mm^3, mice were injected with 124-I pertuzumab (HER2-specific). The mice were imaged using PET at 4-6 hours post-injection. HER2-Seldeg or controls (MOG-Seldeg or PBS vehicle) were delivered at 24 hours post-

pertuzumab injection. Radioactivity levels of whole body were taken before HER2-Seldeg (and control) injections and finally at 44 h time point. Delivery of the HER2-Seldeg resulted in a substantial decrease in whole body levels of radiolabel compared with that in control groups (Figure 4.2 A). Mice were analyzed using PET at 6 or 20 hours post-Seldeg injection (Figure 4.2 B).

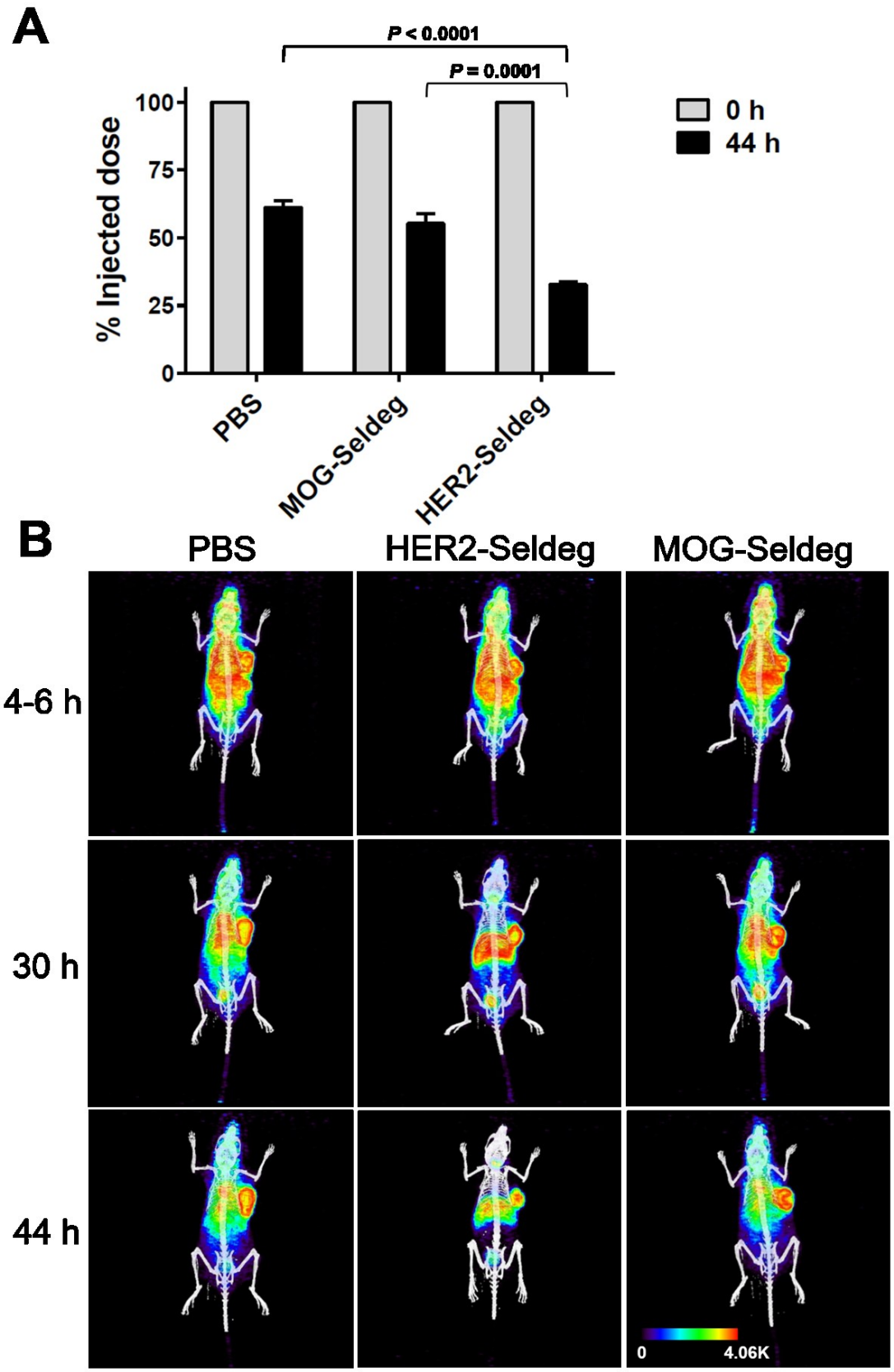
A
P < 0.0001
P = 0.0001
% Injected dose
100
75
50
25
0
0 h
44 h
PBS
MOG-Seldeg
HER2-Seldeg
B
PBS
HER2-Seldeg
MOG-Seldeg
4-6 h
30 h
44 h
0
4.06K

Figure 4.2 Effect of delivery of HER2-Seldeg following injection of radiolabeled pertuzumab into tumor-bearing mice

Twenty four hours following intravenous injection of ^{124}I-pertuzumab, mice (n = 3 mice/group) were intravenously injected with 51 μg of HER2-Seldeg, 31 μg of MOG-Seldeg or PBS vehicle. Seldeg amounts were equimolar with the amount of injected pertuzumab. A, Whole body counts immediately following radiolabeled pertuzumab injection and 44 h later (20 hours post-Seldeg delivery) are shown, with data normalized to the injected dose. Error bars indicate SD and significant differences are indicated for HER2-Seldeg-treatment groups vs. control groups by one-way ANOVA with Tukey's multiple comparison test. B, PET/CT images acquired at 4-6, 30, and 44 h after injection of radiolabeled pertuzumab. The time points correspond to 20 hours prior to, and 6 and 20 following, delivery of Seldeg, respectively. Data for one representative mouse per treatment group is shown, with linear scale bars. Data are representative of two independent experiments (n = 3 mice per treatment group).

The effect of HER2-Seldeg delivery on PET contrast was measured as described in Section 4.2.6. Two ellipsoidal ROIs- one encompassing the tumor and another defining the thorax area, was segmented manually. Figure 4.3 shows the different views (coronal, sagittal, and transverse) of the tumor and thorax ROIs.

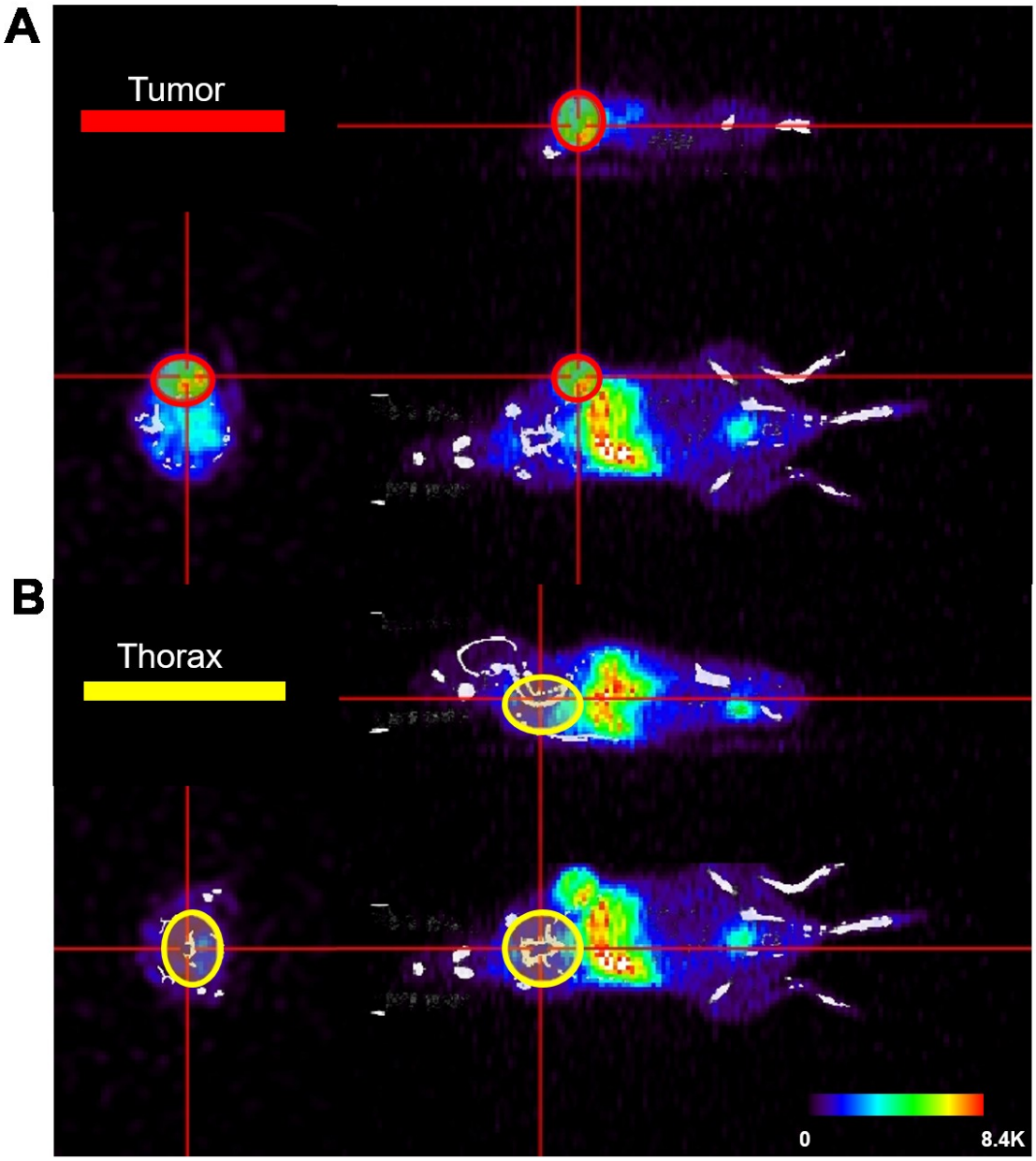

Figure 4.3 Different views of the region of interest (ROI)
Tumor ROI A, and the thorax ROI B, were overlaid with PET and CT images to determine contrast measures (ROIs for a PBS-treated mouse from the experiment described in Figure 4.2 is shown as an example). The intensity in the displays is linearly adjusted.

Contrast measures at 30 h, and 44 h after injection of radiolabeled pertuzumab for HER2-Seldeg treatment group was significantly higher relative to control (MOG-Seldeg and PBS, Figure 4.4). The delivery of HER2-Seldeg resulted in 2.5-3 fold higher contrast for the radiolabeled pertuzumab compared with that in control groups. In addition, and consistent with our earlier biodistribution studies (*261*), Seldeg injection resulted in the delivery of targeted antibody to the liver. We also observed that although imaging mice at 6 or 8 hours post-Seldeg delivery resulted in similar contrast measures, analyses at 3 hours resulted in ~2 fold lower contrast (n = 4 mice).

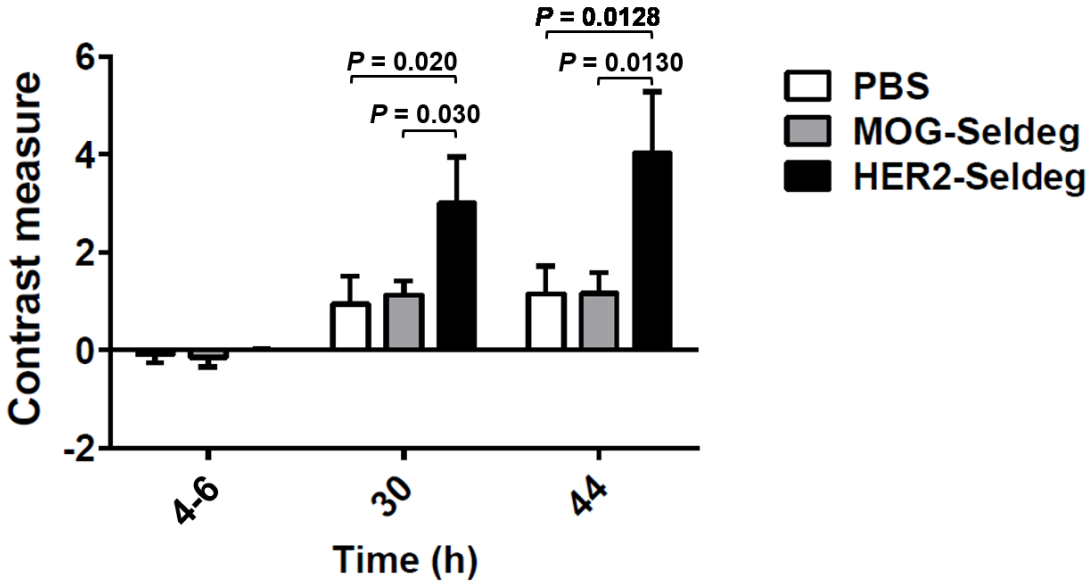

Figure 4.4 Effect of delivery of Seldeg on PET contrast
Tumor-bearing mice were treated as in Figure 2. Contrast measures were determined at 4-6, 30, and 44 h after injection of radiolabeled pertuzumab. These time points correspond to 20 h prior to, and 6 and 20 h following, Seldeg delivery, respectively. Error bars indicate SD and significant differences are indicated for HER2-Seldeg-treatment groups vs. control groups by one-way ANOVA with Tukey's multiple comparison test. Data shown are

representative of two independent experiments (n = 3 mice per treatment group in each experiment).

4.4. Discussion

In the current study we have demonstrated that engineered antigen-Fc fusions with the ability to selectively degrade antigen-specific antibodies can be used to improve contrast during the use of radiolabeled HER2-specific antibody, pertuzumab, to image HER2-positive tumors. This novel approach is expected to be broadly applicable, using appropriately engineered antigen-Fc fusions, to imaging with antibodies or other molecular agents specific for different (tumor) targets. Importantly, through their ability to bind and internalize antibodies with a particular specificity into lysosomes in cells, Seldegs do not affect the levels of endogenous, protective antibodies (*70*).

When used as imaging agents, the prolonged *in vivo* persistence of antibodies necessitates intervals of 4-7 days between the delivery of radiolabeled antibody and PET (or other imaging modality) (*264*, *265*). This wait time can lead to undesirable exposure of normal tissue to radiation. Pretargeting, involving the delivery of unlabeled, derivatized antibody followed by injection of radiolabeled PET probe that is designed to conjugate to the antibody, has been developed as an approach to overcome this problem (*266*, *267*). Shortcomings of pretargeting are the need for wait times for unbound, long-lived antibody to clear and the use of high levels of radiolabel. The application of Seldegs is expected to enable the exposure time to radiolabel to be substantially shortened due to the ability of these Fc fusions to deplete targeted antibody levels in the circulation within several hours

of delivery(*70*). In this context, although the use of antibody fragments with considerably reduced *in vivo* half-lives can be used to reduce radiation exposure times (*268*, *269*), the short half-life of the imaging agent can limit the levels that accumulate in the tumor. Alternatively, high dose intravenous gammaglobulin (IVIG), which acts as a competitor with endogenous IgG for binding to the salvage receptor, FcRn, has been used to clear background during imaging with labeled antibodies (*259*, *264*). In addition to reducing radiolabeled antibody levels, this results in decreases in endogenous antibody (IgG) levels for up to several weeks due to the pharmacokinetic behavior of IVIG (*270*, *271*). Although the limitations of using high doses of IVIG can be overcome by using an engineered, high affinity antagonist of FcRn with relatively short *in vivo* persistence to enhance PET contrast, this approach also results in the lowering of IgGs independent of their specificity (*50*, *68*). Consequently, Seldegs have the potential to provide an alternative, highly specific strategy to improve contrast and reduce background during diagnostic imaging. Further, the utility of Seldegs not only has relevance to the effective use of antibodies in imaging, but also to other classes of molecular diagnostics for which the regulated clearance of circulating agent is desirable.

5. CONCLUSIONS AND FUTURE DIRECTIONS

The MHC class I-related receptor, FcRn, is a multifunctional protein with responsibilities ranging from regulation of IgG and albumin levels in the body to antigen presentation. The past decade has seen an enormous increase in engineering strategies to modulate the dynamics of antibodies and antigens with FcRn. FcRn-targeted engineering approaches have given rise to engineered antibodies with therapeutical and diagnostic implications. The trafficking of engineered antibodies in the body is a multiscale process, taking place at subcellular, intracellular, and organ levels. It is essential to employ techniques capable of capturing the dynamics at these various scales, to gain detailed mechanistic insights of engineered antibodies. Advanced imaging techniques are powerful tools for studying biological systems. Advances in the field of imaging have enabled imaging of biological systems at nano-, meso- and macro-scale possible. Many imaging approaches like fluorescence microscopy, electron microscopy, and single molecule microscopy have been routinely utilized for studying fundamental biomolecular interactions. We utilize advanced imaging modalities to capitulate the dynamics of Fc-engineered antibodies at different scales.

In this study, we investigated the fate of antibody-opsonized tumor cells after phagocytosis in macrophages, an intracellular or micrometer-scale process, using microscopy techniques. Results show a vacuole-like structure associated with the phagosomes exhibiting distinct characteristics. The vacuoles were lysosomal, but interestingly, ratiometric analyses revealed a higher pH in the vacuole compartment

compared to the phagosome. They are separated by a semi-permeable membrane from the phagosomes, as demonstrated by EM studies. Inhibition of the mTOR pathway increased the size of the phagosome-associated vacuole-like structure. The identification of this vacuole-like compartment has implications for understanding the subsequent processes involved in the degradation of antibody-opsonized tumor cells. Antigen-loading compartments in APCs have been shown to maintain high pH favorable for lower degradation (*121*, *222*). The vacuoles have higher pH than the phagosomes, suggesting that they could play a role in antigen-presentation. Future directions will focus on exploring the functions of this vacuole in cross-presentation related to phagocytosis.

The use of high-resolution imaging approaches to study subcellular dynamics provides mechanistic insight with excellent spatiotemporal resolution. Studies focusing on understanding the subcellular dynamics of Fc-engineered antibodies at the subcellular and single molecular levels are essential in predicting its *in vivo* behavior and consequently its therapeutic potential. Currently, many advanced imaging methods are available for studying the dynamics of single molecule at the nanometer-scale. However, it is important to image the single molecule along with its interacting cellular context to make meaningful implications for the trafficking events. We imaged the 3D dynamics of two engineered FcRn-inhibitors at the subcellular level, using an advanced imaging platform- rMUM. The prototype of rMUM setup was previously described by our group (*173*). The multifocal plane microscopy module (MUM-module) of the rMUM setup images the dynamics of single molecules completely, while the remote focusing module (r-module) does a z-scan of the interacting cellular organelles. This enables compensation

of the motion of a single molecule with the organelle's movement, thus giving a real snapshot of the dynamics.

In this current study, we used this multi-dimensional, nanometer resolution microscopy technique to image the dynamics of the two engineered FcRn-inhibitors. We successfully tracked and visualized the engineered FcRn-inhibitors localize on the inner leaflet of sorting endosomes. This has opened avenues for future studies directed towards utilizing quantitative measures to study the engineered antibodies in detail. Our study focused on imaging the immediate cellular context, sorting endosomes. However, the rMUM setup is very powerful and is capable of imaging even the global cellular context of the single molecules. By modifying the depth of z-stacks captured by the r-module and other imaging parameters, different subcellular organelles and processes can be imaged with high-resolution.

In our third study, at the macro or millimeter level, PET imaging of tumor-bearing mice revealed that delivery of the HER2-Seldeg resulted in a substantial decrease in whole body levels of radiolabel and a 2.5-3 fold higher contrast for the radiolabeled pertuzumab compared with that in control groups. Seldeg injection also resulted in the delivery of targeted antibody to the liver, consistent with our previous study. It is to be noted that the liver harbors a large population of tissue-resident macrophages in the body (*272*, *273*). Macrophages are highly pinocytic in nature and expresses high levels of very active FcRn and acts as a degradative sink in the absence of FcRn activity (*274*). We also observed that although imaging mice at 6 or 8 hours post-Seldeg delivery resulted in similar contrast measures, analyses at 3 hours resulted in 2 fold lower contrast.

6. REFERENCES

1. D. C. Roopenian, S. Akilesh, FcRn: the neonatal Fc receptor comes of age. *Nat. Rev. Immunol.* **7**, 715–725 (2007).
2. E. S. Ward, R. J. Ober, Multitasking by exploitation of intracellular transport functions: the many faces of FcRn. *Advances in immunology,* **103**, pp. 77-115 (2009).
3. V. Ghetie, J. G. Hubbard, J.-K. Kim, M.-F. Tsen, Y. Lee, E. S. Ward, Abnormally short serum half-lives of IgG in β2-microglobulin-deficient mice. *Eur. J. Immunol.* **26**, 690–696 (1996).
4. R. P. Junghans, C. L. Anderson, The protection receptor for IgG catabolism is the beta2-microglobulin-containing neonatal intestinal transport receptor. *Proc. Natl. Acad. Sci.* **93**, 5512–5516 (1996).
5. S. M. Claypool, B. L. Dickinson, J. S. Wagner, F.-E. Johansen, N. Venu, J. A. Borawski, W. I. Lencer, R. S. Blumberg, Bidirectional Transepithelial IgG Transport by a Strongly Polarized Basolateral Membrane Fcγ-Receptor. *Mol. Biol. Cell*. **15**, 1746–1759 (2004).
6. B. L. Dickinson, K. Badizadegan, Z. Wu, J. C. Ahouse, X. Zhu, N. E. Simister, R. S. Blumberg, W. I. Lencer, Bidirectional FcRn-dependent IgG transport in a polarized human intestinal epithelial cell line. *J. Clin. Invest.* **104**, 903–911 (1999).
7. K. M. McCarthy, Y. Yoong, N. E. Simister, Bidirectional transcytosis of IgG by the rat neonatal Fc receptor expressed in a rat kidney cell line: a system to study

protein transport across epithelia. *J. Cell Sci.* **113**, 1277–1285 (2000).

8. H. P. Montoyo, C. Vaccaro, M. Hafner, R. J. Ober, W. Mueller, E. S. Ward, Conditional deletion of the MHC class I-related receptor FcRn reveals the sites of IgG homeostasis in mice. *Proc. Natl. Acad. Sci.* **106**, 2788–2793 (2009).
9. S. Akilesh, G. J. Christianson, D. C. Roopenian, A. S. Shaw, Neonatal FcR expression in bone marrow-derived cells functions to protect serum IgG from catabolism. *J. Immunol.* **179**, 4580–4588 (2007).
10. X. Zhu, G. Meng, B. L. Dickinson, X. Li, E. Mizoguchi, L. Miao, Y. Wang, C. Robert, B. Wu, P. D. Smith, MHC class I-related neonatal Fc receptor for IgG is functionally expressed in monocytes, intestinal macrophages, and dendritic cells. *J. Immunol.* **166**, 3266–3276 (2001).
11. N. E. Simister, K. E. Mostov, An Fc receptor structurally related to MHC class I antigens. *Nature*. **337**, 184–187 (1989).
12. D. K. Challa, R. Velmurugan, R. J. Ober, E. Sally Ward, FcRn: From Molecular interactions to regulation of IgG pharmacokinetics and functions. In: Fc Receptors. Curr. Top. Microbiol. Immunol. **382**, pp. 249–272 (2014).
13. M. Pyzik, T. Rath, W. I. Lencer, K. Baker, R. S. Blumberg, FcRn: the architect behind the immune and nonimmune functions of IgG and albumin. *J. Immunol.* **194**, 4595–4603 (2015).
14. S. M. Claypool, B. L. Dickinson, M. Yoshida, W. I. Lencer, R. S. Blumberg, Functional reconstitution of human FcRn in Madin-Darby canine kidney cells requires co-expressed human β2-microglobulin. *J. Biol. Chem.* **277**, 28038–28050

(2002).

15. J.-K. Kim, M.-F. Tsen, V. Ghetie, E. S. Ward, Localization of the site of the murine IgG1 molecule that is involved in binding to the murine intestinal Fc receptor. *Eur. J. Immunol.* **24**, 2429–2434 (1994).

16. W. L. Martin, A. P. West Jr, L. Gan, P. J. Bjorkman, Crystal structure at 2.8 Å of an FcRn/heterodimeric Fc complex: mechanism of pH-dependent binding. *Mol. Cell*. **7**, 867–877 (2001).

17. J. Kim, M. Firan, C. G. Radu, C. Kim, V. Ghetie, E. S. Ward, Mapping the site on human IgG for binding of the MHC class I-related receptor, FcRn. *Eur. J. Immunol.* **29**, 2819–2825 (1999).

18. J. Deisenhofer, Crystallographic refinement and atomic models of a human Fc fragment and its complex with fragment B of protein A from Staphylococcus aureus at 2.9-and 2.8-. ANG. resolution. *Biochemistry*. **20**, 2361–2370 (1981).

19. E. A. Kabat, T. Te Wu, H. M. Perry, C. Foeller, K. S. Gottesman, Sequences of proteins of immunological interest (DIANE publishing, 1992).

20. J. Kim, M. Tsen, V. Ghetie, E. Sally Ward, Identifying amino acid residues that influence plasma clearance of murine IgG1 fragments by site-directed mutagenesis. *Eur. J. Immunol.* **24**, 542–548 (1994).

21. M. Raghavan, V. R. Bonagura, S. L. Morrison, P. J. Bjorkman, Analysis of the pH dependence of the neonatal Fc receptor/immunoglobulin G interaction using antibody and receptor variants. *Biochemistry*. **34**, 14649–14657 (1995).

22. J. Zhou, J. E. Johnson, V. Ghetie, R. J. Ober, E. S. Ward, Generation of mutated

variants of the human form of the MHC class I-related receptor, FcRn, with increased affinity for mouse immunoglobulin G. *J. Mol. Biol.* **332**, 901–913 (2003).

23. R. J. Ober, C. G. Radu, V. Ghetie, E. S. Ward, Differences in promiscuity for antibody–FcRn interactions across species: implications for therapeutic antibodies. *Int. Immunol.* **13**, 1551–1559 (2001).

24. J. Zhou, F. Mateos, R. J. Ober, E. S. Ward, Conferring the binding properties of the mouse MHC class I-related receptor, FcRn, onto the human ortholog by sequential rounds of site-directed mutagenesis. *J. Mol. Biol.* **345**, 1071–1081 (2005).

25. C. Vaccaro, R. Bawdon, S. Wanjie, R. J. Ober, E. S. Ward, Divergent activities of an engineered antibody in murine and human systems have implications for therapeutic antibodies. *Proc. Natl. Acad. Sci. USA*. **103**, 18709–18714 (2006).

26. L. B. Avery, M. Wang, M. S. Kavosi, A. Joyce, J. C. Kurz, Y.-Y. Fan, M. E. Dowty, M. Zhang, Y. Zhang, A. Cheng, in *MAbs* (Taylor & Francis, 2016), vol. 8, pp. 1064–1078.

27. G. Proetzel, M. V Wiles, D. C. Roopenian, Genetically engineered humanized mouse models for preclinical antibody studies. *BioDrugs*. **28**, 171–180 (2014).

28. R. Rodewald, J.-P. Kraehenbuhl, Receptor-mediated transport of IgG. *J. Cell Biol.* **99**, 159s (1984).

29. K. H. Wallace, A. R. Rees, Studies on the immunoglobulin-G Fc-fragment receptor from neonatal rat small intestine. *Biochem. J.* **188**, 9–16 (1980).

30. E. S. Ward, R. J. Ober, Multitasking by exploitation of intracellular transport functions: the many faces of FcRn. *Adv. Immunol.* **103**, 77–115 (2009).

31. J. Borvak, J. Richardson, C. Medesan, F. Antohe, C. Radu, M. Simionescu, V. Ghetie, E. S. Ward, Functional expression of the MHC class I-related receptor, FcRn, in endothelial cells of mice. *Int. Immunol.* **10**, 1289–1298 (1998).

32. S. Akilesh, T. B. Huber, H. Wu, G. Wang, B. Hartleben, J. B. Kopp, J. H. Miner, D. C. Roopenian, E. R. Unanue, A. S. Shaw, Podocytes use FcRn to clear IgG from the glomerular basement membrane. *Proc. Natl. Acad. Sci.* **105**, 967–972 (2008).

33. F. Schlachetzki, C. Zhu, W. M. Pardridge, Expression of the neonatal Fc receptor (FcRn) at the blood–brain barrier. *J. Neurochem.* **81**, 203–206 (2002).

34. C. Chaudhury, S. Mehnaz, J. M. Robinson, W. L. Hayton, D. K. Pearl, D. C. Roopenian, C. L. Anderson, The major histocompatibility complex–related Fc receptor for IgG (FcRn) binds albumin and prolongs its lifespan. *J. Exp. Med.* **197**, 315–322 (2003).

35. M. Firan, R. Bawdon, C. Radu, R. J. Ober, D. Eaken, F. Antohe, V. Ghetie, E. S. Ward, The MHC class I-related receptor, FcRn, plays an essential role in the maternofetal transfer of γ-globulin in humans. *Int. Immunol.* **13**, 993–1002 (2001).

36. K. Baker, T. Rath, M. B. Flak, J. C. Arthur, Z. Chen, J. N. Glickman, I. Zlobec, E. Karamitopoulou, M. D. Stachler, R. D. Odze, Neonatal Fc receptor expression in dendritic cells mediates protective immunity against colorectal cancer. *Immunity*. **39**, 1095–1107 (2013).

37. K. Baker, S.-W. Qiao, T. T. Kuo, V. G. Aveson, B. Platzer, J.-T. Andersen, I. Sandlie, Z. Chen, C. de Haar, W. I. Lencer, Neonatal Fc receptor for IgG (FcRn) regulates cross-presentation of IgG immune complexes by CD8− CD11b+ dendritic

cells. *Proc. Natl. Acad. Sci.* **108**, 9927–9932 (2011).

38. S.-W. Qiao, K. Kobayashi, F.-E. Johansen, L. M. Sollid, J. T. Andersen, E. Milford, D. C. Roopenian, W. I. Lencer, R. S. Blumberg, Dependence of antibody-mediated presentation of antigen on FcRn. *Proc. Natl. Acad. Sci.* **105**, 9337–9342 (2008).

39. W. Mi, S. Wanjie, S.-T. Lo, Z. Gan, B. Pickl-Herk, R. J. Ober, E. S. Ward, Targeting the neonatal fc receptor for antigen delivery using engineered fc fragments. *J. Immunol.* **181**, 7550–7561 (2008).

40. R. J. Ober, C. Martinez, X. Lai, J. Zhou, E. S. Ward, Exocytosis of IgG as mediated by the receptor, FcRn: An analysis at the single-molecule level. *Proc. Natl. Acad. Sci.* **101**, 11076–11081 (2004).

41. R. J. Ober, C. Martinez, C. Vaccaro, J. Zhou, E. S. Ward, Visualizing the Site and Dynamics of IgG Salvage by the MHC Class I-Related Receptor, FcRn. *J. Immunol.* **172**, 2021–2029 (2004).

42. P. Prabhat, Z. Gan, J. Chao, S. Ram, C. Vaccaro, S. Gibbons, R. J. Ober, E. S. Ward, Elucidation of intracellular recycling pathways leading to exocytosis of the Fc receptor, FcRn, by using multifocal plane microscopy. *Proc. Natl. Acad. Sci.* **104**, 5889–5894 (2007).

43. W. I. Lencer, R. S. Blumberg, A passionate kiss, then run: exocytosis and recycling of IgG by FcRn. *Trends Cell Biol.* **15**, 5–9 (2005).

44. A. W. Weflen, N. Baier, Q.-J. Tang, M. Van den Hof, R. S. Blumberg, W. I. Lencer, R. H. Massol, Multivalent immune complexes divert FcRn to lysosomes by exclusion from recycling sorting tubules. *Mol. Biol. Cell*. **24**, 2398–2405 (2013).

45. S. Tzaban, R. H. Massol, E. Yen, W. Hamman, S. R. Frank, L. A. Lapierre, S. H. Hansen, J. R. Goldenring, R. S. Blumberg, W. I. Lencer, The recycling and transcytotic pathways for IgG transport by FcRn are distinct and display an inherent polarity. *J. Cell Biol.* **185**, 673–684 (2009).

46. Z. Gan, S. Ram, R. J. Ober, E. S. Ward, Using multifocal plane microscopy to reveal novel trafficking processes in the recycling pathway. *J. Cell Sci.* **126**, 1176–1188 (2013).

47. E. S. Ward, R. J. Ober, Targeting FcRn to Generate Antibody-Based Therapeutics. *Trends Pharmacol. Sci.* **39**, 892–904 (2018).

48. T. Igawa, S. Ishii, T. Tachibana, A. Maeda, Y. Higuchi, S. Shimaoka, C. Moriyama, T. Watanabe, R. Takubo, Y. Doi, Antibody recycling by engineered pH-dependent antigen binding improves the duration of antigen neutralization. *Nat. Biotechnol.* **28**, 1203–1207 (2010).

49. C. Vaccaro, J. Zhou, R. J. Ober, E. S. Ward, Engineering the Fc region of immunoglobulin G to modulate in vivo antibody levels. *Nat. Biotechnol.* **23**, 1283–1288 (2005).

50. P. Ulrichts, A. Guglietta, T. Dreier, T. van Bragt, V. Hanssens, E. Hofman, B. Vankerckhoven, P. Verheesen, N. Ongenae, V. Lykhopiy, F. J. Enriquez, J. Cho, R. J. Ober, E. S. Ward, H. de Haard, N. Leupin, Neonatal Fc receptor antagonist efgartigimod safely and sustainably reduces IgGs in humans. *J. Clin. Invest.* **128**, 4372–4386 (2018).

51. L. Liu, A. M. Garcia, H. Santoro, Y. Zhang, K. McDonnell, J. Dumont, A. Bitonti,

Amelioration of Experimental Autoimmune Myasthenia Gravis in Rats by Neonatal FcR Blockade. *J. Immunol.* **178**, 5390–5398 (2007).

52. L. Blumberg, J. E. Humphries, K. C. Lasseter, R. S. Blumberg, SYNT001: a humanized IgG4 monoclonal antibody that disrupts the interaction of FcRn and IgG for the treatment of IgG-mediated autoimmune diseases. *Blood*. **130**, 3483 (2017).

53. P. Kiessling, R. Lledo-Garcia, S. Watanabe, G. Langdon, D. Tran, M. Bari, L. Christodoulou, E. Jones, G. Price, B. Smith, F. Brennan, I. White, S. Jolles, The FcRn inhibitor rozanolixizumab reduces human serum IgG concentration: A randomized phase 1 study. *Sci. Transl. Med.* **9**, eaan1208 (2017).

54. L. E. Ling, J. L. Hillson, R. G. Tiessen, T. Bosje, M. P. van Iersel, D. J. Nix, L. Markowitz, N. A. Cilfone, J. Duffner, J. B. Streisand, M281, an anti-FcRn antibody: pharmacodynamics, pharmacokinetics, and safety across the full range of IgG reduction in a first-in-human study. *Clin. Pharmacol. Ther.* **105**, 1031–1039 (2019).

55. D. A. Patel, A. Puig-Canto, D. K. Challa, H. P. Montoyo, R. J. Ober, E. S. Ward, Neonatal Fc receptor blockade by Fc engineering ameliorates arthritis in a murine model. *J. Immunol.* **187**, 1015–1022 (2011).

56. A. Khosroshahi, D. B. Bloch, V. Deshpande, J. H. Stone, Rituximab therapy leads to rapid decline of serum IgG4 levels and prompt clinical improvement in IgG4-related systemic disease. *Arthritis Rheum.* **62**, 1755–1762 (2010).

57. A. R. Ahmed, Z. Spigelman, L. A. Cavacini, M. R. Posner, Treatment of pemphigus vulgaris with rituximab and intravenous immune globulin. *N. Engl. J. Med.* **355**,

1772–1779 (2006).

58. S. C. Low, A. R. Mezo, Inhibitors of the FcRn:IgG Protein–Protein Interaction. *AAPS J.* **11**, 432 (2009).

59. A. E. Nixon, J. Chen, D. J. Sexton, A. Muruganandam, A. J. Bitonti, J. Dumont, M. Viswanathan, D. Martik, D. Wassaf, A. Mezo, Fully human monoclonal antibody inhibitors of the neonatal fc receptor reduce circulating IgG in non-human primates. *Front. Immunol.* **6**, 176 (2015).

60. J. Seijsing, S. Yu, F. Y. Frejd, I. Höiden-Guthenberg, T. Gräslund, In vivo depletion of serum IgG by an affibody molecule binding the neonatal Fc receptor. *Sci. Rep.* **8**, 1–9 (2018).

61. V. P. Werth, D. Culton, L. Blumberg, J. Humphries, R. Blumberg, R. Hall, FcRn blockade with SYNT001 for the treatment of pemphigus. *J Invest Dermatol*. **138**, S92 (2018).

62. T. Robak, I. Jarque, V. Musteata, P. Kiessling, U. Massow, J. Higginson, R. Snipes, S. Jolles, Phase II, multiple-dose study of anti-FcRn antibody, rozanolixizumab (UCB7665), in patients with primary immune thrombocytopenia: interim analysis. *Blood*. **130**, 15 (2017).

63. D. K. Challa, U. Bussmeyer, T. Khan, H. P. Montoyo, P. Bansal, R. J. Ober, E. S. Ward, in *MAbs* (Taylor & Francis, 2013), vol. 5, pp. 655–659.

64. E. S. Ward, S. C. Devanaboyina, R. J. Ober, Targeting FcRn for the modulation of antibody dynamics. *Mol. Immunol.* **67**, 131–141 (2015).

65. W. F. Dall'Acqua, R. M. Woods, E. S. Ward, S. R. Palaszynski, N. K. Patel, Y. A.

Brewah, H. Wu, P. A. Kiener, S. Langermann, Increasing the affinity of a human IgG1 for the neonatal Fc receptor: biological consequences. *J. Immunol.* **169**, 5171–5180 (2002).

66. K. E. Getman, J. P. Balthasar, Pharmacokinetic effects of 4C9, an anti-FcRn antibody, in rats: implications for the use of FcRn inhibitors for the treatment of humoral autoimmune and alloimmune conditions. *J. Pharm. Sci.* **94**, 718–729 (2005).

67. Z. Gan, S. Ram, C. Vaccaro, R. J. Ober, E. S. Ward, Analyses of the recycling receptor, FcRn, in live cells reveal novel pathways for lysosomal delivery. *Traffic*. **10**, 600–614 (2009).

68. R. Swiercz, S. Chiguru, A. Tahmasbi, S. M. Ramezani, G. Hao, D. K. Challa, M. A. Lewis, P. V Kulkarni, X. Sun, R. J. Ober, Use of Fc-engineered antibodies as clearing agents to increase contrast during PET. *J. Nucl. Med.* **55**, 1204–1207 (2014).

69. D. M. Goldenberg, C.-H. Chang, E. A. Rossi, Pretargeted molecular imaging and radioimmunotherapy. *Theranostics*. **2**, 523 (2012).

70. S. C. Devanaboyina, P. Khare, D. K. Challa, R. J. Ober, E. S. Ward, Engineered clearing agents for the selective depletion of antigen-specific antibodies. *Nat. Commun.* **8**, 1–6 (2017).

71. D. M. Ecker, S. D. Jones, H. L. Levine, The therapeutic monoclonal antibody market. *MAbs*. **7**, 9–14 (2015).

72. G. P. Adams, L. M. Weiner, Monoclonal antibody therapy of cancer. *Nat.*

Biotechnol. **23**, 1147–1157 (2005).

73. K. R. Rodgers, R. C. Chou, Therapeutic monoclonal antibodies and derivatives: Historical perspectives and future directions. *Biotechnol. Adv.* **34**, 1149–1158 (2016).

74. P. McLaughlin, A. J. Grillo-López, B. K. Link, R. Levy, M. S. Czuczman, M. E. Williams, M. R. Heyman, I. Bence-Bruckler, C. A. White, F. Cabanillas, Rituximab chimeric anti-CD20 monoclonal antibody therapy for relapsed indolent lymphoma: half of patients respond to a four-dose treatment program. *J. Clin. Oncol.* **16**, 2825–2833 (1998).

75. S. Maximiano, P. Magalhaes, M. P. Guerreiro, M. Morgado, Trastuzumab in the treatment of breast cancer. *BioDrugs*. **30**, 75–86 (2016).

76. J. Teillaud, Antibody-dependent Cellular Cytotoxicity (ADCC). *eLS* (2012).

77. R. Gennari, S. Menard, F. Fagnoni, L. Ponchio, M. Scelsi, E. Tagliabue, F. Castiglioni, L. Villani, C. Magalotti, N. Gibelli, Pilot study of the mechanism of action of preoperative trastuzumab in patients with primary operable breast tumors overexpressing HER2. *Clin. Cancer Res.* **10**, 5650–5655 (2004).

78. T. Triulzi, V. Regondi, L. De Cecco, M. R. Cappelletti, M. Di Modica, B. Paolini, P. L. Lollini, S. Di Cosimo, L. Sfondrini, D. Generali, Early immune modulation by single-agent trastuzumab as a marker of trastuzumab benefit. *Br. J. Cancer*. **119**, 1487–1494 (2018).

79. X. Pivot, M. Pegram, J. Cortes, D. Lüftner, G. H. Lyman, G. Curigliano, I. Bondarenko, Y. C. Yoon, Y. Kim, C. Kim, Three-year follow-up from a phase 3

study of SB3 (a trastuzumab biosimilar) versus reference trastuzumab in the neoadjuvant setting for human epidermal growth factor receptor 2–positive breast cancer. *Eur. J. Cancer*. **120**, 1–9 (2019).

80. T. Masu, M. Atsukawa, K. Nakatsuka, M. Shimizu, D. Miura, T. Arai, H. Harimoto, C. Kondo, K. Kaneko, S. Futagami, Anti-CD137 monoclonal antibody enhances trastuzumab-induced, natural killer cell-mediated cytotoxicity against pancreatic cancer cell lines with low human epidermal growth factor-like receptor 2 expression. *PLoS One*. **13**, e0200664 (2018).

81. A. W. Pawluczkowycz, F. J. Beurskens, P. V Beum, M. A. Lindorfer, J. G. J. van de Winkel, P. W. H. I. Parren, R. P. Taylor, Binding of submaximal C1q promotes complement-dependent cytotoxicity (CDC) of B cells opsonized with anti-CD20 mAbs ofatumumab (OFA) or rituximab (RTX): considerably higher levels of CDC are induced by OFA than by RTX. *J. Immunol.* **183**, 749–758 (2009).

82. N. Prang, S. Preithner, K. Brischwein, A. Wöppel, J. Müller, C. Steiger, M. Peters, P. A. Baeuerle, A. J. da Silva, Cellular and complement-dependent cytotoxicity of Ep-CAM-specific monoclonal antibody MT201 against breast cancer cell lines. *Br. J. Cancer*. **92**, 342–349 (2005).

83. M. Leidi, E. Gotti, L. Bologna, E. Miranda, M. Rimoldi, A. Sica, M. Roncalli, G. A. Palumbo, M. Introna, J. Golay, M2 macrophages phagocytose rituximab-opsonized leukemic targets more efficiently than M1 cells in vitro. *J. Immunol.* **182**, 4415–4422 (2009).

84. S. Su, J. Zhao, Y. Xing, X. Zhang, J. Liu, Q. Ouyang, J. Chen, F. Su, Q. Liu, E.

Song, Immune checkpoint inhibition overcomes ADCP-induced immunosuppression by macrophages. *Cell*. **175**, 442–457 (2018).

85. M. Feng, W. Jiang, B. Y. S. Kim, C. C. Zhang, Y.-X. Fu, I. L. Weissman, Phagocytosis checkpoints as new targets for cancer immunotherapy. *Nat. Rev. Cancer*. **19**, 568–586 (2019).

86. R. Velmurugan, S. Ramakrishnan, M. Kim, R. J. Ober, E. S. Ward, Phagocytosis of antibody-opsonized tumor cells leads to the formation of a discrete vacuolar compartment in macrophages. *Traffic*. **19** (2018), doi:10.1111/tra.12552.

87. N. Gül, L. Babes, K. Siegmund, R. Korthouwer, M. Bögels, R. Braster, G. Vidarsson, T. L. M. ten Hagen, P. Kubes, M. van Egmond, Macrophages eliminate circulating tumor cells after monoclonal antibody therapy. *J. Clin. Invest.* **124**, 812–823 (2014).

88. K. Weiskopf, I. L. Weissman, Macrophages are critical effectors of antibody therapies for cancer. *MAbs*. **7**, 303–310 (2015).

89. R. Velmurugan, D. K. Challa, S. Ram, R. J. Ober, E. S. Ward, Macrophage-Mediated Trogocytosis Leads to Death of Antibody-Opsonized Tumor Cells. *Mol. Cancer Ther.* **15**, 1879–1889 (2016).

90. D. Ribatti, Mast cells and macrophages exert beneficial and detrimental effects on tumor progression and angiogenesis. *Immunol. Lett.* **152**, 83–88 (2013).

91. P. Luz-Crawford, C. Jorgensen, F. Djouad, Mesenchymal stem cells direct the immunological fate of macrophages. *Macrophages*, 61–72 (2017).

92. P. M. Hogarth, Fc receptors: Introduction. *Immunol. Rev.* **268**, 1–5 (2015).

93. J. E. Bakema, M. Van Egmond, The human immunoglobulin A Fc receptor FcαRI: a multifaceted regulator of mucosal immunity. *Mucosal Immunol.* **4**, 612–624 (2011).

94. D. MacGlashan, IgE and FcεRI regulation. *Clin. Rev. Allergy Immunol.* **29**, 49–60 (2005).

95. P. M. Hogarth, G. A. Pietersz, Fc receptor-targeted therapies for the treatment of inflammation, cancer and beyond. *Nat. Rev. Drug Discov.* **11**, 311–331 (2012).

96. F. Nimmerjahn, J. V Ravetch, Fcγ receptors as regulators of immune responses. *Nat. Rev. Immunol.* **8**, 34–47 (2008).

97. S. A. Freeman, S. Grinstein, Phagocytosis: receptors, signal integration, and the cytoskeleton. *Immunol. Rev.* **262**, 193–215 (2014).

98. P. Bruhns, B. Iannascoli, P. England, D. A. Mancardi, N. Fernandez, S. Jorieux, M. Daëron, Specificity and affinity of human Fcγ receptors and their polymorphic variants for human IgG subclasses. *Blood*. **113**, 3716–3725 (2009).

99. C. L. Anderson, L. Shen, D. M. Eicher, M. D. Wewers, J. K. Gill, Phagocytosis mediated by three distinct Fc gamma receptor classes on human leukocytes. *J. Exp. Med.* **171**, 1333–1345 (1990).

100. C. Rosales, E. Uribe-Querol, Phagocytosis: a fundamental process in immunity. *Biomed Res. Int.* **2017** (2017).

101. F. Nimmerjahn, J. V Ravetch, Fc-receptors as regulators of immunity. *Adv. Immunol.* **96**, 179–204 (2007).

102. T. Takai, Roles of Fc receptors in autoimmunity. *Nat. Rev. Immunol.* **2**, 580–592

(2002).

103. R. S. Flannagan, V. Jaumouillé, S. Grinstein, The cell biology of phagocytosis. *Annu. Rev. Pathol.* **7**, 61–98 (2012).

104. R. Clynes, J. S. Maizes, R. Guinamard, M. Ono, T. Takai, J. V Ravetch, Modulation of immune complex–induced inflammation in vivo by the coordinate expression of activation and inhibitory Fc receptors. *J. Exp. Med.* **189**, 179–186 (1999).

105. R. Braster, T. O'Toole, M. van Egmond, Myeloid cells as effector cells for monoclonal antibody therapy of cancer. *Methods*. **65**, 28–37 (2014).

106. R. Noy, J. W. Pollard, Tumor-Associated Macrophages: From Mechanisms to Therapy. *Immunity*. **41**, 49–61 (2014).

107. N. Gül, M. van Egmond, Antibody-dependent phagocytosis of tumor cells by macrophages: a potent effector mechanism of monoclonal antibody therapy of cancer. *Cancer Res.* **75**, 5008–5013 (2015).

108. R. Levin, S. Grinstein, J. Canton, The life cycle of phagosomes: formation, maturation, and resolution. *Immunol. Rev.* **273**, 156–179 (2016).

109. M. T. Crowley, P. S. Costello, C. J. Fitzer-Attas, M. Turner, F. Meng, C. Lowell, V. L. J. Tybulewicz, A. L. DeFranco, A critical role for Syk in signal transduction and phagocytosis mediated by Fcγ receptors on macrophages. *J. Exp. Med.* **186**, 1027–1039 (1997).

110. H. Kawasaki, G. M. Springett, S. Toki, J. J. Canales, P. Harlan, J. P. Blumenstiel, E. J. Chen, I. A. Bany, N. Mochizuki, A. Ashbacher, A Rap guanine nucleotide exchange factor enriched highly in the basal ganglia. *Proc. Natl. Acad. Sci.* **95**,

13278–13283 (1998).

111. R. J. Botelho, M. Teruel, R. Dierckman, R. Anderson, A. Wells, J. D. York, T. Meyer, S. Grinstein, Localized biphasic changes in phosphatidylinositol-4, 5-bisphosphate at sites of phagocytosis. *J. Cell Biol.* **151**, 1353–1368 (2000).

112. F. Guo, Y. Ding, N. Caberoy, G. Alvarado, F. Wang, R. Chen, W. Li, ABCF1 extrinsically regulates retinal pigment epithelial cell phagocytosis. *Mol. Biol. Cell*. **26**, 2311–2320 (2015).

113. Y. Gottlieb, O. Topaz, L. A. Cohen, L. D. Yakov, T. Haber, A. Morgenstern, A. Weiss, K. C. Berman, E. Fibach, E. G. Meyron-Holtz, Physiologically aged red blood cells undergo erythrophagocytosis in vivo but not in vitro. *Haematologica*. **97**, 994 (2012).

114. C. Farrera, B. Fadeel, Macrophage clearance of neutrophil extracellular traps is a silent process. *J. Immunol.* **191**, 2647–2656 (2013).

115. A. C. Humphries, S. K. Donnelly, M. Way, Cdc42 and the Rho GEF intersectin-1 collaborate with Nck to promote N-WASP-dependent actin polymerisation. *J. Cell Sci.* **127**, 673–685 (2014).

116. H. Park, D. Cox, Cdc42 regulates Fcγ receptor-mediated phagocytosis through the activation and phosphorylation of Wiskott-Aldrich syndrome protein (WASP) and neural-WASP. *Mol. Biol. Cell*. **20**, 4500–4508 (2009).

117. A. E. Dart, S. K. Donnelly, D. W. Holden, M. Way, E. Caron, Nck and Cdc42 co-operate to recruit N-WASP to promote FcγR-mediated phagocytosis. *J. Cell Sci.* **125**, 2825–2830 (2012).

118. M. Desjardins, L. A. Huber, R. G. Parton, G. Griffiths, Biogenesis of phagolysosomes proceeds through a sequential series of interactions with the endocytic apparatus. *J. Cell Biol.* **124**, 677–688 (1994).

119. G. L. Lukacs, O. D. Rotstein, S. Grinstein, Determinants of the phagosomal pH in macrophages. In situ assessment of vacuolar H (+)-ATPase activity, counterion conductance, and H+" leak". *J. Biol. Chem.* **266**, 24540–24548 (1991).

120. S. Greenberg, S. Grinstein, Phagocytosis and innate immunity. *Curr. Opin. Immunol.* **14**, 136–145 (2002).

121. A. Alloatti, F. Kotsias, J. G. Magalhaes, S. Amigorena, Dendritic cell maturation and cross-presentation: timing matters! *Immunol. Rev.* **272**, 97–108 (2016).

122. M. T. Tassin, T. Lang, J. C. Antoine, R. Hellio, A. Ryter, Modified lysosomal compartment as carrier of slowly and non-degradable tracers in macrophages. *Eur J Cell Biol*. **52**, 219–228 (1990).

123. E. Joly, D. Hudrisier, What is trogocytosis and what is its purpose? *Nat. Immunol.* **4**, 815 (2003).

124. P. V Beum, D. A. Mack, A. W. Pawluczkowycz, M. A. Lindorfer, R. P. Taylor, Binding of rituximab, trastuzumab, cetuximab, or mAb T101 to cancer cells promotes trogocytosis mediated by THP-1 cells and monocytes. *J. Immunol.* **181**, 8120–8132 (2008).

125. E. A. Rossi, D. M. Goldenberg, R. Michel, D. L. Rossi, D. J. Wallace, C.-H. Chang, Trogocytosis of multiple B-cell surface markers by CD22 targeting with epratuzumab. *Blood, J. Am. Soc. Hematol.* **122**, 3020–3029 (2013).

126. R. P. Taylor, M. A. Lindorfer, Fcγ-receptor–mediated trogocytosis impacts mAb-based therapies: historical precedence and recent developments. *Blood, J. Am. Soc. Hematol.* **125**, 762–766 (2015).

127. H. Taguchi, T. Ueno, H. Tadakuma, M. Yoshida, T. Funatsu, Single-molecule observation of protein–protein interactions in the chaperonin system. *Nat. Biotechnol.* **19**, 861–865 (2001).

128. R. Iino, I. Koyama, A. Kusumi, Single molecule imaging of green fluorescent proteins in living cells: E-cadherin forms oligomers on the free cell surface. *Biophys. J.* **80**, 2667–2677 (2001).

129. A. Yildiz, Myosin V Walks Hand-Over-Hand: Single Fluorophore Imaging with 1.5-nm Localization. *Science (80-.).* **300**, 2061–2065 (2003).

130. J. Zlatanova, K. Van Holde, Single-molecule biology: what is it and how does it work? *Mol. Cell*. **24**, 317–329 (2006).

131. M. Bruchez, M. Moronne, P. Gin, S. Weiss, A. P. Alivisatos, Semiconductor nanocrystals as fluorescent biological labels. *Science (80-.).* **281**, 2013–2016 (1998).

132. J. K. Jaiswal, S. M. Simon, Potentials and pitfalls of fluorescent quantum dots for biological imaging. *Trends Cell Biol.* **14**, 497–504 (2004).

133. M. Born, E. Wolf, Principles of Optics, 7th (expanded) edition. *United Kingdom Press Synd. Univ. Cambridge*. **461** (1999).

134. D. Axelrod, Total internal reflection fluorescence microscopy. *Methods Cell Biol.* **30**, 245–270 (1989).

135. G. I. Mashanov, D. Tacon, A. E. Knight, M. Peckham, J. E. Molloy, Visualizing single molecules inside living cells using total internal reflection fluorescence microscopy. *Methods*. **29**, 142–152 (2003).

136. S. B. Andersson, Tracking a single fluorescent molecule with a confocal microscope. *Appl. Phys. B*. **80**, 809–816 (2005).

137. S. R. P. Pavani, M. A. Thompson, J. S. Biteen, S. J. Lord, N. Liu, R. J. Twieg, R. Piestun, W. E. Moerner, Three-dimensional, single-molecule fluorescence imaging beyond the diffraction limit by using a double-helix point spread function. *Proc. Natl. Acad. Sci.* **106**, 2995-2999 (2009) doi:10.1073/pnas.0900245106.

138. L. Holtzer, T. Meckel, T. Schmidt, Nanometric three-dimensional tracking of individual quantum dots in cells. *Appl. Phys. Lett.* **90**, 53902 (2007).

139. W. E. Moerner, D. P. Fromm, Methods of single-molecule fluorescence spectroscopy and microscopy. *Rev. Sci. Instrum.* **74**, 3597–3619 (2003).

140. S. Ram, E. S. Ward, R. J. Ober, How accurately can a single molecule be localized when imaged through an optical microscope? *Proc SPIE*. *Imaging, Manipulation, and Analysis of Biomolecules and Cells: Fundamentals and Applications III*, vol. 5699, p. 426–435 (2005).

141. V. Levi, Q. Ruan, E. Gratton, 3-D particle tracking in a two-photon microscope: application to the study of molecular dynamics in cells. *Biophys. J.* **88**, 2919–2928 (2005).

142. E. Toprak, J. Enderlein, S. Syed, S. A. McKinney, R. G. Petschek, T. Ha, Y. E. Goldman, P. R. Selvin, Defocused orientation and position imaging (DOPI) of

myosin V. *Proc. Natl. Acad. Sci.* **103**, 6495–6499 (2006).

143. H. P. Kao, A. S. Verkman, Tracking of single fluorescent particles in three dimensions: use of cylindrical optics to encode particle position. *Biophys. J.* **67**, 1291–1300 (1994).

144. R. Piestun, Y. Y. Schechner, J. Shamir, Propagation-invariant wave fields with finite energy. *JOSA A*. **17**, 294–303 (2000).

145. S. Ram, P. Prabhat, J. Chao, E. Sally Ward, R. J. Ober, High Accuracy 3D Quantum Dot Tracking with Multifocal Plane Microscopy for the Study of Fast Intracellular Dynamics in Live Cells. *Biophys. J.* **95**, 6025–6043 (2008).

146. S. Ram, D. Kim, R. J. Ober, E. S. Ward, 3D single molecule tracking with multifocal plane microscopy reveals rapid intercellular transferrin transport at epithelial cell barriers. *Biophys. J.* **103**, 1594–1603 (2012).

147. S. Ram, D. Kim, E. S. Ward, R. J. Ober, Fast 3D Single Molecule Tracking with Multifocal Plane Microscopy in Polarized Epithelia Reveals a Novel Cellular Process of Intercellular Transfer. *Biophys. J.* **104**, 535a (2013).

148. S. Inoué, in *Methods in cell biology* (Elsevier, 1989), vol. 30, pp. 85–112.

149. R. J. Ober, S. Ram, E. S. Ward, Localization Accuracy in Single-Molecule Microscopy. *Biophys. J.* **86**, 1185–1200 (2004).

150. M. J. Saxton, K. Jacobson, Single-Particle Tracking:Applications to Membrane Dynamics. *Annu. Rev. Biophys. Biomol. Struct.* **26**, 373–399 (1997).

151. E. Betzig, G. H. Patterson, R. Sougrat, O. W. Lindwasser, S. Olenych, J. S. Bonifacino, M. W. Davidson, J. Lippincott-Schwartz, H. F. Hess, Imaging

intracellular fluorescent proteins at nanometer resolution. *Science (80-.).* **313**, 1642–1645 (2006).

152. M. J. Rust, M. Bates, X. Zhuang, Sub-diffraction-limit imaging by stochastic optical reconstruction microscopy (STORM). *Nat. Methods*. **3**, 793–796 (2006).

153. S. T. Hess, T. J. Gould, M. V Gudheti, S. A. Maas, K. D. Mills, J. Zimmerberg, Dynamic clustered distribution of hemagglutinin resolved at 40 nm in living cell membranes discriminates between raft theories. *Proc. Natl. Acad. Sci.* **104**, 17370–17375 (2007).

154. A. V Abraham, S. Ram, J. Chao, E. S. Ward, R. J. Ober, Quantitative study of single molecule location estimation techniques. *Opt. Express*. **17**, 23352 (2009).

155. S. Stallinga, B. Rieger, Position and orientation estimation of fixed dipole emitters using an effective Hermite point spread function model. *Opt. Express*. **20**, 5896–5921 (2012).

156. M. R. Vahid, J. Chao, D. Kim, E. S. Ward, R. J. Ober, State space approach to single molecule localization in fluorescence microscopy. *Biomed. Opt. Express*. **8**, 1332–1355 (2017).

157. B. Zhang, J. Zerubia, J.-C. Olivo-Marin, Gaussian approximations of fluorescence microscope point-spread function models. *Appl. Opt.* **46**, 1819–1829 (2007).

158. S. F. Gibson, F. Lanni, Experimental test of an analytical model of aberration in an oil-immersion objective lens used in three-dimensional light microscopy. *J. Opt. Soc. Am. A*. **9**, 154 (1992).

159. S. F. Gibson, F. Lanni, Diffraction by a circular aperture as a model for three-

dimensional optical microscopy. *JOSA A*. **6**, 1357–1367 (1989).

160. A. Tahmasbi, S. Ram, J. Chao, A. V Abraham, E. S. Ward, R. J. Ober, New results on the single molecule localization problem in two and three dimensions. *Proc SPIE Int Soc Opt Eng. Three-Dimensional and Multidimensional Microscopy: Image Acquisition and Processing XXII* vol. 9330, p. 933011 (2015).

161. J. Mertz, Strategies for volumetric imaging with a fluorescence microscope. *Optica*. **6**, 1261–1268 (2019).

162. K. M. Dean, P. Roudot, E. S. Welf, T. Pohlkamp, G. Garrelts, J. Herz, R. Fiolka, Imaging subcellular dynamics with fast and light-efficient volumetrically parallelized microscopy. *Optica*. **4**, 263–271 (2017).

163. L. Cong, Z. Wang, Y. Chai, W. Hang, C. Shang, W. Yang, L. Bai, J. Du, K. Wang, Q. Wen, Rapid whole brain imaging of neural activity in freely behaving larval zebrafish (Danio rerio). *Elife*. **6**, e28158 (2017).

164. O. Skocek, T. Nöbauer, L. Weilguny, F. M. Traub, C. N. Xia, M. I. Molodtsov, A. Grama, M. Yamagata, D. Aharoni, D. D. Cox, High-speed volumetric imaging of neuronal activity in freely moving rodents. *Nat. Methods*. **15**, 429–432 (2018).

165. B.-C. Chen, W. R. Legant, K. Wang, L. Shao, D. E. Milkie, M. W. Davidson, C. Janetopoulos, X. S. Wu, J. A. Hammer, Z. Liu, Lattice light-sheet microscopy: imaging molecules to embryos at high spatiotemporal resolution. *Science (80-.).* **346** (2014).

166. E. J. Botcherby, R. Juškaitis, T. Wilson, Scanning two photon fluorescence microscopy with extended depth of field. *Opt. Commun.* **268**, 253–260 (2006).

167. G. Thériault, Y. De Koninck, N. McCarthy, Extended depth of field microscopy for rapid volumetric two-photon imaging. *Opt. Express*. **21**, 10095–10104 (2013).

168. B. Chen, X. Huang, D. Gou, J. Zeng, G. Chen, M. Pang, Y. Hu, Z. Zhao, Y. Zhang, Z. Zhou, Rapid volumetric imaging with Bessel-Beam three-photon microscopy. *Biomed. Opt. Express*. **9**, 1992–2000 (2018).

169. R. Lu, W. Sun, Y. Liang, A. Kerlin, J. Bierfeld, J. D. Seelig, D. E. Wilson, B. Scholl, B. Mohar, M. Tanimoto, Video-rate volumetric functional imaging of the brain at synaptic resolution. *Nat. Neurosci.* **20**, 620–628 (2017).

170. A. Cheng, J. T. Gonçalves, P. Golshani, K. Arisaka, C. Portera-Cailliau, Simultaneous two-photon calcium imaging at different depths with spatiotemporal multiplexing. *Nat. Methods*. **8**, 139–142 (2011).

171. J. N. Stirman, I. T. Smith, M. W. Kudenov, S. L. Smith, Wide field-of-view, multi-region, two-photon imaging of neuronal activity in the mammalian brain. *Nat. Biotechnol.* **34**, 857–862 (2016).

172. S. Weisenburger, F. Tejera, J. Demas, B. Chen, J. Manley, F. T. Sparks, F. M. Traub, T. Daigle, H. Zeng, A. Losonczy, Volumetric Ca2+ imaging in the mouse brain using hybrid multiplexed sculpted light microscopy. *Cell*. **177**, 1050–1066 (2019).

173. J. Chao, R. Velmurugan, S. You, D. Kim, E. S. Ward, R. J. Ober, Remote focusing multifocal plane microscopy for the imaging of 3D single molecule dynamics with cellular context. *Proc.SPIE Int Soc Opt Eng.* 10070, *Three-Dimensional and Multidimensional Microscopy: Image Acquisition and Processing XXIV*, vol

10070, p. 100700L (2017)

174. C. W. Smith, E. J. Botcherby, T. Wilson, Resolution of oblique-plane images in sectioning microscopy. *Opt. Express*. **19**, 2662–2669 (2011).

175. E. J. Botcherby, R. Juškaitis, M. J. Booth, T. Wilson, An optical technique for remote focusing in microscopy. *Opt. Commun.* **281**, 880–887 (2008).

176. E. J. Botcherby, C. W. Smith, M. M. Kohl, D. Débarre, M. J. Booth, R. Juškaitis, O. Paulsen, T. Wilson, Aberration-free three-dimensional multiphoton imaging of neuronal activity at kHz rates. *Proc. Natl. Acad. Sci.* **109**, 2919–2924 (2012).

177. C. Dunsby, Optically sectioned imaging by oblique plane microscopy. *Opt. Express*. **16**, 20306–20316 (2008).

178. V. Liberini, R. Laudicella, M. Capozza, M. W. Huellner, I. A. Burger, S. Baldari, E. Terreno, D. Deandreis, The Future of Cancer Diagnosis, Treatment and Surveillance: A Systemic Review on Immunotherapy and Immuno-PET Radiotracers. *Molecules*. **26**, 2201 (2021).

179. A. H. Maurer, Combined imaging modalities: PET/CT and SPECT/CT. *Health Phys.* **95**, 571–576 (2008).

180. D. W. Townsend, Multimodality imaging of structure and function. *Phys. Med. Biol.* **53**, R1 (2008).

181. M. Bray, M. Di Mascio, F. de Kok-Mercado, D. J. Mollura, E. Jagoda, Radiolabeled antiviral drugs and antibodies as virus-specific imaging probes. *Antiviral Res.* **88**, 129–142 (2010).

182. K. Wechalekar, B. Sharma, G. Cook, PET/CT in oncology—a major advance. *Clin.*

Radiol. **60**, 1143–1155 (2005).

183. L. Gorospe, S. Raman, J. Echeveste, N. Avril, Y. Herrero, S. Herna, Whole-body PET/CT: spectrum of physiological variants, artifacts and interpretative pitfalls in cancer patients. *Nucl. Med. Commun.* **26**, 671–687 (2005).

184. D. N. Levin, C. A. Pelizzari, G. T. Chen, C.-T. Chen, M. D. Cooper, Retrospective geometric correlation of MR, CT, and PET images. *Radiology*. **169**, 817–823 (1988).

185. D. W. Townsend, J. P. J. Carney, J. T. Yap, N. C. Hall, PET/CT today and tomorrow. *J. Nucl. Med.* **45**, 4S-14S (2004).

186. A. W. Segal, M. Geisow, R. Garcia, A. Harper, R. Miller, The respiratory burst of phagocytic cells is associated with a rise in vacuolar pH. *Nature*. **290**, 406–409 (1981).

187. R. A. Saxton, D. M. Sabatini, mTOR Signaling in Growth, Metabolism, and Disease. *Cell*. **168**, 960–976 (2017).

188. R. Puertollano, mTOR and lysosome regulation. *F1000Prime Rep.* **6**, 52 (2014).

189. R. Zoncu, L. Bar-Peled, A. Efeyan, S. Wang, Y. Sancak, D. M. Sabatini, mTORC1 senses lysosomal amino acids through an inside-out mechanism that requires the vacuolar H(+)-ATPase. *Science (80-.).* **334**, 678–683 (2011).

190. M. Overholtzer, J. S. Brugge, The cell biology of cell-in-cell structures. *Nat. Rev. Mol. cell Biol.* **9**, 796–809 (2008).

191. M. Krajcovic, S. Krishna, L. Akkari, J. A. Joyce, M. Overholtzer, mTOR regulates phagosome and entotic vacuole fission. *Mol. Biol. Cell*. **24**, 3736–3745 (2013).

192. R. M. Dayam, A. Saric, R. E. Shilliday, R. J. Botelho, The Phosphoinositide-Gated Lysosomal Ca2+ Channel, TRPML1, Is Required for Phagosome Maturation. *Traffic*. **16**, 1010–1026 (2015).

193. M. A. Gray, C. H. Choy, R. M. Dayam, E. Ospina-Escobar, A. Somerville, X. Xiao, S. M. Ferguson, R. J. Botelho, Phagocytosis Enhances Lysosomal and Bactericidal Properties by Activating the Transcription Factor TFEB. *Curr Biol*. **26**, 1955–1964 (2016).

194. J. A. Martina, H. I. Diab, O. A. Brady, R. Puertollano, TFEB and TFE3 are novel components of the integrated stress response. *EMBO J.* **35**, 479–495 (2016).

195. S. Krishna, W. Palm, Y. Lee, W. Yang, U. Bandyopadhyay, H. Xu, O. Florey, C. B. Thompson, M. Overholtzer, PIKfyve Regulates Vacuole Maturation and Nutrient Recovery following Engulfment. *Dev Cell*. **38**, 536–547 (2016).

196. A. M. Scott, J. D. Wolchok, L. J. Old, Antibody therapy of cancer. *Nat. Rev. cancer*. **12**, 278–287 (2012).

197. Y. Shi, X. Fan, H. Deng, R. J. Brezski, M. Rycyzyn, R. E. Jordan, W. R. Strohl, Q. Zou, N. Zhang, Z. An, Trastuzumab triggers phagocytic killing of high HER2 cancer cells in vitro and in vivo by interaction with Fcγ receptors on macrophages. *J. Immunol.* **194**, 4379–4386 (2015).

198. M. P. Chao, A. A. Alizadeh, C. Tang, J. H. Myklebust, B. Varghese, S. Gill, M. Jan, A. C. Cha, C. K. Chan, B. T. Tan, C. Y. Park, F. Zhao, H. E. Kohrt, R. Malumbres, J. Briones, R. D. Gascoyne, I. S. Lossos, R. Levy, I. L. Weissman, R. Majeti, Anti-CD47 antibody synergizes with rituximab to promote phagocytosis

and eradicate non-Hodgkin lymphoma. *Cell*. **142**, 699–713 (2010).

199. K. D. Grugan, F. L. McCabe, M. Kinder, A. R. Greenplate, B. C. Harman, J. E. Ekert, N. van Rooijen, G. M. Anderson, J. A. Nemeth, W. R. Strohl, R. E. Jordan, R. J. Brezski, Tumor-associated macrophages promote invasion while retaining Fc-dependent anti-tumor function. *J. Immunol.* **189**, 5457–5466 (2012).

200. N. Gul, L. Babes, K. Siegmund, R. Korthouwer, M. Bogels, R. Braster, G. Vidarsson, T. L. ten Hagen, P. Kubes, M. van Egmond, Macrophages eliminate circulating tumor cells after monoclonal antibody therapy. *J. Clin. Invest.* **124**, 812–823 (2014).

201. M. B. Overdijk, S. Verploegen, M. Bogels, M. van Egmond, J. J. Lammerts van Bueren, T. Mutis, R. W. Groen, E. Breij, A. C. Martens, W. K. Bleeker, P. W. Parren, Antibody-mediated phagocytosis contributes to the anti-tumor activity of the therapeutic antibody daratumumab in lymphoma and multiple myeloma. *MAbs*. **7**, 311–321 (2015).

202. D. Tseng, J. P. Volkmer, S. B. Willingham, H. Contreras-Trujillo, J. W. Fathman, N. B. Fernhoff, J. Seita, M. A. Inlay, K. Weiskopf, M. Miyanishi, I. L. Weissman, Anti-CD47 antibody-mediated phagocytosis of cancer by macrophages primes an effective antitumor T-cell response. *Proc. Natl. Acad. Sci. USA*. **110**, 11103–11108 (2013).

203. A. R. Mantegazza, J. G. Magalhaes, S. Amigorena, M. S. Marks, Presentation of phagocytosed antigens by MHC class I and II. *Traffic*. **14**, 135–152 (2013).

204. K.-M. Lin, W. Hu, T. D. Troutman, M. Jennings, T. Brewer, X. Li, S. Nanda, P.

Cohen, J. A. Thomas, C. Pasare, IRAK-1 bypasses priming and directly links TLRs to rapid NLRP3 inflammasome activation. *Proc. Natl. Acad. Sci. USA*. **111**, 775–780 (2014).

205. J. Chao, E. S. Ward, R. J. Ober, A software framework for the analysis of complex microscopy image data. *IEEE Trans. Inf. Technol. Biomed.* **14**, 1075–1087 (2010).

206. T. Pham, P. Mero, J. W. Booth, Dynamics of macrophage trogocytosis of rituximab-coated B cells. *PLoS. One.* **6**, e14498 (2011).

207. B. Chazotte, Labeling lysosomes in live cells with LysoTracker. *Cold Spring Harb. Protoc.*, **2**, (2011), doi:10.1101/pdb.prot5571.

208. H. J. Lin, P. Herman, J. S. Kang, J. R. Lakowicz, Fluorescence lifetime characterization of novel low-pH probes. *Anal. Biochem.* **294**, 118–125 (2001).

209. C. R. Brooks, M. Y. Yeung, Y. S. Brooks, H. Chen, T. Ichimura, J. M. Henderson, J. V Bonventre, KIM-1-/TIM-1-mediated phagocytosis links ATG5-/ULK1-dependent clearance of apoptotic cells to antigen presentation. *EMBO J.* **34**, 2441–2464 (2015).

210. N. Panchuk-Voloshina, R. P. Haugland, J. Bishop-Stewart, M. K. Bhalgat, P. J. Millard, F. Mao, W.-Y. Leung, R. P. Haugland, Alexa dyes, a series of new fluorescent dyes that yield exceptionally bright, photostable conjugates. *J. Histochem. Cytochem.* **47**, 1179–1188 (1999).

211. M. T. Z. Spence, I. D. Johnson, The molecular probes handbook- A guide to fluorescent probes and labeling technologies (Molecular Probes, Life Technologies Corporation; Edition 11 (2010).

212. B. Kasmapour, A. Gronow, C. K. E. Bleck, W. Hong, M. G. Gutierrez, Size-dependent mechanism of cargo sorting during lysosome-phagosome fusion is controlled by Rab34. *Proc. Natl. Acad. Sci. USA*. **109**, 20485–20490 (2012).

213. E. P. Berthiaume, C. Medina, J. A. Swanson, Molecular size-fractionation during endocytosis in macrophages. *J. Cell Biol.* **129**, 989–998 (1995).

214. C. Settembre, C. Di Malta, V. A. Polito, M. G. Arencibia, F. Vetrini, S. Erdin, S. U. Erdin, T. Huynh, D. Medina, P. Colella, TFEB links autophagy to lysosomal biogenesis. *Science (80-.).* **332**, 1429–1433 (2011).

215. M. Sardiello, M. Palmieri, A. di Ronza, D. L. Medina, M. Valenza, V. A. Gennarino, C. Di Malta, F. Donaudy, V. Embrione, R. S. Polishchuk, A gene network regulating lysosomal biogenesis and function. *Science (80-.).* **325**, 473–477 (2009).

216. Y. Sancak, L. Bar-Peled, R. Zoncu, A. L. Markhard, S. Nada, D. M. Sabatini, Ragulator-Rag complex targets mTORC1 to the lysosomal surface and is necessary for its activation by amino acids. *Cell*. **141**, 290–303 (2010).

217. E. Muraille, P. Gounon, J. Cazareth, J. Hoebeke, C. Lippuner, A. Davalos-Misslitz, T. Aebischer, S. Muller, N. Glaichenhaus, E. Mougneau, Direct visualization of peptide/MHC complexes at the surface and in the intracellular compartments of cells infected in vivo by Leishmania major. *PLoS Pathog.* **6**, e1001154 (2010).

218. J. Han, K. Burgess, Fluorescent Indicators for Intracellular pH. *Chem. Rev.* **110**, 2709–2728 (2010).

219. M. Desjardins, N. N. Nzala, R. Corsini, C. Rondeau, Maturation of phagosomes is

accompanied by changes in their fusion properties and size-selective acquisition of solute materials from endosomes. *J. Cell Sci.* **110 (Pt 1**, 2303–2314 (1997).

220. N. A. Bright, L. J. Davis, J. P. Luzio, Endolysosomes Are the Principal Intracellular Sites of Acid Hydrolase Activity. *Curr. Biol.* **26**, 2233–2245 (2016).

221. C. Astarie-Dequeker, S. Carreno, C. Cougoule, I. Maridonneau-Parini, The protein tyrosine kinase Hck is located on lysosomal vesicles that are physically and functionally distinct from CD63-positive lysosomes in human macrophages. *J. Cell Sci.* **115**, 81–89 (2002).

222. R. M. Yates, A. Hermetter, G. A. Taylor, D. G. Russell, Macrophage activation downregulates the degradative capacity of the phagosome. *Traffic*. **8**, 241–250 (2007).

223. L. Cohn, B. Chatterjee, F. Esselborn, A. Smed-Sörensen, N. Nakamura, C. Chalouni, B.-C. Lee, R. Vandlen, T. Keler, P. Lauer, Antigen delivery to early endosomes eliminates the superiority of human blood BDCA3+ dendritic cells at cross presentation. *J. Exp. Med.* **210**, 1049–1063 (2013).

224. J. A. Martina, Y. Chen, M. Gucek, R. Puertollano, MTORC1 functions as a transcriptional regulator of autophagy by preventing nuclear transport of TFEB. *Autophagy*. **8**, 903–914 (2012).

225. A. Roczniak-Ferguson, C. S. Petit, F. Froehlich, S. Qian, J. Ky, B. Angarola, T. C. Walther, S. M. Ferguson, The transcription factor TFEB links mTORC1 signaling to transcriptional control of lysosome homeostasis. *Sci. Signal.* **5**, ra42 (2012).

226. M. Palmieri, R. Pal, H. R. Nelvagal, P. Lotfi, G. R. Stinnett, M. L. Seymour, A.

Chaudhury, L. Bajaj, V. V Bondar, L. Bremner, U. Saleem, D. Y. Tse, D. Sanagasetti, S. M. Wu, J. R. Neilson, F. A. Pereira, R. G. Pautler, G. G. Rodney, J. D. Cooper, M. Sardiello, mTORC1-independent TFEB activation via Akt inhibition promotes cellular clearance in neurodegenerative storage diseases. *Nat Commun*. **8**, 14338 (2017).

227. R. Milo, What is the total number of protein molecules per cell volume? A call to rethink some published values. *BioEssays*. **35**, 1050–1055 (2013).

228. M. Bohdanowicz, S. Grinstein, Role of phospholipids in endocytosis, phagocytosis, and macropinocytosis. *Physiol. Rev.* **93**, 69–106 (2013).

229. S. K. Dove, K. Dong, T. Kobayashi, F. K. Williams, R. H. Michell, Phosphatidylinositol 3, 5-bisphosphate and Fab1p/PIKfyve underPPIn endo-lysosome function. *Biochem. J.* **419**, 1–13 (2009).

230. W. F. D. Acqua, R. M. Woods, E. S. Ward, S. R. Palaszynski, N. K. Patel, Y. A. Brewah, H. Wu, P. A. Kiener, S. Langermann, Increasing the Affinity of a Human IgG1 for the Neonatal Fc Receptor: Biological Consequences. *J. Immunol.* **169**, 5171–5180 (2002).

231. R. J. Ludwig, K. Vanhoorelbeke, F. Leypoldt, Z. Kaya, K. Bieber, S. M. McLachlan, L. Komorowski, J. Luo, O. Cabral-Marques, C. M. Hammers, J. M. Lindstrom, P. Lamprecht, A. Fischer, G. Riemekasten, C. Tersteeg, P. Sondermann, B. Rapoport, K.-P. Wandinger, C. Probst, A. El Beidaq, E. Schmidt, A. Verkman, R. A. Manz, F. Nimmerjahn, Mechanisms of Autoantibody-Induced Pathology. *Front. Immunol.* **8** (2017), doi:10.3389/fimmu.2017.00603.

232. S. Sathasivam, Steroids and immunosuppressant drugs in myasthenia gravis. *Nat. Clin. Pract. Neurol.* **4**, 317–327 (2008).

233. C. Kneitz, M. Wilhelm, H. Tony, Effective B cell depletion with rituximab in the treatment of autoimmune diseases. *Immunobiology*. **206**, 519–527 (2002).

234. A. S. Rosenberg, A. R. Pariser, B. Diamond, L. Yao, L. A. Turka, E. Lacana, P. S. Kishnani, A role for plasma cell targeting agents in immune tolerance induction in autoimmune disease and antibody responses to therapeutic proteins. *Clin. Immunol.* **165**, 55–59 (2016).

235. W. M. Baldwin, A. Valujskikh, R. L. Fairchild, The neonatal Fc receptor: Key to homeostatic control of IgG and IgG-related biopharmaceuticals. *Am. J. Transplant.* **19**, p 1881-1887 (2019), doi:10.1111/ajt.15366.

236. L. E. Ling, S. Roy, T. Daly, E. Cochran, S. Tyler, L. Markowitz, D. Bulik, A. Choudhury, J. Meador, V. Parge, M281: A Therapeutic Anti-FcRn Blocking Antibody for Rapid Clearance of IgG and IgG Autoantibodies in Immune Cytopenias and Other Auto/Allo-Immune Disease (2015), doi:10.1182/blood.V126.23.3472.3472.

237. J. F. Howard, V. Bril, T. M. Burns, R. Mantegazza, M. Bilinska, A. Szczudlik, S. Beydoun, F. J. R. D. R. Garrido, F. Piehl, M. Rottoli, Randomized phase 2 study of FcRn antagonist efgartigimod in generalized myasthenia gravis. *Neurology*. **92**, e2661–e2673 (2019).

238. B. Smith, A. Kiessling, R. Lledo-Garcia, K. L. Dixon, L. Christodoulou, M. C. Catley, P. Atherfold, L. E. D'Hooghe, H. Finney, K. Greenslade, H. Hailu, L.

Kevorkian, D. Lightwood, C. Meier, R. Munro, O. Qureshi, K. Sarkar, S. P. Shaw, R. Tewari, A. Turner, K. Tyson, S. West, S. Shaw, F. R. Brennan, Generation and characterization of a high affinity anti-human FcRn antibody, rozanolixizumab, and the effects of different molecular formats on the reduction of plasma IgG concentration. *MAbs*, 1–20 (2018).

239. D. D. Patel, J. B. Bussel, Neonatal Fc receptor in human immunity: function and role in therapeutic intervention. *J. Allergy Clin. Immunol.* **146**, 467–478 (2020).

240. J. C. Kang, W. Sun, P. Khare, M. Karimi, X. Wang, Y. Shen, R. J. Ober, E. S. Ward, Engineering a HER2-specific antibody–drug conjugate to increase lysosomal delivery and therapeutic efficacy. *Nat. Biotechnol.* **37**, 523–526 (2019).

241. C. G. Radu, S. M. Anderton, M. Firan, D. C. Wraith, E. S. Ward, Detection of autoreactive T cells in H-2u mice using peptide–MHC multimers. *Int. Immunol.* **12**, 1553–1560 (2000).

242. O. Woodford, vol3d v2. *MATLAB Cent. File Exch.*, (available at https://www.mathworks.com/matlabcentral/fileexchange/22940-vol3d-v2).

243. D. S. C. Biggs, M. Andrews, Acceleration of iterative image restoration algorithms. *Appl. Opt.* **36**, 1766 (1997).

244. M. Born, E. Wolf, Principles of optics: electromagnetic theory of propagation, interference and diffraction of light (Elsevier, 2013).

245. M. Unser, A. Aldroubi, M. Eden, B-spline signal processing. I. Theory. *IEEE Trans. Signal Process.* **41**, 821–833 (1993).

246. Z. Gan, S. Ram, C. Vaccaro, R. J. Ober, E. S. Ward, Analyses of the Recycling

Receptor, FcRn, in Live Cells Reveal Novel Pathways for Lysosomal Delivery. *Traffic*. **10**, 600–614 (2009).

247. A. E. Toth, M. R. Holst, M. S. Nielsen, Vesicular transport machinery in brain endothelial cells: what we know and what we do not. *Curr. Pharm. Des.* **26**, 1405–1416 (2020).

248. B. J. Wilson, J. L. Allen, P. T. Caswell, Vesicle trafficking pathways that direct cell migration in 3D matrices and in vivo. *Traffic*. **19**, 899–909 (2018).

249. P. Watson, A. T. Jones, D. J. Stephens, Intracellular trafficking pathways and drug delivery: fluorescence imaging of living and fixed cells. *Adv. Drug Deliv. Rev.* **57**, 43–61 (2005).

250. J. Huotari, A. Helenius, Endosome maturation. *EMBO J.* **30**, 3481–3500 (2011).

251. J. Chao, T. Lee, E. S. Ward, R. J. Ober, Fluorescent Microspheres as Point Sources: A Localization Study. *PLoS One*. **10**, e0134112 (2015).

252. Z. Liu, W. R. Legant, B.-C. Chen, L. Li, J. B. Grimm, L. D. Lavis, E. Betzig, R. Tjian, 3D imaging of Sox2 enhancer clusters in embryonic stem cells. *Elife*. **3**, e04236 (2014).

253. F. Wäldchen, J. Schlegel, R. Götz, M. Luciano, M. Schnermann, S. Doose, M. Sauer, Whole-Cell imaging of plasma membrane receptors by 3D lattice light-sheet d STORM. *Nat. Commun.* **11**, 1–6 (2020).

254. L. Möckl, W. E. Moerner, Super-resolution microscopy with single molecules in biology and beyond–essentials, current trends, and future challenges. *J. Am. Chem. Soc.* **142**, 17828–17844 (2020).

255. L. Xie, P. Dong, X. Chen, T.-H. S. Hsieh, S. Banala, M. De Marzio, B. P. English, Y. Qi, S. K. Jung, K.-R. Kieffer-Kwon, 3D ATAC-PALM: super-resolution imaging of the accessible genome. *Nat. Methods*. **17**, 430–436 (2020).

256. K. Welsher, H. Yang, Multi-resolution 3D visualization of the early stages of cellular uptake of peptide-coated nanoparticles. *Nat. Nanotechnol.* **9**, 198 (2014).

257. R.-L. Zhang, F. W. Pratiwi, B.-C. Chen, P. Chen, S.-H. Wu, C.-Y. Mou, Simultaneous Single-Particle Tracking and Dynamic pH Sensing Reveal Lysosome-Targetable Mesoporous Silica Nanoparticle Pathways. *ACS Appl. Mater. Interfaces*. **12**, 42472–42484 (2020).

258. R. Goldstein, J. Sosabowski, K. Vigor, K. Chester, T. Meyer, Developments in single photon emission computed tomography and PET-based HER2 molecular imaging for breast cancer. *Expert Rev. Anticancer Ther.* **13**, 359–373 (2013).

259. J. S. Jaggi, J. A. Carrasquillo, S. V Seshan, P. Zanzonico, E. Henke, A. Nagel, J. Schwartz, B. Beattie, B. J. Kappel, D. Chattopadhyay, Improved tumor imaging and therapy via iv IgG–mediated time-sequential modulation of neonatal Fc receptor. *J. Clin. Invest.* **117**, 2422–2430 (2007).

260. A. M. Wu, Engineered antibodies for molecular imaging of cancer. *Methods*. **65**, 139–147 (2014).

261. W. Sun, P. Khare, X. Wang, D. K. Challa, B. M. Greenberg, R. J. Ober, E. S. Ward, Selective Depletion of Antigen-Specific Antibodies for the Treatment of Demyelinating Disease. *Mol. Ther.* (2020).

262. M. C. Franklin, K. D. Carey, F. F. Vajdos, D. J. Leahy, A. M. De Vos, M. X.

Sliwkowski, Insights into ErbB signaling from the structure of the ErbB2-pertuzumab complex. *Cancer Cell*. **5**, 317–328 (2004).

263. A. M. Loening, S. S. Gambhir, AMIDE: a free software tool for multimodality medical image analysis. *Mol. Imaging*. **2**, 15353500200303132 (2003).

264. J. A. Carrasquillo, N. Pandit-Taskar, J. A. O'Donoghue, J. L. Humm, P. Zanzonico, P. M. Smith-Jones, C. R. Divgi, D. A. Pryma, S. Ruan, N. E. Kemeny, 124I-huA33 antibody PET of colorectal cancer. *J. Nucl. Med.* **52**, 1173–1180 (2011).

265. S. M. Knowles, A. M. Wu, Advances in immuno–positron emission tomography: antibodies for molecular imaging in oncology. *J. Clin. Oncol.* **30**, 3884 (2012).

266. R. Rossin, P. Renart Verkerk, S. M. van den Bosch, R. C. M. Vulders, I. Verel, J. Lub, M. S. Robillard, In vivo chemistry for pretargeted tumor imaging in live mice. *Angew. Chemie*. **122**, 3447–3450 (2010).

267. E. M. F. Billaud, S. Belderbos, F. Cleeren, W. Maes, M. Van de Wouwer, M. Koole, A. Verbruggen, U. Himmelreich, N. Geukens, G. Bormans, Pretargeted PET imaging using a bioorthogonal 18F-labeled trans-cyclooctene in an ovarian carcinoma model. *Bioconjug. Chem.* **28**, 2915–2920 (2017).

268. T. Olafsen, D. Betting, V. E. Kenanova, F. B. Salazar, P. Clarke, J. Said, A. A. Raubitschek, J. M. Timmerman, A. M. Wu, Recombinant anti-CD20 antibody fragments for small-animal PET imaging of B-cell lymphomas. *J. Nucl. Med.* **50**, 1500–1508 (2009).

269. S. M. Knowles, K. A. Zettlitz, R. Tavaré, M. M. Rochefort, F. B. Salazar, D. B. Stout, P. J. Yazaki, R. E. Reiter, A. M. Wu, Quantitative immunoPET of prostate

cancer xenografts with 89Zr-and 124I-labeled anti-PSCA A11 minibody. *J. Nucl. Med.* **55**, 452–459 (2014).

270. M. Stangel, R. Pul, Basic principles of intravenous immunoglobulin (IVIg) treatment. *J. Neurol.* **253**, v18–v24 (2006).

271. R. Clynes, Protective mechanisms of IVIG. *Curr. Opin. Immunol.* **19**, 646–651 (2007).

272. O. Krenkel, F. Tacke, Liver macrophages in tissue homeostasis and disease. *Nat. Rev. Immunol.* **17**, 306–321 (2017).

273. M. Guilliams, C.-A. Dutertre, C. L. Scott, N. McGovern, D. Sichien, S. Chakarov, S. Van Gassen, J. Chen, M. Poidinger, S. De Prijck, Unsupervised high-dimensional analysis aligns dendritic cells across tissues and species. *Immunity*. **45**, 669–684 (2016).

274. D. K. Challa, X. Wang, H. P. Montoyo, R. Velmurugan, R. J. Ober, E. S. Ward, in *MAbs* (Taylor & Francis, 2019), vol. 11, pp. 848–860.

275. R. Velmurugan, Using Advanced Microscopy Techniques for the Study of Macrophage-Cancer Cell Interactions in the Presence of Therapeutic Antibodies (2017).